Manifestation of Colossal Thermoelectric Power by Charge Ordered Small and Intermediate Bandwidth Manganites

Thesis submitted to
Cochin University of Science and Technology
in partial fulfilment of the requirements for the
award of the degree of

Doctor of Philosophy

Lija K Joy

Department of Physics
Cochin University of Science and Technology
Cochin- 682022
India

August 2015

Manifestation of Colossal Thermoelectric Power by Charge Ordered Small and Intermediate Bandwidth Manganites

Ph.D Thesis

Author:

Lija K Joy
Thattaruthundil Star Light
Puthoor P.O.
Kollam- 691507
Kerala. India
E-Mail: lijakjoy@gmail.com

Supervising Guide:

Prof. (Dr.) M. R. Anantharaman
Professor, Department of Physics
Cochin University of Science and Technology
Cochin - 682 022
Kerala. India.

August 2015

Cover page illustration:

Front: Schematic of a thermoelectric module in power generation mode

Back: Colossal thermoelectric power exhibited by $La_{0.5}Ca_{0.5}MnO_3$

Department of Physics
Cochin University of Science and Technology
Cochin – 682022

Certificate

Certified that the present Ph.D. thesis work entitled **"Manifestation of Colossal Thermoelectric Power by Charge Ordered Small and Intermediate Bandwidth Manganites, "** submitted by **Mrs. Lija K Joy** is an authentic record of research work carried out by her under my supervision in the Department of Physics in partial fulfillment of the requirements for the Degree of Doctor of Philosophy of Cochin University of Science and Technology, and has not been included in any other thesis submitted previously for the award of any degree.

.

August 2015

Cochin -22

Prof. M. R. Anantharaman

Supervising Guide
Department of Physics
CUSAT

DECLARATION

I hereby declare that the Ph.D. thesis work entitled, **"Manifestation of Colossal Thermoelectric Power by Charge Ordered Small and Intermediate Bandwidth Manganites"** is based on the original work carried out by me under the guidance of **Prof. M R Anantharaman,** in the Department of Physics, Cochin University of Science and Technology, Cochin-22 and has not been included in any other thesis submitted previously for the award of any degree.

Lija K Joy

Cochin – 22
August 2015

Department of Physics
Cochin University of Science and Technology
Cochin – 682022

Certificate

Certified that all the relevant corrections and modifications suggested by the audience during the Pre-synopsis seminar and recommended by the Doctoral Committee of the candidate has been incorporated in the thesis.

Cochin -22
August 2015

Prof. M. R. Anantharaman

Supervising Guide
Department of Physics
CUSAT

Acknowledgement

It is with great pleasure that I present my doctoral thesis and I wish to express my heartfelt gratitude and thanks to all those who helped me in realizing my dream.

First and foremost, I am obliged to Prof. M R Anantharaman, my mentor and teacher who helped me to toddle in the world of research. I am grateful to him for his valuable support, encouragement and help throughout my research work. I express my deep sense of gratitude to his family for their support during the course of this work.

I wish to acknowledge former Head of the Department of Physics, Cochin University of Science and Technology, Prof. B. Pradeep and present head Prof. S. Jayalekshmi for providing the laboratory and library facilities during my research program. I am thankful to all the faculty members and non-teaching staff of the department of Physics, CUSAT, for the support they have provided me for the completion of this research work. I also wish to acknowledge my doctoral committee member Prof. P. Radhakrishnan, former Director of International School of Photonics, CUSAT for his valuable help.

During my Ph.D programme I was supported by University Junior Research Fellowship from CUSAT (2010-2012) and Research Fellowship in Sciences for meritorious students (RFSMS) by UGC (2012-2015) in the form of junior and senior research fellowships. I acknowledge the financial support extended to me during my research work.

I am thankful to Prof. Manfred Albrecht, Institute of physics, University of Augsburg, Germany for giving me a chance to carry out a part of my Ph.D work with him in the Institute of Physics, Technical University of Chemnitz, Germany. I sincerely acknowledge the help received from Dr. Andreas Leibig, Dr. Marcus Daniel, Ms Birgit Hebler, Mr. Patrick Matthes,

Mr. Jonny Franke, Mr. Phani Kanth Arekapudi in the Institute of Physics, TU Chemnitz, Germany. I express my gratitude to Mr. Varun, Technical University of Chemnitz, Germany for his help and company during my stay in Germany.

I also extend my sincere gratitude to the INUP programme of the Centre for Nanoelectronics, IIT-Bombay especially to the co-ordinators, Dr. K. Nageshwari, Prof. Anil Kottantharayil and Prof. Ramgopal Rao. Their support was crucial for my work especially in the thin film deposition and characterization.

I express my sincere gratitude to Dr. V Ganesan and Dr. R. Raawat, IUC Indore for allowing me to carry out thermoelectric power and resistivity measurements. I am grateful to P.M. Ajayan, Rice University, USA and Dr. Salim Al Harthi, SQU Oman for their help regarding XPS measurements.

I would like to thank the following persons who supported me during various stages of my research. I thankfully remember Mr.Shanmukharao Samatham, Durgesh Singh of IUC, Indore, Ms. Shailaja, and Ms. Gayathri of IIT Bombay. I was also fortunate to get good friends like Mr. Arun Thoms and Mrs. Yashna Sharma of IIT Delhi. This friendship made my stay in IIT Bombay more comfortable.

I wish to acknowledge all my lab mates in my second home, Magnetics Laboratory in the Department of Physics, CUSAT for the support I received from them. I would like to thank Dr. Hysen Thomas (Hysen chettan), Dr. Geetha P.(Geetha chechi), Mr. Vasudevan Namboodiri (Babu sir), Mrs. Vinayasree S., Dr. Sethulakshmi N., Dr. Sudeep P.M., Mrs. Lisha Raghavan, Mr.Sivaraj K.S., Ms. Archana V. N., Mr. Thoufeeq S., Mr. Sreeram P. R, Ms. Bintu Thomas, Ms. Pooja V. Janardanan, Ms. Reyha Benedict and Bharath Chandran. Special love and thanks to Mr. Aravind P.B. and Ms. Beena Mol.

Special thanks to Dr. Senoy Thomas, NIIST Trivandrum for providing magnetic measurements and useful discussions throughout the research period. I am sincerely thankful to Dr. T.N.Narayanan, Dr. Vijutha Sunny, Dr.Sagar S., Dr. Reena Mary and Dr. Smitha Sasidharan for their valuable advice.

I thank all of my friends at CUSAT. I extend my sincere thanks to Mr. Santhosh M.V., Mr. Abhilash A. Dr. Poornima N. (Poornima chechi) and Ms. Hasna for the nice moments at CUSAT. I am also grateful to Mrs Smrithy Vasudevan and Mrs Lini Devassy for their support and valuable help when I started my research. I express my gratitude to my roommate in the Athulya hostel Mrs, Jimily C. Jacob for her love and affection.

I use this occasion to thank and remember all of my school and college teachers, especially Anilkumar Sir, S.N.S.M. Higher Secondary School, Elampalloor for inculcating research interest in me and moulding me in this form.

My deepest gratitude to my family, they were with me at each stage of my research work. Words are insufficient to express my acknowledgements to my ever loving parents (my Pappa and my Mummy), for they have been the inspiring force behind me. They supported and encouraged me during all my difficult times. I am deeply indebted to my husband, Mr. Geevarughese John for his constant encouragement, love and support without which I would not have completed this research work. I am thankful to my grandmother, in laws, sister, and brother, my brother in law and sister in law and my other beloved relatives. My mother has been there with me at each stage of my life and I have no suitable word that can fully describe her everlasting love and care to me. I use this occasion to express my gratitude by dedicating this thesis to my beloved mummy.

Above all I thank God Almighty for all His blessings showered upon me. I bow my head humbly before Him for making me capable of completing this thesis.

Preface

Thermoelectric materials are revisited for various applications including power generation. The direct conversion of temperature differences into electric voltage and vice versa is known as thermoelectric effect. Possible applications of thermoelectric materials are in eco-friendly refrigeration, electric power generation from waste heat, infrared sensors, temperature controlled-seats and portable picnic coolers. Thermoelectric materials are also extensively researched upon as an alternative to compression based refrigeration. This utilizes the principle of Peltier cooling. The performance characteristic of a thermoelectric material, termed as figure of merit (ZT) is a function of several transport coefficients such as electrical conductivity (σ), thermal conductivity (κ) and Seebeck coefficient of the material (S). ZT is expressed as $ZT = \frac{S^2 \sigma T}{\kappa}$, where T is the temperature in degree absolute. A large value of Seebeck coefficient, high electrical conductivity and low thermal conductivity are necessary to realize a high performance thermoelectric material. The best known thermoelectric materials are phonon-glass electron – crystal (PGEC) system where the phonons are scattered within the unit cell by the rattling structure and electrons are scattered less as in crystals to obtain a high electrical conductivity.

A survey of literature reveals that correlated semiconductors and Kondo insulators containing rare earth or transition metal ions are found to be potential thermoelectric materials. The structural magnetic and charge transport properties in manganese oxides having the general formula of $RE_{1-x}AE_xMnO_3$ (RE = rare earth, AE= Ca, Sr, Ba) are solely determined by

the mixed valence ($3^+/4^+$) state of Mn ions. In strongly correlated electron systems, magnetism and charge transport properties are strongly correlated. Within the area of strongly correlated electron systems the study of manganese oxides, widely known as manganites exhibit unique magneto electric transport properties, is an active area of research.

Strongly correlated systems like perovskite manganites, characterized by their narrow localized band and hoping conduction, were found to be good candidates for thermoelectric applications. Manganites represent a highly correlated electron system and exhibit a variety of phenomena such as charge, orbital and magnetic ordering, colossal magneto resistance and Jahn-Teller effect. The strong inter-dependence between the magnetic order parameters and the transport coefficients in manganites has generated much research interest in the thermoelectric properties of manganites. Here, large thermal motion or rattling of rare earth atoms with localized magnetic moments is believed to be responsible for low thermal conductivity of these compounds. The 4f levels in these compounds, lying near the Fermi energy, create large density of states at the Fermi level and hence they are likely to exhibit a fairly large value of Seebeck coefficient.

The physical properties of manganites are dictated by the amount of substitution and the average ionic radii of both rare earth and substituting atoms. When rare earth ion is substituted with a divalent cation, the antiferromagnetic (AFM) phase of insulating parent compound $REMnO_3$ is progressively destroyed and transforms into a ferromagnet (FM) through an intermediate canted structure. This is due to the competing interaction between AFM and FM spin ordering of Mn^{3+} and Mn^{4+} ions. The electrical and magnetic properties of these mixed valent perovskite manganites strongly depend on the degree of substitution of trivalent element by divalent cations. The other factors that influence the nature of different magnetic

interactions in these compounds are small changes in Mn-O-Mn bond length and bond angles induced by tolerance factor.

With substitution, the antiferromagnetic (AFM) Mn^{3+}-O-Mn^{3+} interactions begin to compete with ferromagnetic (FM) Mn^{3+}-O-Mn^{4+} interactions resulting in the evolution of various magnetic phases of AFM-CAFM (canted AFM) -FM making them magnetically diverse. Out of various compositions in the phase diagram, the region where x=0.5 is the most important. Goodenough has reported that at x=0.5, Mn^{3+} and Mn^{4+} are equal in number and hence ordering of Mn^{3+} and Mn^{4+} species occurs over the lattice leading to charge ordering and co-existence of antiferromagnetism and ferromagnetism. Below this composition, FM phases are more favourable and above this composition AFM phases are favourable. As FM and AFM phases co-exist for charge ordered composition x=0.5, strong competition between these magnetic phases begins giving rise to a magnetically frustrated glass state or a spin glass state, which in turn prevents the occurrence of long range magnetic ordering. Hence the composition x = 0.5 is critical and the physical properties close to this composition assume significance.

In manganites, the width of conduction band formed by the hybridization of manganese e_g level and oxygen p level is termed as bandwidth. The size mismatch of the ions substituted into the perovskite lattice causes a change in the Mn-O-Mn bond angles and thereby, the conduction bandwidth (*W*). Based on this bandwidth, manganites are classified into three. They are large, intermediate and low bandwidth manganites. Tokura showed that the robustness of the charge/orbital ordering at x = 1/2 critically depends on bandwidth. In large bandwidth manganites, atomic orbitals are strongly over-lapping and valence electrons are more delocalized, whereas charge-ordering is a fully localized electron

phenomenon. Hence charge ordering (CO) is absent in large bandwidth manganites. However CO is possible in intermediate bandwidth manganites. For low bandwidth compounds, their magnetization, conductivity and magnetic ordering temperatures are lower when compared to manganites based on lighter rare earths. The replacement of lighter rare earth elements in mixed valent manganites by heavier rare earth elements induce lattice distortion associated with modification of tolerance factor which in turn influence the double exchange mechanism and hence influence magnetic interactions. Due to smaller ionic radii of heavier rare earth R atom, Mn-O-Mn bond distribution is maximum and hence a weak double exchange results. Thus a stable charge ordered phase exists over a wide range of doping (x=0.3 - 0.7) in small bandwidth manganites.

It has been pointed out that various effects such as localization due to charge ordering, short range magnetic ordering due to spin glass, electron – electron correlation, electron magnon scattering and electron phonon scattering strongly modify the temperature dependence of transport properties especially the thermoelectric power.

Colossal thermoelectric power has been observed in our recent investigations carried out on charge ordered compositions of small bandwidth manganites based on $Gd_{1-x}Sr_xMnO_3$ and the observed colossal thermoelectric power was explained based on charge and orbital ordered spin-glasses. The contribution to thermoelectric power from different scattering phenomena such as magnon drag, phonon drag, charge ordering and spin glass strongly depends on the grain size, the role of grain boundary and grain size on thermoelectric power is also of interest from a fundamental perspective which is found less investigated. Hence the grain size dependant transport properties in charge ordered $Gd_{1-x}Sr_xMnO_3$ (x =0.3, 0.5 and 0.6) samples are interesting and assume significance.

Also these manganites are found to be exhibiting magnetic reversal. Magnetic reversal is found to be an important phenomenon in magnetism and is utilized in magnetic data storage processes. To fabricate electronic and magnetic devices, thin film forms of these compositions are necessary. This study helps to compare the dimensional dependence on the physical properties of both bulk and thin film forms of these compositions. A systematic study of both the spin reversal and spin glass existence in the charge ordered region of both bulk and thin film form of $Gd_{1-x}Sr_xMnO_3$ assume significance and less investigated. So it is in this context that a thorough investigation on thin film forms of $Gd_{1-x}Sr_xMnO_3$ is relevant. This is a virgin area and rich Physics can be derived out of these investigations. This is one of the motivations of the present work.

Intermediate bandwidth manganites based on calcium, especially, the charge ordered composition, $La_{0.5}Ca_{0.5}MnO_3$, is interesting not only from a fundamental perspective but also from an applied angle as they are likely to exhibit colossal thermoelectric power as observed in $Gd_{0.5}Sr_{0.5}MnO_3$. Moreover, the mechanism leading to the display of colossal thermoelectric power is based on the charge and orbital ordered spin-glasses and it is presumed that these materials also could be another system to check the veracity of this mechanism proposed in the case of $Gd_{0.5}Sr_{0.5}MnO_3$. Phenomena like the co-existences of ferromagnetic and antiferromagnetic phases and of charge ordering (CO) in $La_{0.5}Ca_{0.5}MnO_3$ and $Gd_{1-x}Sr_xMnO_3$ (x =0.3, 0.5 and 0.6) is also interesting which warrants a thorough investigation. It will be our endeavour to apply suitable models for theoretical fitting of colossal thermoelectric power to propose a plausible mechanism for explaining the phenomenon of colossal thermoelectric power. This is yet another motivation of the present study

Charge Ordering is generally not found in large bandwidth manganites. Since the composition $La_{0.5}Sr_{0.5}MnO_3$, is a representative of large bandwidth manganites, was subjected to extensive investigations, especially, on the thermoelectric properties. This study is intended to provide a comparison vis a vis large, small and intermediate bandwidth manganites.

Colossal thermo power in charge ordered $La_{0.5}Ca_{0.5}MnO_3$, $Gd_{1-x}Sr_xMnO_3$ (x =0.3, 0.5 and 0.6) indicates that charge ordering is more pronounced in the case of intermediate and small band width manganites and they are likely to exhibit large Seebeck coefficient. The above mentioned charge ordered manganites exhibited colossal thermoelectric power only at very low temperatures. From an application point of view, it would be worthwhile to find a material or tailor these transition temperatures to near room temperature. So we extended our investigation to find a material exhibiting appreciable thermo power at room temperature. From literature it is found that doping with a heavy and small rare earth at calcium site in slightly electron doped perovskite $CaMnO_3$ families can exhibit a considerable Seebeck coefficient which also minimizes the phonon contribution the thermal conductivity (κ). Substitution of Ytterbium in $CaMnO_3$ will yield, $Ca_{0.9}Yb_{0.1}MnO_3$. This composition is envisaged to be a candidate material displaying appreciable thermoelectric power at near room temperature and above. Preliminary investigation will also be carried out on the thermoelectric power of this compound. Plausible mechanisms responsible for high thermoelectric power obtained at high temperature will be discussed. So the specific objectives of present investigation are:

- Synthesis of charge ordered small bandwidth manganites belonging to the series $Gd_{1-x}Sr_xMnO_3$ (x =0.3, 0.5 and 0.6) by wet solid state reaction method with varying sizes.

- Evaluation of size effect on the thermoelectric power in charge ordered small bandwidth manganites based on Gd-Sr.
- Deposition of thin films of $Gd_{1-x}Sr_xMnO_3$ using Pulsed Laser Deposition on silicon substrate.
- Study the phenomenon of the existence of spin reversal and spin glass in the charge ordered regions of both bulk and thin film form of $Gd_{1-x}Sr_xMnO_3$ through magnetic measurements.
- Synthesis of charge ordered intermediate bandwidth manganite, $La_{0.5}Ca_{0.5}MnO_3$, by mechanical milling.
- Evaluation of thermoelectric power of $La_{0.5}Ca_{0.5}MnO_3$.
- Study co-existence of spin glass and charge ordering through magnetic studies.
- Modelling of colossal thermoelectric power observed in the small and intermediate bandwidth manganites.
- Synthesis of $La_{0.5}Sr_{0.5}MnO_3$ by citrate gel method and evaluation of its thermoelectric power.
- Correlation of results.

This proposed thesis is entitled "**Manifestation of Colossal Thermoelectric Power by Charge Ordered Small and Intermediate Bandwidth Manganites**" and consists of seven chapters.

Chapter 1 provides an introduction to thermoelectricity and manganites. The properties of manganites are discussed in brief. Finally the motivation and the objectives of the work are brought out.

Chapter 2 discusses the various experimental techniques employed for characterization of these materials at various stages. The principle behind the analytical tools employed for characterization is also briefly discussed in this chapter.

Chapter 3 deals with the synthesis and transport properties including thermoelectric power, resistivity and magnetic studies of charge ordered intermediate bandwidth manganite, $La_{0.5}Ca_{0.5}MnO_3$. This chapter discusses the nature and origin of co-existence of charge ordering and spin-glass. The theoretical fitting of experimental thermoelectric power data is carried out by incorporating Kondo properties of the spin-glass along with magnon scattering proposed by Mandal are also described in this chapter.

The role of grain boundary and the grain size effect on different scattering mechanisms responsible for colossal thermoelectric power in charge ordered small bandwidth manganites $Gd_{1-x}Sr_xMnO_3$ (x=0.3, 0.5, 0.6) is discussed in **Chapter 4**.

Chapter 5 pertains to the synthesis and properties of half doped large bandwidth manganite $La_{0.5}Sr_{0.5}MnO_3$. Magnetoresistance, magnetic and thermoelectric power properties are discussed in this chapter.

Chapter 6 describes the thin film deposition of $Gd_{1-x}Sr_xMnO_3$ using Pulsed Laser Deposition on silicon substrate. A systematic study of both the spin reversal and spin glass existence in the charge ordered region of both bulk and thin film form of $Gd_{1-x}Sr_xMnO_3$ is briefly discussed in this chapter.

The inferences drawn out of this investigation is provided in **Chapter 7**. The scope for further studies is also highlighted in this chapter. Preliminary experiments carried out on $Ca_{0.9}Yb_{0.1}MnO_3$ indicate that they exhibit appreciable Seebeck coefficient at room temperature and the initial results are presented here.

Publications

Peer Reviewed Journals

1. A study on the magnetic properties of Gd-Sr based low bandwidth manganites in their bulk and thin film forms and evidence for magnetization reversal in bulk $Gd_{0.7}Sr_{0.3}MnO_3$; Lija K Joy, Senoy Thomas and M R Anantharaman, **Journal of Magnetism and Magnetic Materials** 398, 174–182 (2016).
2. Size effect on the colossal thermoelectric power in charge ordered small band width manganites based on Gd-Sr; **Lija K Joy**, Durgesh Singh, P M Sudeep, V Ganesan, P M Ajayan, Senoy Thomas and M R Anantharaman, **Material Research Express**, 2, 055504 (2015).
3. Colossal thermoelectric power in charge ordered lanthanum calcium manganites (La0.5Ca0.5MnO3); **Lija K. Joy**, S. Shanmukharao Samatham, Senoy Thomas, V. Ganesan, Salim Al-Harthi, A. Liebig, M. Albrecht and M. R. Anantharaman, **Journal of Applied Physics**, 116, 213701 (2014).
4. Large enhanced dielectric permittivity in polyaniline passivated core-shell nano magnetic iron oxide by plasma polymerization; **Lija K. Joy**, V. Sooraj, U. S. Sajeev, Swapna S. Nair, T. N. Narayanan, N. Sethulakshmi, P. M. Ajayan, and M. R. Anantharaman, **Applied Physics Letters,** 104, 121603 (2014).
5. Contact potential induced enhancement of magnetization in polyaniline coated nanomagnetic iron oxides by plasma polymerization; N. Sethulakshmi, V. Sooraj, U. S. Sajeev, Swapna S. Nair, T. N. Narayanan, **Lija K. Joy**, P. A. Joy, P. M. Ajayan, and M. R. Anantharaman, **Applied Physics Letters**, 103, 162414 (2013).

6. Large thermoelectric power in $Ca_{0.9}Yb_{0.1}MnO_3$ at higher temperature; **Lija K. Joy**, Senoy Thomas and M. R. Anantharaman (Manuscript under preparation).
7. Size dependent optical properties of Ag-SiO_2 nanocomposites with the presence of silver in different states in silica matrix; Beena Mol, **Lija K Joy**, Hysen Thomas, Vinoy Thomas, Cyriac Joseph, T. N. Narayanan, I.A. Al-Omari, N V Unnikrishnan and M R Anantharaman (Manuscript under preparation).

Conference Publications

1. Colossal thermoelectric power in charge ordered lanthanum calcium manganites; **Lija K. Joy**, Senoy Thomas and M. R. Anantharaman , International Conference on Science, Technology & Applications of Rare earths, ICSTAR 2015, April 23-25, Trivandrum, India.
2. Thermo power and magneto electric transport of nanostructured charge ordered $La_{0.5}Sr_{0.5}MnO_3$; **Lija K Joy**, Senoy Thomas, S. Shanmukharao Samatham, V. Ganesan, Rajeev Rawat, and M. R. Anantharaman, International conference on Magnetic Materials and applications, ICMagMA 2014, September 15-17, Pondichery, India.
3. Large thermoelectric power in $Ca_{0.9}Yb_{0.1}MnO_3$ at higher temperature; **Lija K Joy** and M.R. Anantharaman, ISAS National conference on Advanced Technologies for Material Processing and Diagnostics, September 18-20, 2014, Cochin, India.
4. Highly efficient thermo electric materials for energy harvesting applications; **Lija K Joy** and M R Anantharaman, National Seminar on Frontiers of Nanotechnology, March 6-7, 2014, Sree SankaraVidya Peetom College, Perumbavoor (***Oral Presentation***).

5. Magneto electric transport and thermo power properties of charge ordered lanthanum sodium manganites; **Lija K Joy**, Senoy Thomas, S Shanmukharao Samatham, V. Ganesan, Sudeep P M, and M R Anantharaman, International Conference on Magnetic Materials and Applications (MagMA -2013) , 5-7 December, IIT Guwahati, India.
6. Evidence for Existence of spin glass state in single phase polycrystalline $Gd_{0.99}Sr_{0.01}MnO_3$ through Structural and Magnetic Properties; **Lija K Joy** , Senoy Thomas, Manfred Albrecht and M R Anantharaman , National Conference On Emerging Technologies for processing and Utilization of Beach Sand Minerals, March 1-2, 2013,IMA, Cochin, India.
7. Effect of thermal annealing on the optical properties of Silver- Silica nanocomposites; Beena Mol, **Lija K Joy**, Hysen Thomas, Cyriac Joseph, Vinoy Thomas, N V Unnikrishnan and M. R Anantharaman, India Israel Meeting on Material science and Nanoscience – (IIMNN 2013), Jan 31-Feb 1, 2013, Kottayam, India.

Contents

Chapter 1

Thermoelectric power and manganites: An Overview

This chapter provides a comprehensive review on thermoelectric power. A brief account of the recent developments with regard to the development of high efficient thermoelectric materials is provided, simultaneously discussing some of the fundamental issues related to controlling their thermal and electrical conductivities. Potential applications of these thermoelectric materials in power generation and refrigeration modes are also discussed. An overview on manganites and various phenomena exhibited by manganites are discussed. Finally the motivation for the present study together with specific objectives is also detailed.

Thermoelectric power….

With increased awareness and civil society activism along with stricter legislations, the search for eco-friendly alternatives to conventional energy resources is a top priority for nations and in the spot light. This is more so in the area of utilization of waste heat as energy harvesters for various applications ranging from active cooling in hot spots to power generation by converting waste heat into useful electricity. Utilization of waste heat employs the principle of thermoelectricity wherein a temperature gradient in two dissimilar metals creates a potential difference. This is called Seebeck effect. The reverse phenomenon which is the production of cooling on applying a voltage gradient is called Peltier effect. Though both these phenomena were known for centuries, they have not been exploited for obvious reasons. Thus the field of thermoelectricity and thermoelectric materials is an active area of research for quite some time. With rapid strides made in materials technology and solid state physics, new and novel materials are investigated for plausible thermoelectric applications. There are many parameters that determine the performance characteristics of a good thermoelectric material. They are thermoelectric power, carrier density, electrical conductivity and thermal conductivity of the material. However, achieving high performance is essentially a trade-off between various parameters. From first principles, it is known that metals and insulators are not good thermoelectric materials, while heavily doped semiconductors are suitable for thermoelectric applications. Besides semiconductors, there are many materials available such as solid solution of Bi_2Te_3, Sb_2Te_3, PbTe and GeTe, skutterudites such as $CoSb_3$ or clathrates such as $Sr_8Ga_{16}Ge_{30}$ and quantum dot super lattices which exhibit good thermoelectric performance [1].

Highly correlated systems, wherein, the principle of correlation is utilized to make high performance thermoelectric materials is quite

promising. Manganites are ideal correlated systems. They exhibit a rich variety of properties and there exist a close correlation between structure, electron transport and magnetic properties. Manganites exhibiting perovskite like structure have been a well-studied system and there is no dearth of literature on these class of materials. These materials are revisited because their properties can be tuned to meet the requirements of a good thermoelectric material. From a fundamental perspective, manganites, serve as a rich template for testing many hypothesis, models and mechanisms. This thesis looks at the various possibilities of converting manganites into a useful thermoelectric material by appropriate synthesis strategies and by studying the properties at various temperature regimes for tailoring its thermoelectric properties.

1.1 Thermoelectric Power (TEP)

The thermoelectric effect refers to the phenomenon of direct conversion of temperature differences to electric voltage and vice versa. The principle of thermoelectric conversion was first discovered by Thomas Seebeck in 1821 [2]. He found that when a temperature gradient ΔT is applied to the two ends of a metal bar, a voltage is generated. This phenomenon arises because the electrons at the hot end of the conductor diffuse towards the cold end of the conductor where the energy states are lower. Later in 1834 Jean Charles Athanase reversed the flow of electrons in Seebeck circuit to create refrigeration [3]. This effect is known as the Peltier effect. This idea forms the basis for the thermoelectric refrigerator. Scottish scientist William Thomson (later Lord Kelvin) discovered in 1854 that if a temperature difference exists between any two points of a current- carrying conductor, heat is either evolved or absorbed depending upon the material. The rate of change of thermoelectric voltage with respect to temperature is

called thermoelectric power or Seebeck coefficient (S). It is usually expressed in μV/K.

$$S = -\frac{dV}{dT} \tag{1.1}$$

The figure of merit (ZT) of a thermoelectric material is a function of transport coefficients such as electrical conductivity (σ), thermal conductivity (κ) and is defined as

$$ZT = \frac{S^2 \sigma T}{\kappa} \tag{1.2}$$

Here, S is the Seebeck coefficient of the material and T is absolute temperature. For practical applications, ZT should be greater than one [4]. A large value of Seebeck coefficient for obtaining high voltage, high electrical conductivity for reducing the internal resistance of the material and low thermal conductivity for creating a large temperature gradient between the ends of the material are necessary to realize a high performance thermoelectric material.

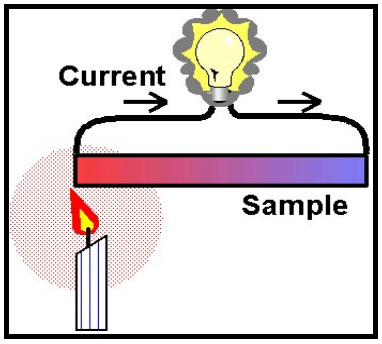

Figure 1.1: Simplest thermoelectric power circuit.

1.1.1 Conflicting thermoelectric properties

As these transport coefficients depend on inter related material properties, to maximize ZT a number of conflicting parameters need to be optimized. It is important to note that a material's Seebeck coefficient is

directly related to carrier density. The Seebeck coefficient of metals or semiconductors [5] is given by

$$S = \frac{8\Pi^2 k^2}{3eh^2} m^* T \left(\frac{\Pi}{3n}\right)^{2/3} \qquad (1.3)$$

Where n is the carrier concentration and m^* is the effective mass of carrier. From equation (1.3) it is seen that lower carrier concentration results in larger Seebeck coefficient. However, lower carrier concentration also results in lower electrical conductivity since

$$\sigma = \frac{1}{\rho} = ne\mu \qquad (1.4)$$

Where μ is the mobility of the carrier. Thus S and σ has reverse dependence on number of charge carriers. Maximum figure of merit typically occurs at carrier concentrations between 10^{19} and 10^{21} carriers per cm^3 (depending on the material system), which falls in between common metals and concentrations found in heavily doped semiconductors.

The effective mass of charge carriers is another conflicting property due to its reverse dependence on Seebeck coefficient and electrical conductivity. The inertial mass is associated to effective mass m^*. Hence heavy carriers will move with lower velocity which in turn leads to lower thermal conductivity. The numerical value of the optimum effective mass is not found to be mentioned in literature. Good thermoelectric materials can be found within a wide range of mobility and effective masses from both low-mobility high - effective mass polaron conductors (oxides) to high mobility low effective mass semiconductors (SiGe, GaAs) [6-7].

Another conflicting term in thermoelectric is thermal conductivity. Thermal conductivity in thermoelectric has two sources. One source is thermal conductivity due to heat transportation through electrons and holes and the other one is due to phonons travelling through the lattice [8]. Thus

thermal conductivity (κ) can be expressed as the sum of carrier component (κ_{car}) and phonon component (κ_{ph}),

$$\text{i.e} \quad \kappa = \kappa_{car} + \kappa_{ph} \tag{1.5}$$

From Wiedemann–Franz's law electronic term κ_{car} is directly related to the electrical conductivity as

$$\kappa_{car} = L_0 \sigma T = L_0 ne\mu T \tag{1.6}$$

where L_0 is the Lorentz constant, 2.4×10^{-8} $J^2 K^{-2} C^{-2}$ for free electrons.
High ZT requires high electrical conductivity but low thermal conductivity. However, these requirements are conflicting from first principles. For materials with very high electrical conductivity (metals) or very low κ_{ph}, the Seebeck coefficient alone primarily determines ZT, as can be seen in equation (1.7), where $(\kappa_{ph} / \kappa_{car}) << 1$:

$$ZT = \frac{S^2 / L_0}{1 + \frac{\kappa_{ph}}{\kappa_{car}}} \tag{1.7}$$

The value of κ_{car} is directly proportional to σ, and thus there is no way to reduce it while preserving the high electrical conductivity; however, κ_{ph} may be minimized. The reduction of κ_{ph} by tailoring material properties to minimize the propagation of phonons has proven to be the most successful strategy for the production of more efficient thermoelectric materials. The best thermoelectric materials were summarized as phonon-glass electron – crystal (PGEC) which means that the materials should have a low lattice thermal conductivity as in a glass and high electrical conductivity as in crystals. That is, the phonons are scattered more within the unit cell as in amorphous and electrons are scattered less as in crystals to obtain high electrical conductivity [9-11].

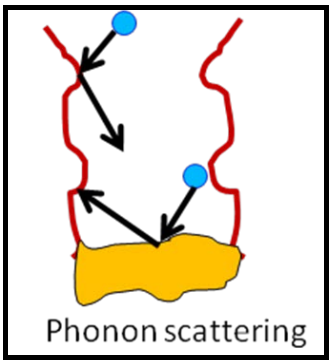

Figure 1.2: Phonon scattering

The best thermoelectric materials will have a small electronic contribution to the thermal conductivity, κ_{car}, thus maximizing the electronic conductivity while minimizing the thermal conductivity. As metals have small Seebeck coefficient and large electronic contribution to thermal conductivity, they are poor thermoelectric materials [12]. Insulators have a high Seebeck coefficient and a small electronic contribution to thermal conductivity; however their charge density and hence electrical conductivity are low leading to a low ZT. The best thermoelectric materials are between metals and insulators; ie semiconductors with an electron density of $10^{19}/cm^3$ [13].

Recently there has been a revival of interest in thermoelectric materials. A few of possible applications of thermoelectric power are in eco-friendly refrigeration, electric power generation from waste heat, infrared sensors, and in computer chips [4-13]. Thermoelectric materials are also extensively studied as an alternative to compression based refrigeration based on the principle of Peltier cooling [4]. The low efficiency of thermoelectric devices limits its applications. Scientists and engineers are scouting for novel materials for thermoelectric power generation applications. The main applications of thermoelectric effect including power generation from waste heat and eco friendly refrigeration are explained in

detail below. In power generation mode, electrons at the hot end of the conductor move towards the cold end of the conductor and thus transform heat into electricity. A thermoelectric device in power generation mode is shown in figure (1.3.a).

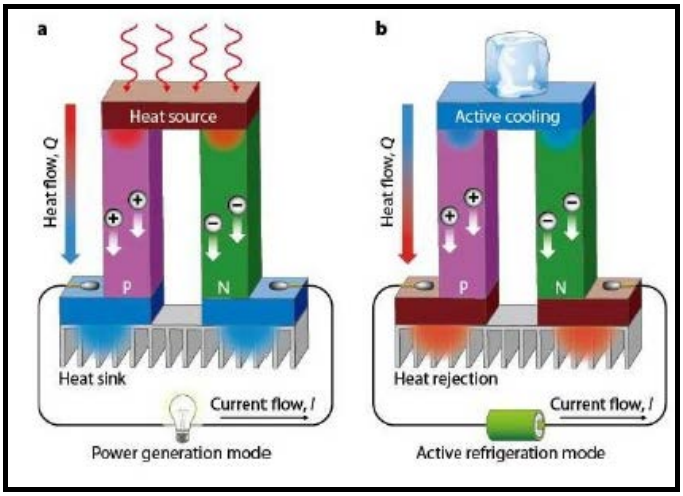

Figure 1.3: Thermoelectric module in (a) Power generation mode (b) Active refrigeration mode. Adopted from reference [14].

When a temperature gradient ΔT is applied to a thermoelectric couple consisting of n-type (electron transporting) and p- type (hole transporting) semiconductors, the mobile charge carriers at the hot end tend to diffuse to cold end. The build up of charge carriers at the cold end produces an electrostatic potential ΔV. An equilibrium is thus reached between the chemical potential for diffusion and the electrostatic repulsion due to the build-up of charge. This is the basis of thermoelectric power generation. A typical thermoelectric device is depicted in figure (1.4.a) which contain many thermoelectric couple (figure (1.4.b)) consisting of n-type and p-type thermoelectric elements which are connected electrically in series and thermally in parallel. A typical thermoelectric generator is shown in figure (1.5). It uses the heat flow across a temperature gradient to provide power to an electric load through the external circuit.

Thermoelectric power….

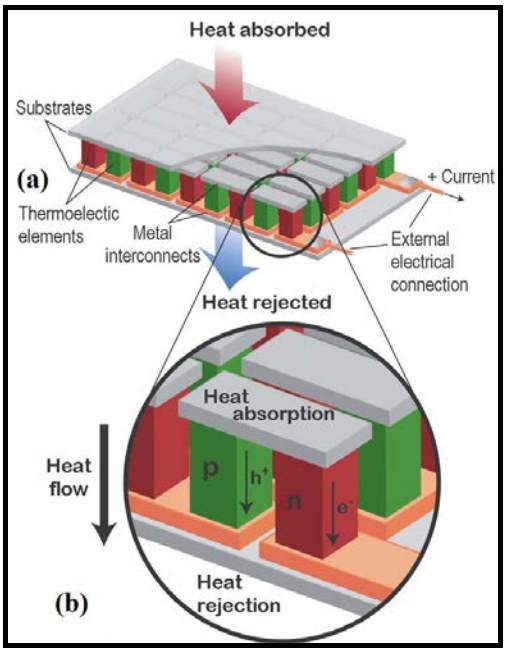

Figure 1.4: Thermoelectric module showing the direction of charge flow on both cooling and power generation. Adopted from reference [4].

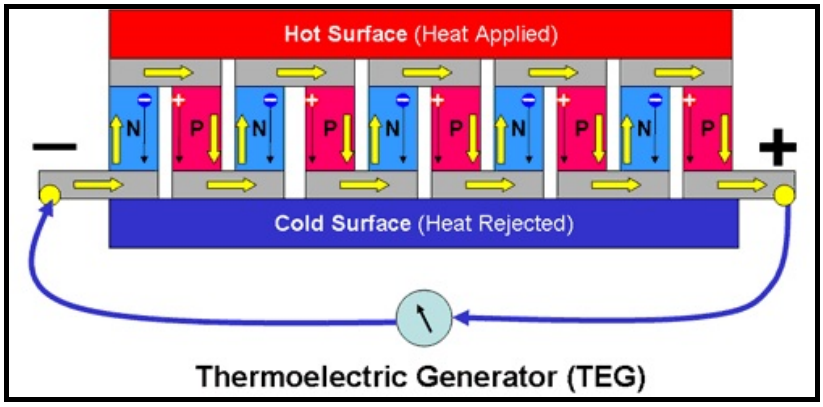

Figure 1.5: A typical thermoelectric generator. Adopted from reference [16].

Thermoelectric devices can be used as a refrigerator on the basis of Peltier effect. A thermoelectric device in an active refrigeration mode is shown in figure (1.3.b). When a voltage gradient ΔV is applied to a thermoelectric couple, the carriers try to return to the electronic equilibrium

that already existed before the current was applied by absorbing energy at one connector and releasing at the other. Thermoelectric technology has found profound applications in the field of waste heat recovery and solar heat utilization, temperature controlled-seats, portable picnic coolers and in satellites [14-15].

1.1.2 History

The field of thermoelectric has been heightened over the past decade due to the need for more efficient materials for electronic refrigeration and power generation. History of thermoelectric materials can be characterised by the progress of increasing value of ZT. Semiconductors for thermocouple applications started in late 1950s. Bi_2Te_3, a narrow gap semiconductor has been used as refrigeratior since 1950's [17]. Thermoelectric semiconductor devices for power generation were developed [12]. Solid solution of Bi_2Te_3 and isomorphous compounds such as Sb_2Te_3, PbTe and GeTe were discovered in the middle 1950's and this lead to the development of high performance thermoelectric material (ZT~1). During 1960's it is found that Phonon Glass Electron Crystal (PGEC) is a prerequisite for maximizing thermoelectric figure of merit [11].

In the mid 1990's, the bench mark of ZT=1 was broken by exploring new materials with complex crystal structures. In those compounds, rattling motion of loosely bonded atoms within the unit cell scatters phonons more by creating rattling structures without creating impact on the transport of electrons. Skutterudites and clathrates are typical phonon glass electron crystal materials [11, 18-20]. Skutterudites such as $CoSb_3$ or clathrates such as $Sr_8Ga_{16}Ge_{30}$ have cage-like structure [21-23]. When atoms are placed into the interstitial voids or cages of these materials, the lattice thermal conductivity can be significantly reduced compared with that of unfilled skutterudites [19].

ZT was further improved by reducing the dimensions of the materials. Dresselhaus *et al.* suggested that the use of quantum confinement in charge carriers improve power factor [24]. Another class of materials such as strongly correlated systems including cobaltites are also gaining increasing research interest for their thermoelectric properties [25-27]. The common features of these materials will be discuss detail in section 1.2. Venkatasubramanian *et al*. reported that p-type Bi_2Te_3/Sb_2Te_3 superlattices have the highest *ZT* of about 2.4 at 300K [28]. Later quantum dot superlattices such as PbTe/PbTeSe were reported to be of high ZT of about 3 at 600K [29]. Other useful approaches for enhancing TE properties are band structure engineering by doping [30-31] and also in Ag–Pb–Sb–Te or 'LAST', half-Heusler alloys and some high-ZT oxides [32]. Silicon nano wires are also reported to be highly interesting due to their low thermal conductivity [33-34]. All this investigation shed light on the development of various low dimensional systems like superlattices, nanowires and quantum dots as thermoelectric materials.

1.2 Strongly Correlated systems

Materials, basically, oxides comprised of transition metal elements belong to the class of correlated materials. In strongly correlated systems, each electron move with other electron in a correlated way owing to strong electron - electron Coulomb repulsion. In transition metal oxides, the d electrons are localized which means that the 'd' orbital functions are confined more closely to the nucleus than that for 's' or 'p' orbital having comparable energy. Spatial confinement of electrons in partially filled d or f orbitals of transition metal provides a strong coulomb repulsion between them.

The interplay between spin, charge and orbital moment has a profound influence on the properties of these materials. They are also prone

to small changes in temperature, pressure and ionic concentration [35-36]. These systems consists of simple transition metals exhibit remarkable properties like ferromagnetic/ antiferrromagnetic ordering, metal - insulator transition in oxides of transition metals, superconductivity in cuprates like $La_{2-x}Sr_xCuO_4$ and volume change associated with phase transitions in actinides are the effects of correlated electron behaviour [36-37]. Strongly correlated materials such as Cobaltites exhibit large thermoelectric power (Seebeck coefficient) and low thermal conductivity. Large thermoelectric power is due to the spin and orbital degeneracy of their strongly correlated electron bands and low thermal conductivity is due to their layered structure consisting of triangle-lattice CoO_2 layers or CoO_3 octahedral. Depending on the properties exhibited by correlated systems, they can be categorized as high T_C materials, mott insulators, spintronic materials, MR materials and perovskite manganites. It is thus believed that these correlated systems have brought a tremendous exploitation with theories like Density function theory (DFT) and Dynamic mean field theory (DMFT) to explain the physics of correlated systems.

Within the area of strongly correlated electrons, the study of manganese oxides (manganites) exhibiting unique magneto electric transport properties is an active area of research. The correlated structural magnetic and charge transport in manganese oxides of general formula $RE_{1-x}AE_xMnO_3$ (RE = rare earth, AE= Ca, Sr, Ba, Pb) is induced by the mixed valence ($3^+ - 4^+$) of the Mn ions [38]. Since there are strong correlations between magnetism and charge transport properties in strongly correlated electron systems such as in 3d transition metal oxides, conduction mechanism in these systems is a close correlation between magnetic, charge and spin degrees of freedom. Recently spin-charge coupled phenomena

found in strongly correlated system has ignited interest in scientists and engineers [39].

1.3 Manganites

Manganites represented by the general formula $RE_{1-x}AE_xMnO_3$, where RE is rare earth element and AE is the alkaline earth elements such as Ca, Sr and Ba is a prominent member of the ABO_3 type perovskite family. They came to the focus of research because of two significant features, namely, metal - insulator transition and exchange interaction mediated magnetism [37]. This series of compounds exhibits ferromagnetism and antiferromagnetism which depend upon the relative trivalent and tetravalent manganese ion content [40]. Generally the samples are purely ferromagnetic over a relatively narrow range of composition x ~ 0.3. Manganites became technologically important after the discovery of Colossal Magneto Resistance (CMR) in 1990's by Jin *et. al* [41]. The existence of competing interactions that arise from orbital, charge and spin degrees of freedom makes manganites an interesting system. The physical properties of manganites arise from two generic broad classes of competing effects. One is charge and orbital order (CO/OO) that lead to insulating and antiferromagnetically (AFM) ordered ground state and the second one is double-exchange interactions that lead to metallic ferromagnetically (FM) ordered ground state. These interactions can be tuned by a number of parameters such as the carrier concentration, structure and ionic size [42]. Manganites have found potential use in the field of magnetoelectrics, magnetic storage, switching devices, magnetocaloric effects and spintronics [43-49].

1.4 Historical Background of Manganites

From a historic point of view, manganites were studied in the fifties, both experimentally [40, 50-52] and theoretically [53-56]. The earliest work

on these manganites was carried out by Jonker and Van Santen' in 1950's [50-52]. They investigated the magnetic properties of a number of perovskite-type compounds and found that end members of the series, $RE_{1-x}AE_xMnO_3$, corresponding to $x = 0$ and $x = 1$, were antiferromagnetic insulators (AFI) and intermediate values of '*x*' were ferromagnetic (FM), particularly around $x = 0.30$. A sharp increase in electrical conductivity was observed with the onset of ferromagnetism. In the following year, Zener proposed the double exchange (DE) model [55] to explain the concomitant occurrence of ferromagnetism and metallicity in these materials observed by Jonker and Van Santen. This was followed by contributions from Anderson and Hasegawa in 1955 and de Gennes in 1960 [53,56].

The observed correlation between electrical and magnetic transitions in manganites has been explained within the frame work of the double exchange mechanism which describes the electronic hopping between two partially filled d orbitals of neighbouring Mn^{3+} and Mn^{4+} via central oxygen 2p orbital. The occurrence of magnetoresistance was first reported by Volger in 1954 [57]. He reported that maximum T_C and minimum resistivity observed when x=0.3 was a clear indication of correlation between magnetism and electrical conductivity. In 1955, Wollan and Koehler performed neutron diffraction studies on $La_{1-x}Ca_xMnO_3$ samples and prepared a phase diagram based on magnetic structure [40]. Neutron diffraction data revealed the presence of ferromagnetic (FM) and antiferromagnetic (AFM) regions and occasionally the simultaneous occurrence FM and AFM regions in $La_{1-x}Ca_xMnO_3$ [40]. This was the earliest report of phase coexistence in doped rare earth manganites. They established that a very rich magnetic phase diagram for different doping levels, where antiferromagnetism can take different configurations (A, C, CE and G types) and can even coexist with ferromagnetism (B type).

Tanaka *et. al* proposed an interpretation based on the charge localization into a small lattice polaron that conducts by hopping in the paramagnetic region [58]. Thus recent studies in mixed valent manganites have showed that double exchange is not a perfect tool to explain the overall scenario of transport and conduction mechanisms [56, 59-60]. Furthermore polaron effect due to very strong interaction between electron and phonon arising from the Jahn-Teller lattice distortion of Mn^{3+} is very crucial.

Manganites had become obsolete until the discovery of Colossal Magneto Resistance (CMR) in 1990's by Jin et al [41]. In 1993, MR~60% was observed in $La_{2/3}Ba_{1/3}MnO_3$ thin films [61]. In the following year Jin et al discovered MR in excess of 90% in $La_{0.67}Ca_{0.33}MnO_3$ thin films and reported that this magnitude was much larger than that reported as Giant Magneto Resistance (GMR) in multi layers. The term CMR for manganites was coined to discriminate the gigantic negative magnetoresistance MR observed in them, from the GMR observed in transition metal systems in multilayer or granular forms [37, 62-66].

The concept of mixed valence states and their control over the properties of manganites especially on the metallic conduction and the magnetic ordering was put forth by Verwey and de Boer [63]. Physical properties of manganites such as paramagnetic-ferromagnetic (PM-FM) transition at Curie temperature (T_C), insulator-metal transition (IMT) at temperature T_{im}, colossal magnetoresistance (CMR), antiferromagnetism (AFM) at Neel temperature T_N, charge ordering/orbital ordering (CO/OO) at T_{CO} depends upon the amount of substitution and average radius of A site cations [67].

1.5 Basic phenomena in manganites

1.5.1 Crystallographic and Electronic structure

1.5.1.1 Crystallographic Structure

Manganites with general formula $REMnO_3$ exhibit cubic perovskite structure and is shown in figure (1.6). The large sized RE trivalent ions occupy the A-site with 12-fold oxygen coordination. The smaller Mn ions are located at the centre of an oxygen octahedron. They occupy the B-site with 6-fold coordination. The structure of $RE_{1-x}AE_xMnO_3$ oxides is close to that of the cubic perovskite (figure 1.6). Here the divalent AE ions occupy in the A site, the same site where trivalent ions RE occupies. Mn ions located at the B site exists in the mixed-valence state Mn^{3+}/Mn^{4+}. For the stoichiometric oxide, the proportions of Mn ions in the valence states 3^+ and 4^+ are respectively, $1 - x$ and x. The structure of manganites is governed by the tolerance factor $t = (r_A + r_O)/\sqrt{2}(r_B + r_O)$. The perovskite structure is stable for $0.89 < t < 1.02$ and $t = 1$ corresponding to the perfect cubic closely packed structure. Generally, t differs appreciably from 1 and the manganites have at least a lower rhombohedral symmetry or orthorhombic structure at low temperatures.

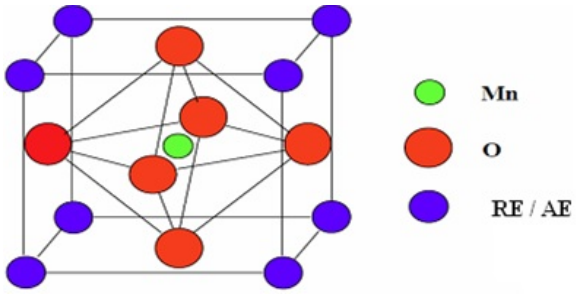

Figure 1.6: Schematic view of perovskite building block of $RE_{1-x}AE_xMnO_3$. RE and AE occupy the A-sites and manganese occupies the central B-site.

1.5.1.2 Electronic structure

In MnO_6 octahedron complex of manganites, any hopping from one Mn to another is via a bridging oxygen. The geometry of the local Mn-O-Mn

bond plays a key role in hopping. Considering the electronic levels of Mn atom in the octahedral coordination, five degenerated orbital states are available for an isolated 3d ion to the 3d electrons with l = 2. The five fold degenerate orbitals d_{xy}, d_{yz}, d_{xz}, $d_{x^2-y^2}$ and $d_{3z^2-r^2}$ are shown in figure (1.7).

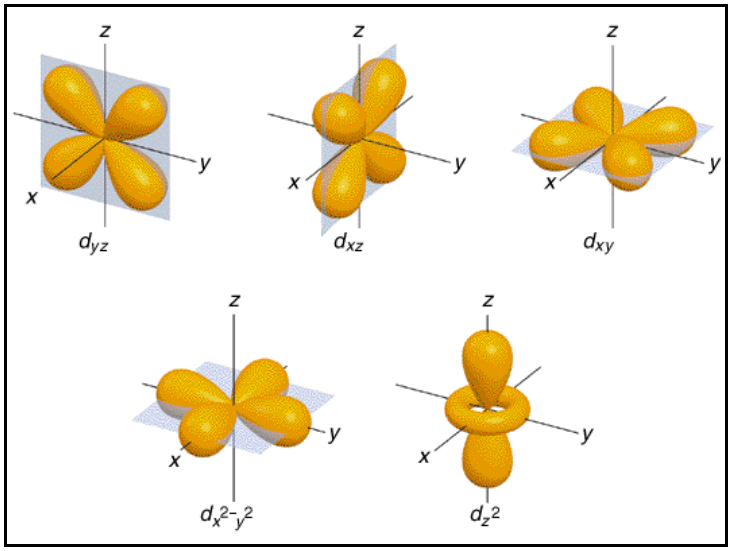

Figure 1.7: 3d orbitals

1.5.2 Crystal Field Splitting

When a transition-metal atom is surrounded by anions in a solid, the energies of the transition-metal d electrons are affected by their environment in the crystal lattice. Those electrons that are closest to the negative anions experience an unfavorable Coulomb repulsion compared with those that are geometrically distant from the anions. The electrostatic environment provided by the anions is called the crystal field. In a crystal, the degeneracy is partly lifted by the crystal field. For the MnO_6 octahedron, the chains of O-Mn-O planes can be assumed to be as directed along the three cartesian axes as shown in figure (1.8).

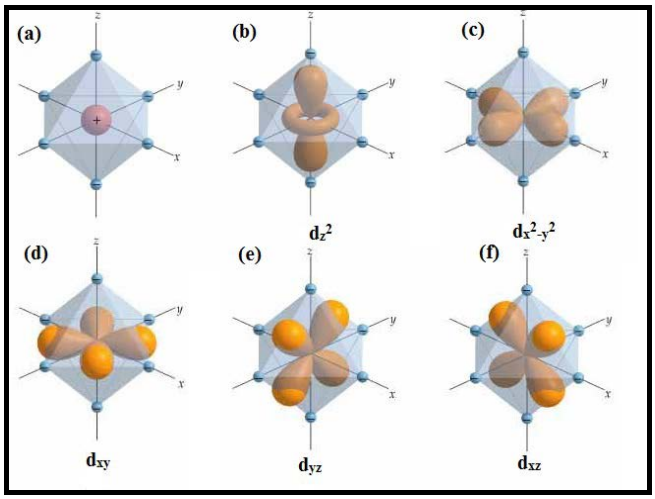

Figure 1.8: (a) octahedral array of negative charges approaching a metal ion. (b-f) d orbital orientation with ligand oxygen atoms

The O^{2-} ions forms the crystal field enclosing the Mn ions. All the 5 d orbitals of Mn ions will no longer have the same energy as in free ion as the relative energies of the d orbitals are controlled by the repulsive energy of the oxygen anion complex. The d orbitals, d_{xy}, d_{xz}, d_{yz} (π bonding orbitals) are oriented in between either of the two cartesian axes (i.e, in the empty space between the oxygen atoms) while the $d_{x^2-y^2}$ and d_{z^2} orbitals (σ bonding orbitals) point towards the axes. As a result, there exists large coulomb repulsion from the oxygen anions to $d_{x^2-y^2}$ and d_{z^2} orbitals and hence their energy will be raised compared to the other three d orbitals and it is called crystal field effect or distortion. The π bonding orbitals after the distortion forms the symmetric class t_{2g} and the σ bonding orbitals as e_g . Thus the five d-orbitals are split by a cubic crystal field into three t_{2g} orbitals and two e_g orbitals. The energy split between the lowest t_{2g} level and the highest e_g level is given by the splitting energy term Δ which equals $\frac{5zq}{3a^5}\langle r^4 \rangle$, zq denotes the charge of Oxygen ion , a is Mn- O distance and r is the distance of the electron to the central Mn ion. The magnitude of Δ varies

between 1-2eV [68-69]. For the Mn^{3+} and Mn^{4+} ions in MnO_6 octahedra, the intra atomic correlations ensure parallel alignment of the electron spins (first Hund's rule); the corresponding exchange energy of about 2.5 eV being larger than the crystal field splitting Δ, Mn^{3+} is $3d^4$, $t_{2g}^{3\uparrow}e_g^{\uparrow}$ with $S = 2$ whereas Mn^{4+} is $3d^3$, $t_{2g}^{3\uparrow}$ with $S = 3/2$.

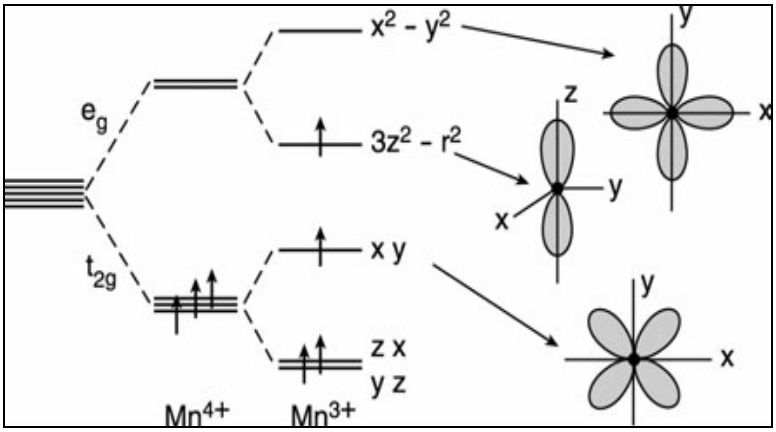

Figure 1.9: Energy levels and orbitals of Mn^{4+} and Mn^{3+} in a crystal field of octahedral symmetry. Adopted from reference [38].

1.5.3 Jahn - Teller Distortion

The Jahn - Teller effect occurs in those materials having partial electronic occupation in t_{2g} or e_g symmetric classes. This phenomenon was put forthby Herman Jahn and Edward Teller in 1937 to explain the instability of a non-linear system in a degenerate energy state. Jahn - Teller states that a non-linear system with a degenerate energy state will undergo spontaneous distortion so as to split its energy states and removes its degeneracy.

In an octahedral crystal field, the 5 fold degeneracy of 3d orbitals is split into two sets of orbitals, namely e_g and t_{2g}. Jahn - Teller distortion is energetically favourable if either of the e_g or t_{2g} sets is partially occupied. In Mn^{3+} ion, after the field splitting, 3 out of 4 electrons of Mn^{3+} occupy the t_{2g}

set and one electron in the e_g set make the Mn^{3+} ion Jahn Teller active. The single e_g electron can occupy either the $d_{x^2-y^2}$ or the d_{z^2} orbital with equal probability. Since the system is electronically degenerate, the orbitals are asymmetrically occupied and they experience more energy. In order to get rid of this extra energy, the system tries to lower the overall symmetry of the molecule by distorting the octahedra along the z axis. The octahedron elongates along the z axes and compresses along the x and y directions. The elongation and compression greatly affect the degeneracy of e_g and t_{2g} orbitals as - d_{z^2} will be lower in energy than $d_{x^2-y^2}$ orbital similarly the d_{xz}, d_{yz} orbitals will have lower energy than d_{xy}. This structural distortion introduces strain in the lattice. The single electron of the e_g set occupies the d_{z^2} level and hence the raised orbital is unoccupied and this leads to lowering of electronic energy. The magnitude of the Jahn -Teller distortion is determined by the balance between the lattice strain energy and the electronic energy for attaining energy stabilization. This distortion can affect the electrical and magnetic properties of the material [70].

Thus in manganites, degeneracy of the e_g and t_{2g} levels is lifted for an axial elongation of the oxygen octahedron. Although the energy of Mn^{4+} remains unchanged by such a distortion, the energy of Mn^{3+} is lowered. Thus, Mn^{3+} has a marked tendency to distort its octahedral environment in contrast to Mn^{4+}. This Jahn–Teller distortion is relatively effective in the lightly doped manganites, i.e. with a large concentration, 1-*x*, of Mn^{3+} ions; the Jahn–Teller distortions are not independent from one Mn^{3+} site to another (cooperative Jahn– Teller effect). When the Mn^{4+} content increases, the Jahn–Teller distortions are reduced and the stabilization of the $3z^2 - r^2$ e_g orbital becomes less effective. However, in a large number of manganites, the e_g orbitals of two types, $3z^2$-r^2 and x^2- y^2 are not occupied by the e_g electrons of Mn^{3+} at random and an orbital order is achieved and they greatly

affect its magnetic properties [68]. This Jahn-Teller distortion plays a key role in the structural phase diagram of the perovskite manganites and has a profound influence on the electronic and magnetic properties of materials.

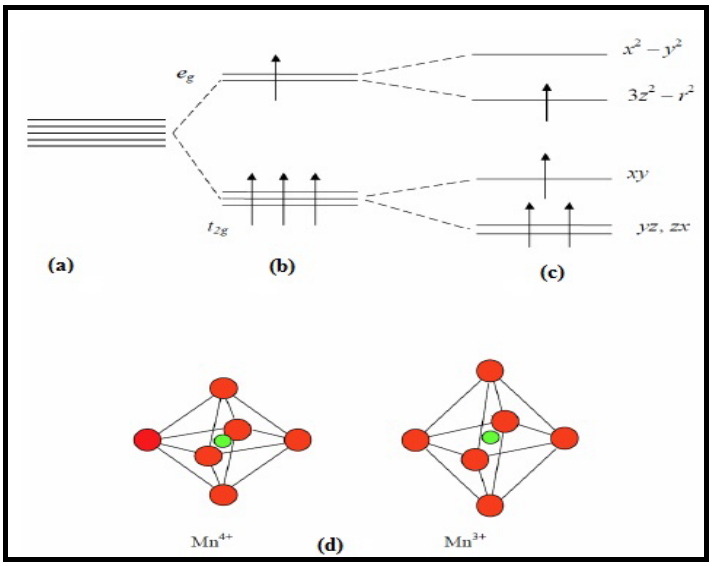

Figure 1.10: A schematic diagram showing the relative energies of the Mn 3d orbitals (a) in isolation, (b) in an octahedral environment such as the MnO_6 octahedra, and (c) after undergoing a Jahn-Teller distortion. (d) The shape of the MnO_6 octahedron for $Mn^{4+}$and Mn^{3+} ions. Adopted from reference [37].

1.5.4 Magnetic Interaction

Earlier Jonker and Van Santen have found an empirical correlation between electrical conduction and ferromagnetism in certain compounds of manganese with perovskite structure [50-51]. The magnetic properties of manganites are largely determined by transfer of electrons between the manganese and oxygen orbitals that point towards each other. The direct overlap between the atomic manganese orbitals is small and the magnetic interaction is mediated by intervening O '2p' electrons. The magnetic properties of manganites are governed by the exchange interaction between the Mn ion spins. There are two important interactions, namely double exchange and superexchange.

1.5.4.1 Double Exchange

Zener has interpreted the correlation between electrical conduction and ferromagnetism in manganites as the exchange interaction between the d shells of Mn ion spins [55,70]. This quantitative relation between electrical conductivity and the ferromagnetism are found to arise from a double exchange process. Double exchange mechanism explains the ferromagnetic ordering in mixed valence manganites. In double exchange process, Zener proposed a mechanism of electron spin interaction arises from the oxygen mediated coupling of two Mn ions of different valence states. The magnetic behaviour in the case of doped manganites is due to the simultaneous transfer of an electron from a Mn^{3+} 3d e_g orbital to an O^{2-} 2p orbital and transfer from the same oxygen 2p to a manganese 3d e_g orbital on an adjacent Mn^{4+} ion as shown in figure (1.11). Hopping of electrons between Mn ions occurs only if spins of two adjacent Mn ions are parallel else Hund's rule would be violated. Hund's rule demands the occupancy of electrons with same spins in the d orbitals of Mn^{3+} and Mn^{4+} ions. This leads a ferromagnetic arrangement of the e_g electrons and hence exhibiting high conductivity.

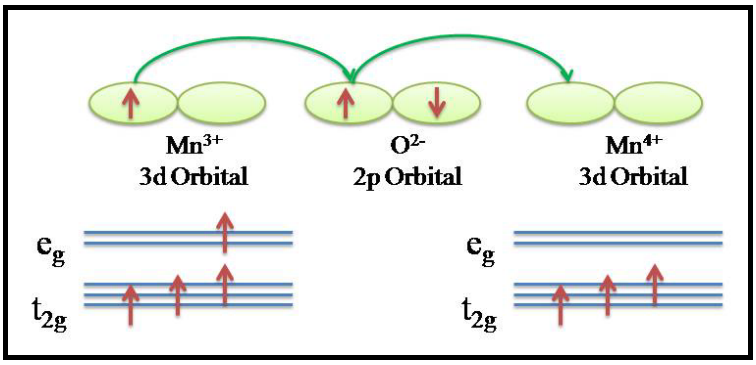

Figure 1.11: Double exchange mechanism between Mn^{3+} and Mn^{4+} ions

Consider a system of two Mn ions of different valence states separated by an O^{2-} ion. Because of Pauli's exclusion principle, both

electrons involved in the exchange must have the same spin. Let ψ_1 and ψ_2 be the wave functions representing the configuration of the system before and after the electron transfer as follows:

$$\Psi_1 = Mn^{3+}O^{2-}Mn^{4+} \quad (1.8)$$

$$\Psi_2 = Mn^{4+}O^{2-}Mn^{3+} \quad (1.9)$$

Since the spins of two Mn d shells are pointing in the same direction, states ψ_1 and ψ_2 are degenerate and hence no activation energy is required for electron hopping. With the hopping of an itinerant electron takes place from Mn^{3+} to Mn^{4+} via oxygen this degeneracy will be lifted and overall energy of the states will be lowered. An electron transfer from Mn^{3+} to Mn^{4+} occurs as a result of simultaneous double transfer of electron from Mn^{3+} to O^{2-} and then from O^{2-} to Mn^{4+}. Double transfer of electrons results in a ferromagnetic ordering between Mn ions and the mechanism is called double exchange, which accounts for both ferromagnetism and metallicity. In a semi classical treatment, the double exchange leads to a specific dependence of electron transfer between Mn ions on the angle (θ) between their core magnetic moments.

$$t = t_0 \cos(\theta/2) \quad (1.10)$$

1.5.4.2 Superexchange

Superexchange was first proposed by Hendrik Kramers in MnO crystals. In superexchange, indirect magnetic interaction through the oxygen ion by means of Mn ions of similar or dissimilar charges occurs. Depending on the occupancy of Mn orbitals, this magnetic interaction leads to either antiferromagnetic or ferromagnetic alignment of spins in which conduction is poor. If the two Mn ions are in the same valence state, then the arrangement of spins and orbitals in superexchange will lead to an AFM alignment as shown in figure (1.12). The super exchange mechanism between Mn^{3+}-O^{2-}-Mn^{3+} and Mn^{4+}-O^{2-}-Mn^{4+} pairs is shown in figure (1.12).

The orbitals involved in the case of Mn^{3+}-O^{2-}-Mn^{3+} are the vacant Mn 'e_g' orbital and the occupied O '2p' orbital and the O 2p electron is shared between the two ions [53, 71].

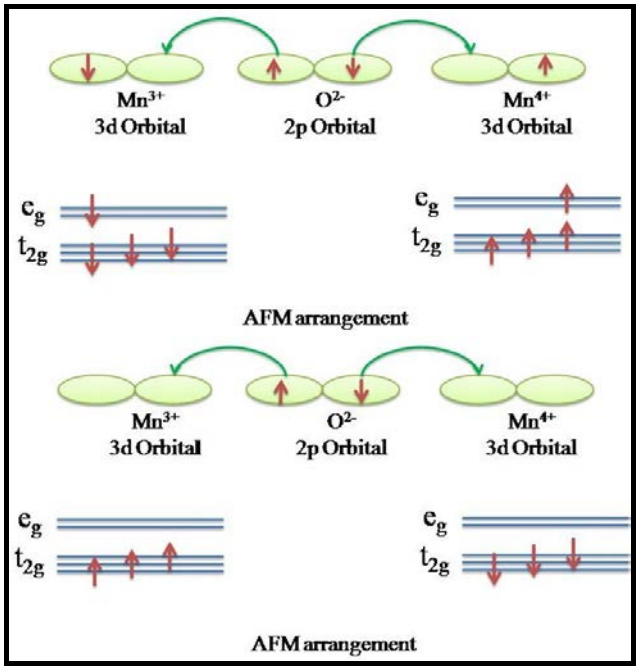

Figure 1.12: Superexchange mechanism between Mn^{3+}-O^{2-}-Mn^{3+} and Mn^{4+}-O^{2-}-Mn^{4+} pairs

For Mn^{3+}, core t_{2g} electrons and permanent e_g electron will be spin aligned due to strong Hund's coupling between them. So the spin of the transferred electron from oxygen 2p orbital needs to be of opposite to satisfy Pauli's exclusion principle. Since the two electrons from the oxygen anion have opposite spins, such a process results in an antiferromagnetic alignment between similar Mn^{3+}or Mn^{4+} ions. But for Mn^{3+}-O^{2-}- Mn^{4+}, an empty Mn^{4+} e_g orbital is pointing towards a half full Mn^{3+} e_g orbital, which will lead to a ferromagnetic alignment. This is shown in figure (1.13). This is the case of insulating ferromagnets. Thus superexchange will always results in an insulating state.

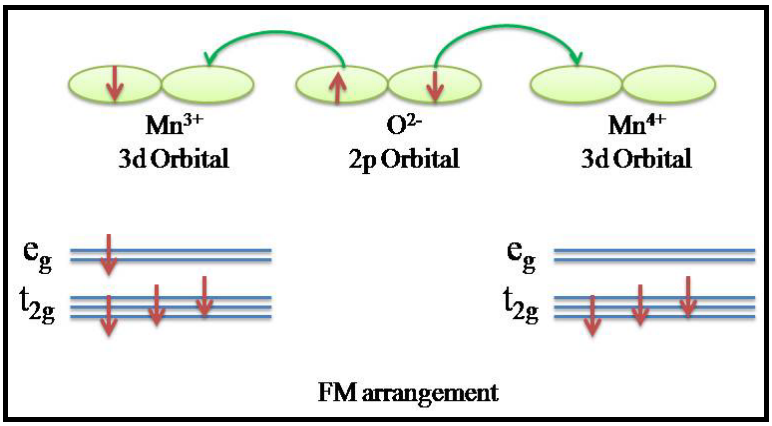

Figure 1.13: Superexchange mechanism between Mn^{3+}-O^{2-}—Mn^{4+}

1.5.5 Electron-Phonon Coupling

Millis *et. al* pointed out that the double exchange alone cannot explain the high resistivity of manganites and that electron-phonon interaction is important. Electron-phonon coupling arising from the Jahn-Teller (JT) splitting of the manganese 3d levels [72]. Oxygen octahedron undergo spontaneous distortion for reducing coulomb repulsion energy between the e_g electron and oxygen. If the oxygen octahedron is compressed by symmetrically pushing out the four planar oxygen atoms, it will favour the occupation of $e_g d_{x^2-y^2}$ orbital, while elongation favors the occupation of elongated $e_g d_{3z^2-r^2}$ orbital by symmetrically pushing out two apical oxygen atoms. These two distortions are shown in figure (1.14). When the distortion became prominent charge carriers are well trapped by elastic distortion, hence moving e_g electrons may be polarons comprising of electrons and the local Jahn - Teller distortion. This elastic distortion in lattice is phonons. Thus phonons have much importance in manganites towards the formation of polarons. The effective coupling could be above the critical value when the temperature is higher than T_C which in turn leads to the insulating behaviour due to electron localization and would be smaller

than the critical value when temperature is below T_C and thus exhibit metallic behaviour [73-74].

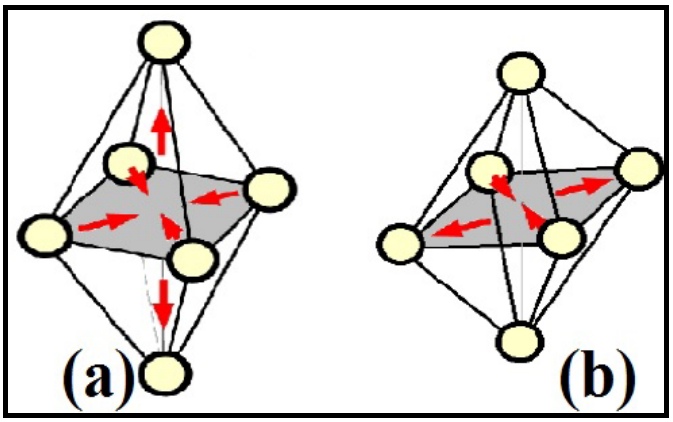

Figure 1.14: Important phonon modes that couple with the electrons. Jahn-Teller distortions of the octahedral, in which (a) apical and (b) the planar oxygen atoms are pushed out.

1.5.6 Electron –electron and electron- magnon interaction

In addition to double exchange and electron phonon interactions one cannot rule out the influence of electron-electron interactions that stabilizes the FM phase. Electron-electron interaction arises from the coulombic repulsion between Mn^{3+} e_g electron.

Kubo and Ohata found that the perfect spin polarisation of conducting electrons makes a qualitative change in the scattering of charge carriers by magnon-electron interactions [75]. In ferromagnets electrons are scattered by spin waves. The electron –magnon interactions introduce magnon drag.

1.5.7 Spin glass and Cluster glass

A spin glass is characterized by the presence of strong, competing magnetic interactions and randomness. The spin glass phase is generally formed in a frustrated system where FM and AFM phases are randomly distributed. The magnetic moments of these materials are frozen in an arbitrary state with short range magnetic order to form a magnetically

frustrated state at low temperature. When a spin glass is cooled down, collective freezing of magnetic moments occurs at a temperature called magnetic glass temperature T_g. Below this temperature, magnetic interactions are stronger compared to thermal activation. Hence these moments are immobile below T_g. The ground state of spin glass is an arrangement of magnetic moments with short range order so that they have a net magnetization. [76].

Magnetic clusters are formed when a ferromagnet is dispersed within an AFM matrix. In manganites, antiferromagnetic (AFM) Mn^{3+}-O-Mn^{3+} interactions compete with ferromagnetic (FM) Mn^{3+}-O-Mn^{4+} interactions. Several magnetic moments can be ferromagnetically coupled in a cluster which is surrounded by an environment with weaker ferromagnetic or AFM interactions. Thus FM clusters are present in AFM matrix. For a system of many clusters, the zero field ground state has no net magnetization since individual magnetization of clusters cancel. When the magnetic interactions between the clusters are strong enough, these clusters can freeze in a spin glass like state termed as cluster glass. Thus cluster glass is a type of spin glass which is formed in a magnetically frustrated system where FM and AFM clusters are randomly oriented and also the interaction between these pairs cannot be negligible. Usually the existence of spin glass or cluster glass state is mainly based on thermo magnetic irreversibility [77].

1.5.8 Magnetoresistance

Manganites possess the unique property of magnetoresistance which is the property of a material to change the value of its electrical resistance when an external magnetic field is applied. The magnetoresistive (MR) ratio is defined as the ratio of the change in resistance when the field is applied to the resistance at zero field, that is,

$$MR = \frac{R_H - R_0}{R_0} \qquad (1.11)$$

where R_H and R_0 represents the resistance of the material in the applied field and zero field respectively. If a material has a large resistance in presence of field than in the absence of field, it is said to possess positive magneto resistance. If the field reduces the resistivity, the magneto resistance is negative. Magneto resistive materials are used in a number of commercially available technologies such as magnetic sensors, read component in magnetic recording heads and magnetic memories [68]. Depending on the percentage of change of magnetoresistance, they can be broadly classified into two: Giant Magnetoresistance (GMR) and Colossal Magnetoresistance (CMR).

1.5.8.1Giant Magnetoresistance (GMR)

The effect was first observed in the late 1980s by Baibich *et al* in metallic multilayers of iron/chromium [78]. Magnetic fields can induce change in resistance in multilayers of thin ferromagnetic metals separated by non-magnetic or antiferromagnetic metals. This phenomenon is known as GMR. Nobel Prize in Physics for the year 2007 was awarded to Albert Fert and Peter Gruenberg for the discovery of GMR [79].

GMR has led the way for the development of spin valves comprising of two magnetic layers with an intermediate non magnetic layer. Thickness of the intermediate layer guides the ferro/ antiferromagnetic alignment of the magnetic layers. GMR occurs when the thicknesses are chosen such that the adjacent layers are antiferromagnetic in zero applied field. These results in high resistance state as up spin electrons are scattered by regions of down spin magnetization and vice versa (figure 1.2). Then GMR effect works by

changing the relative magnetization directions between adjacent magnetic layers [62,68]. A typical spin valve is shown in figure (1.15).

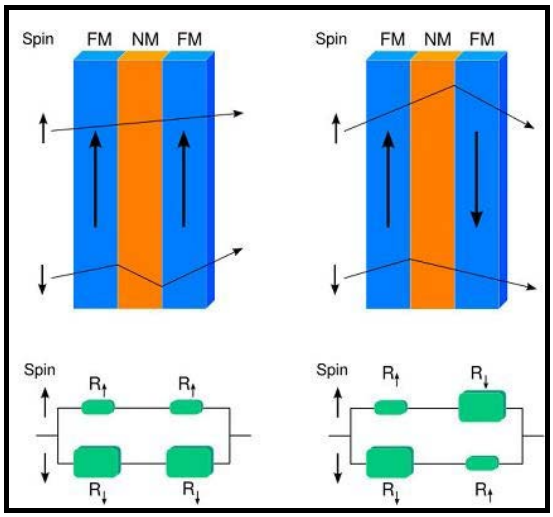

Figure 1.15: A typical spin valve

1.5.8.2 Colossal Magnetoresistance (CMR)

The phenomenon of colossal magnetoresistance (CMR) was first observed in 1994 by Jin *et. al* in $La_{0.67}Ca_{0.33}MnO_3$ films at 77 K as shown in figure (1.16). The term "colossal" was coined because of the very large change in resistance occurring during the transition from the insulating to a conducting state, on application of a magnetic field [68-74, 78-80]. Conventional metals also exhibit magnetoresistance but the change in resistance is nearly 5% while in manganites a gigantic decrease in resistance on the application of magnetic field is observed. Spin dependent scattering mechanism of the conduction electrons in metal oxides and suppression of such scattering by magnetic field were the features which led to CMR mechanism. CMR arises from strong coupling between magnetism and transport properties: Below the Curie temperature, the electrical resistivity shows metallic behavior and rapidly decreases with decreasing temperature [81].

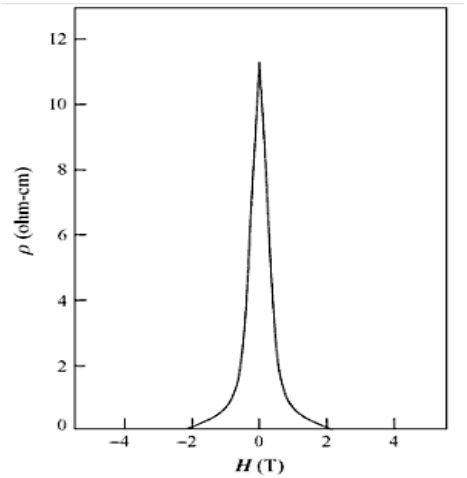

Figure 1.16: Change in resistivity as a function of applied magnetic field in La-Ca-Mn-O films at T=77K. Adopted from reference [68].

In CMR materials, as temperature decreases, the material undergoes a phase transition from ferromagnetic to paramagnetic/ antiferromagnetic. These transition take place nearly at same temperature of the order of a transition from metal to insulating state which is termed as M-I transition. Thus the material undergoes a phase transition from a paramagnetic insulating phase at high temperature to a ferromagnetic metal at low temperature and the M-I transition temperature is in the vicinity of magnetic transition from ferromagnetic to paramagnetic state (Curie temperature, T_C). A schematic diagram of two transitions is shown in figure (1.17) [62]. This indicates that magnetic and conduction behaviors are closely coupled. When the magnetic moments are not aligned (in the paramagnetic state), electrons cannot transfer between Mn ions without violating Hund's rule, and double exchange does not occur. However, an applied field causes a ferromagnetic phase transition with a corresponding increase in conductivity associated with the alignment of spins.

Thermoelectric power….

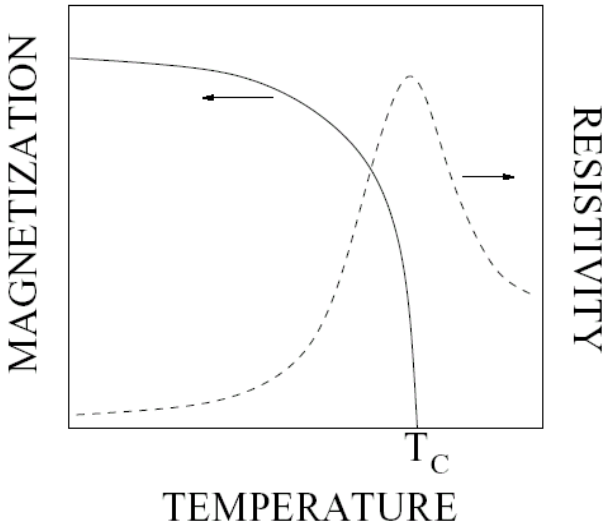

Figure 1.17: M-I transition and T_C

1.6 Types of manganites

The size mismatch of the ions substituted into the perovskite lattice causes a reduction of the Mn-O-Mn bond angles from 180^0 down to 160^0 and below. Thereby, the conduction bandwidth (W) is reduced due to the smaller orbital overlap. Bond length changes are another consequence of varied ionic radii, this additionally may influence W. Most manganites have a tolerance factor $t < 1$, that is, the ions on the RE site are too small. With increasing mean ionic radius of cation (both rare earth and divalent) $<r_A>$, one observes that both an increasing average bond angle (enhanced W) and also an increasing bond length. Based on the width of this conduction band, manganites are categorized into three: namely large bandwidth manganites intermediate bandwidth manganites and small bandwidth manganites [82]. Metal–insulator transition and the distance between the magnetic ions are strongly dependent on the bandwidth [77, 83]. The bandwidth increases when the magnetic ions are closer to each other and, on the other hand, the broader bandwidth enables the excitation of electrons to higher energy states. In manganites, a decrease of ionic radius distorts the crystal lattice. It is

important to notice that grouping according to bandwidths is closely related to the crystalline distortion of the compounds and the stability can be described by the Goldschmidt tolerance factor t [84].

1.7 Ordering phenomenon in manganites

When a crystal is formed from its atoms/molecules, their interaction energy (U) in the lattice depends on the mutual orientation of these molecules. The necessary minimum free energy is given by F=U-TS, which requires an ordering of the interacting molecules. At a particular temperature a phase transition to the disordered state, for which the entropy is maximum, takes place and this is order-disorder phase transitions. In coordination compounds, in addition to this order disorder phase transitions, displacive phase transitions (in which the atomic arrangement in the coordination centre itself changes) may also take place. These displacive transitions are directly related to the electronic structure. Thus the electronic structure of the coordination centre plays a key role and if different Jahn - Teller centres in case of manganites can interact and there will be an ordering of local deformations, which leads to macro deformation of the crystal as a whole. The ordering of the Jahn-Teller center distortions, called the cooperative Jahn-Teller effect can create new physical properties, including the formation of new crystal structures and structural phase transitions.

In manganites, there is close entanglement between the charge, spin and orbital degrees of freedom. Spatial long range replication of charge, spin and orbital degrees of freedom result in charge ordering, spin ordering and orbital ordering respectively at Mn sites. The relation between orbital ordering, spin ordering and charge ordering in the rare earth manganites is of great importance. These ordering depend on the size of divalent cation, AE, in $RE_{1-x}AE_xMnO_3$ and the extent of ordering on the x-T phase diagram will

vary from small bandwidth, intermediate bandwidth to large bandwidth. The Mn^{3+} orbitals and the associated lattice distortions leads to a long range order, giving rise to orbital ordering. The occurrence of charge ordering was first observed by Wollen Koehler and later examined by Jirak et al. [40, 85]. Ordering including A, CE type, G and C type AFM ordering exist. Orbital ordering can occur in both A- and CE-type AFM ordering, but they differ in detail. The CE-type AFM state is attained on cooling a ferromagnetic state or a charge-ordered paramagnetic state [86]. Different ordering phenomena in detail are explained below.

1.7.1 Orbital Ordering

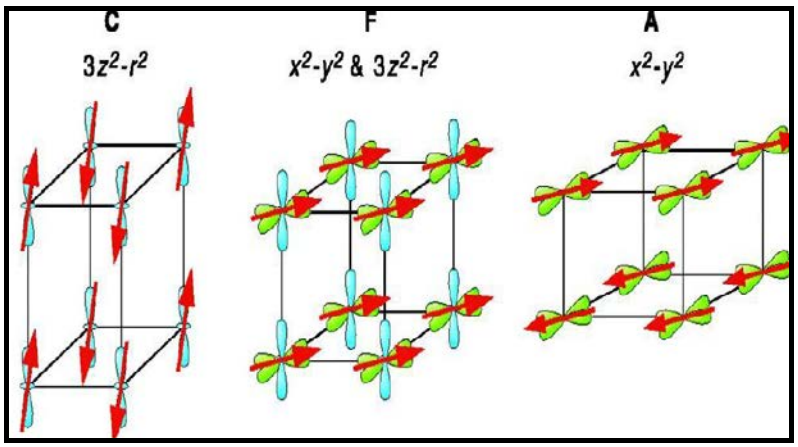

Figure 1.18: Different types of orbital ordering occurring in manganites [117].

When the d electrons occupy an asymmetric orbital, orbital ordering occurs at certain carrier concentration. Kanamori pointed out that carriers in manganites are strongly coupled to lattice distortions [87] and hence this ordering is coupled with Jahn-Teller distortion Thus Mn^{3+} orbitals associated with Jahn Teller distortions gives rise to orbital ordering. Orbital-ordering results in the anisotropy of the electron-transfer interaction [88-89]. This favors or detriment the double-exchange interaction or superexchange interaction in an orbital direction-dependent manner and hence leads to a complex spin-orbital coupled state. Orbital ordering can occur in both A- and

CE-type AFM ordering, but they differ in detail [86]. Different types of orbital ordering occurring in manganese perovskites are shown in figure (1.18).

1.7.2 Spin Ordering

Interaction with adjacent atoms allows to align the spin of the electrons in a specific fashion. Ferromagnetic order occurs when the spins are arranged parallel to each other and anti- ferromagnetic order (AFM) results when they are anti-parallel to one another. The anti- ferromagnetic order can take different configurations. The most common configurations observed in manganites are three types which are listed below and shown in figure (1.19).

A-type: The intra-plane coupling is ferromagnetic while inter-plane coupling is antiferromagnetic.

C-type: The intra-plane coupling is antiferromagnetic while inter-plane coupling is ferromagnetic.

G-type: Both intra-plane and inter-plane coupling are antiferromagnetic.

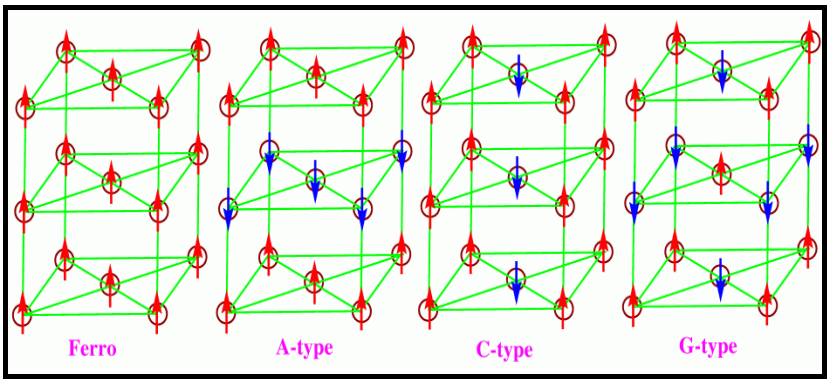

Figure 1.19: Different types of spin ordering in manganites

1.7.3 Charge Ordering

Charge ordering also known as Wigner crystallisation is controlled by interatomic coulomb interactions. When the inter electronic Coulomb

interaction is comparable with the conduction- electron bandwidth (W*)* for particular occupancies of the d band, the mobile d electrons are localized on certain manganese ions to form a regular lattice. Charge ordered (CO) state is generally observed in half doped manganites with relatively narrow bandwidth system. Charge ordering arises due to the real space ordering of charge carriers into specific lattice sites below a certain temperature T_{CO} and this ordering occurs when their long range coulomb energy overcomes their kinetic energy. Since charge ordering is based on localization of charge carriers, usually there occurs a competing interaction to ferromagnetic double exchange and promotes insulating behaviour and antiferromagnetism.

Wollen and Koehler determined different magnetic structures for $La_{1-x}Ca_xMnO_3$ manganites in a remarkably complete neutron diffraction study as a function of Mn^{4+} content [40]. At half filling, *x*=0.5, Mn^{3+} and Mn^{4+} are equal number, an ordering of Mn^{3+} and Mn^{4+}species occurs over the lattice leading to charge ordering. Ordering of $Mn^{3+}$and Mn^{4+} ions in alternate (100) (figure(1.20.a)) and (111) planes (figure (1.20.b)) leads to formation of high energy C type antiferromagnetic magnetic lattice and ordering along (110) planes corresponds to low energy CE type antiferromagnetic magnetic lattice (figure (1.21.b)) [40,54]. Tokura et al. showed that the robustness of the charge/orbital ordering at x = 1/2 critically depends on the W (band width), which is understood as a competition between the DE interaction and the ordering of Mn^{3+}/Mn^{4+} ions with a 1 : 1 ratio accompanied by simultaneous ordering of e_g orbital of Mn^{3+} ion [90]. Even though charge ordering is usually observed in half filling, depending on the size of rare earth and divalent cations, it is found in various compositions in the range of $0.3<x<0.75$ [86, 91-94]. Charge Ordering is sensitive to the average size of A site cations, pressure, magnetic and electric fields. For small A size cations, CO state is the ground state. The sensitivity

of CO state to the average size of the A site cations will be discussed in detail in section (1.8.2).

In addition to charge ordering, there exists orbital ordering through Jahn-Teller mechanism. Hence orbital ordering has also been observed for numerous insulating manganites. Thus Charge ordering (CO) phase originates from Coulomb potential, orbit ordering, and Jahn-Teller effect [95]. Also charge ordering, orbit ordering and spin ordering are closely related to transport property. Charge order, orbit order and spin order are coupled to one another in the antiferromagnetic system in charge ordering [96]. Manganites near half doping (x ~ 0.50), having equal numbers of Mn^{3+}/Mn^{4+} ions with a peculiar orbital and spin ordering is shown in figure (1.22). The spin ordering is *CE*-type in which FM chains are arranged in the z-direction [75, 97]. Charge is also stacked in the *z*-direction implying that there may be some interaction closely competing with Coulomb repulsion.

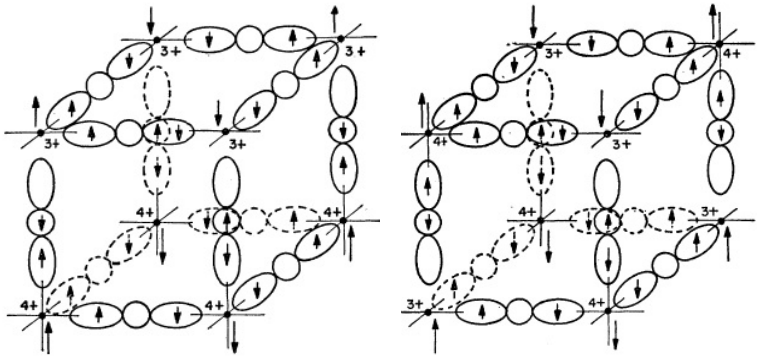

Figure 1.20: Ordering of Mn^{4+} and Mn^{3+} ions in alternate (a) (111), (b) (100). Adopted from reference [54].

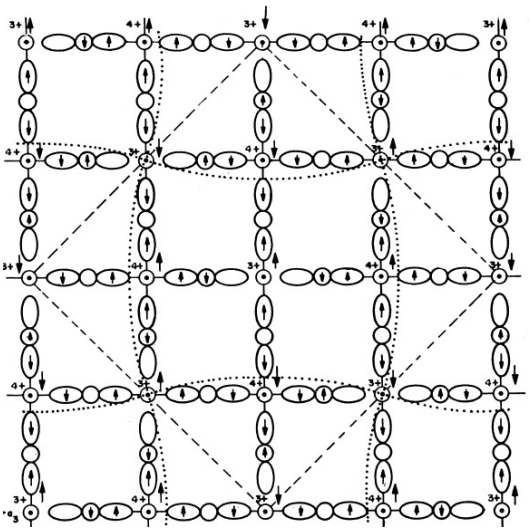

Figure 1.21: ordering of Mn^{4+} and Mn^{3+} ions in alternate (110) planes. Adopted from reference [54].

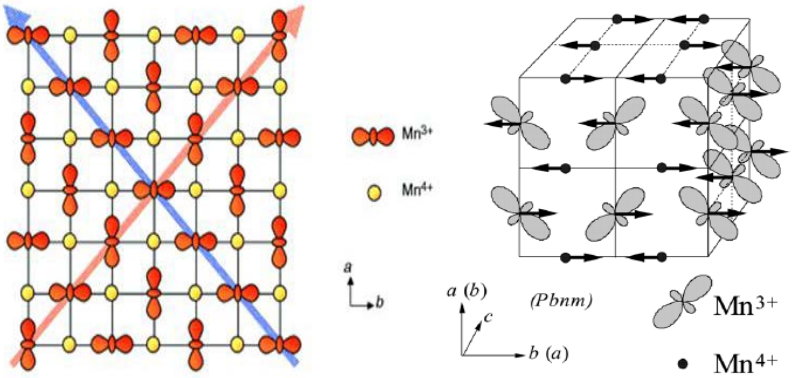

Figure 1. 22: (a) Charge and orbital ordering in a-b plane (taken from [88]) and (b) their ordering in the z direction (taken from [37]).

1.8 Bandwidth dependence

1.8.1 Effect of doping, average cation size and bandwidth

The physical properties of manganites having general formula $RE_{1-x}AE_xMnO_3$ (RE- rare earth, AE-alkaline earth metal) depends on two main parameters such as the doping level and average size of the A-site cations, $<r_A>$. In the undoped $REMnO_3$, all Mn ions are in +3 state which has one

electron in the e_g level. Mn in a fully doped $AEMnO_3$ exists in tetravalent state. Substitution of rare earth element by divalent cation produces mixed valent (Mn^{3+}-Mn^{4+}) manganites, $RE_{1-x}AE_xMnO_3$. Depending on the value of x, the composition may be canted antiferromagnetic (CAF), ferromagnetic insulator (FMI), ferromagnetic metallic (FMM), charge ordered (CO) and antiferromagnetic (AFM). When divalent cations are doped, antiferromagnetic Mn^{3+}-O-Mn^{3+} begins to compete with ferromagnetic Mn^{3+}-O-Mn^{4+}. Maximum ferromagnetism and metallicity is obtained in the vicinity of x=0.3. Out of various compositions in the phase diagram, the composition when x= 0.5 is most interesting [98-99]. Here, Mn^{3+} and Mn^{4+} are equal in number at this composition and hence ordering of Mn^{3+} and Mn^{4+}species occurs over the lattice, leading to charge ordering and co-existence of antiferromagnetism and ferromagnetism. Below this composition, FM phases are more favourable and above this composition, AFM phases are predominant.

The average radius of the A-site cations, $<r_A>$ affects a distortion of the perovskite lattice. Decreasing $<r_A>$ increases the lattice distortion which in turn increases the tilting of MnO_6 octahedra which makes the narrowing of the bandwidth for e_g band. The charge-ordering transition is also highly sensitive to $<r_A>$. This narrowing of bandwidth destabilizes the double exchange and manifests itself in the lowering of the metallic and ferromagnetic transition temperatures. The large difference between the ionic radii of A site cations has a major say in determining the transport properties.

1.8.2 Bandwidth effect on charge ordering

In manganites, the width of conduction band formed by the hybridization of manganese e_g level and oxygen p level is termed as bandwidth. All Mn-O-Mn bond angles in the parent compound $REMnO_3$ are 180^0. Any deviation from this, either by lengthening or bending reduces

the orbital over lapping and hopping amplitude of the itinerant e_g electron. The undoped manganite $REMnO_3$ is hole doped using alkaline earth elements AE. When the rare earth ions are replaced by divalent cations, the size mismatch of the ions tends the oxygen octahedra to tilt. This suppresses the amplitude of hopping for e_g electrons as ~ $\cos^2\theta$, where θ is the Mn-O-Mn bond angle and reduces the bandwidth [62]. Thus the size mismatch of the ions substituted into the perovskite lattice causes a change in the bond angles and thereby, the conduction bandwidth. The mean ionic radius of A site cation is given by $\langle r_A \rangle = (1/2)\ (r_{RE}+r_{AE})$. The bandwidth reduces with reduction in the mean cation radius. Decrease in the bandwidth enhances the tendency to localise the e_g electrons through electron-phonon interaction. Wider the bandwidth, the manganite should be more metallic. Furthermore, the suppression of kinetic energy weakens the ferromagnetic exchange and favours the appearance of antiferro-magnetic order.

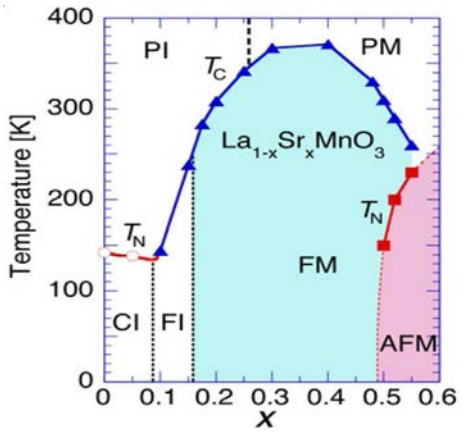

Figure1.23: Phase diagram of $La_{1-x}Sr_xMnO_3$. FM, AFM, PM, CI, FI and PI, denote FM metal , AFM insulator, paramagnetic metal, spin-canted insulator, FM insulator and paramagnetic insulator states, respectively. T_C is the Curie temperature and T_N is the Neel temperature. Adopted from references [99-101].

As bandwidth increases, magnitude of hopping amplitude for e_g electrons is large which is favourable for double exchange and hence

exhibits ferromagnetic behaviour. Their Curie temperature T_C and metal to insulator transition temperature is relatively large (eg: $La_{1-x}Sr_xMnO_3$). Increasing $<r_A>$ increases the bond angle and e_g bandwidth. From the phase diagram of $La_{1-x}Sr_xMnO_3$ [taken from [99-101]] shown in figure (1.23), it is observed that lanthanum strontium mangnaites has a ferromagnetic metallic ground state at half doping. The intermediate bandwidth manganites such as $La_{1-x}Ca_xMnO_3$ (LCMO) have some characteristics such as robust ferromagnetic phase similar to that of large bandwidth manganites, but their Curie temperature is relatively small. It shows strong deviations from double exchange mechanism and more tendency for charge ordering. CE type magnetic order is reported for x=0.5 [72, 102]. Small bandwidth manganites (eg: $Pr_{1-x}Ca_xMnO_3$) exhibit maximum deviation from double exchange ideas. Phase diagram of $Pr_{1-x}Ca_xMnO_3$ taken from [37] is shown in figure (1.24). Metallic ferromagnetic state is not stabilized and in place a ferromagnetic insulator phase is present in large region.

Half doped large bandwidth manganites prefer to be ferromagnetic because the energy gain from electron delocalization is larger than that obtained by localization. Hence charge ordering is not stabilized in large bandwidth manganites. With decreasing bandwidth this state is more and more stabilized due to their increasing tendency of localization [63]. For the smallest bandwidth manganites, this state has a broad window of stability. Even though CO phase is expected only for half doping, systematic increase in stability of CO phase with decreasing bandwidth leads to the existence of this phase for a wide range of doping (x = 0.3-0.7) for low band width manganites [82, 85]. The charge-ordering transition T_{CO} is also highly sensitive to $<r_A>$. The transition temperature decreases with decreasing rare earth size and is generally attributed to an increased tilting of the MnO_6 octahedra.

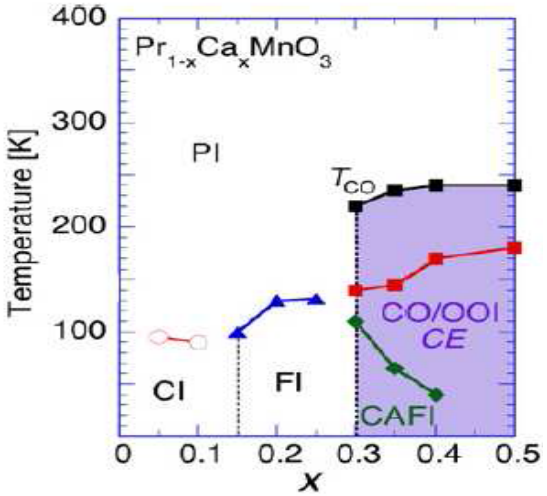

Figure 1.24: Phase diagram of (a) $Pr_{1-x}Ca_xMnO_3$. AFI, COI, CAFI denote antiferromagnetic insulator, charge/orbital-ordered insulator, canted antiferromagnetic insulator states, respectively. Adopted from reference [37].

1.9 Effect of nano structuring on thermoelectric power

Experiments performed on the dimension reduced structures have shown a steadily increasing ZT. These low dimensional structures do not have the same properties as that of their bulk counterpart. The quantum mechanical effects such as electron confinement and tunneling are considered through the modification of density of states (DOS) [103]. When the grain size decreases to nanometric scales, the density of electronic states (DOS) is increased significantly due to quantum confinement [24]. Quantum confinement enhances DOS which in turn leads to the significant improvement in power factor $S^2\sigma$.

The performance characteristic ZT can be improved by reducing thermal conductivity. It is known that thermal transport in low dimensional structures of semiconductor materials occur primarily through phonons which are associated with vibrations of the crystalline lattice. For the largest thermoelectric power, phonon scattering should be high, while electron scattering should be low. This can be achieved by reducing the average grain

size comparable to or lower than the phonon mean free path while it should be greater than electron mean free path [104]. Since the grain size is greater than the mean free path of electrons, electrons are confined while phonons are not confined so that phonon scattering due to grain boundaries (GB) is larger. Besides this, thermal conductivity can be further reduced through the introduction of scattering at different scales. For instance, atomic scattering of short wavelength phonons by compositional fluctuations, surface roughness for longer wavelength phonons, and boundary scattering [103]. In order to suppress lattice thermal conductivity and also to enhance GB-phonon scattering, low dimensional nano structuring techniques are required. There are numerous reports on the improvement of power factor by introducing interface scattering of phonons by grain boundaries due to nano structuring [14, 105-106]. Unlike bulk, scattering of phonons by interfaces has to be taken into account in low dimensional structures. By various studies it was found that an increased phonon- boundary scattering and a reduced phonon thermal conductivity lead to a higher thermoelectric figure of merit.

Thus phonon transport and the scattering of phonons at interfaces and boundaries play a vital role in enhancing the ZT of low dimensional nano structures. The favourable influence of size effects on phonon transport leads to an improved figure of merit. Besides phonon and electron scattering, electron - magnon scattering should also be considered while nano engineering. Such nano structuring influences the mobility of charge carriers and eventually permits tailoring of S, κ and σ.

1.10 Motivation for the present study

Eco friendly thermoelectric materials are promising for energy conversion and have attracted the attention of scientists and engineers. A large value of Seebeck coefficient, high electrical conductivity and low

thermal conductivity are necessary to realize a high performance thermoelectric material. The best known thermoelectric materials are phonon-glass electron – crystal (PGEC) system where the phonons are scattered within the unit cell by the rattling structure and electrons are scattered less as in crystals to obtain a high electrical conductivity [4]. The best thermoelectric materials are between metals and insulators. That is, semiconductors with a carrier concentration between 10^{19} and 10^{21} carrier/cm^3 [4].

Strongly correlated transition metal oxides exhibit large thermoelectric power [13]. In strongly correlated systems, electrons are localised in that they exhibit intermediate properties between metals and insulators. Earlier it was reported that correlated semiconductors and Kondo insulators containing rare earth or transition metal ions were found to be good for production of large thermoelectric power [107-109]. Perovskite manganites are excellent electron correlated systems possessing different phase states and transitions with a close correlation between structure, electron transport and magnetic properties. Strongly correlated systems like perovskite manganites, characterized by their narrow localized band and hoping conduction, were found to be good candidates for thermoelectric applications. These materials are strong electron correlated systems with close coupling between lattice, electron spin and charge transport. They are reported to be potential materials for thermoelectric applications. They satisfy the requirement of having low lattice thermal conductivity. Cong *et. al* reported that the substitution of rare earth induce the fall of thermal conductivity due to phonon lattice interaction [110]. Manganites with both rare earth and alkaline earth metallic cation are thought to be suitable for thermoelectric power investigation, as its thermal conductivity is reduced due to the rattling of rare earth atom. Here, large thermal motion or rattling

of rare earth atoms (RE) with localized magnetic moments is believed to be responsible for low thermal conductivity of these compounds. The 4f levels in these compounds, lying near the Fermi energy, create large density of states at the Fermi level and hence they can exhibit a high Seebeck coefficient.

When a rare earth ion RE in $REMnO_3$ is substituted with divalent cation AE, the electrical and magnetic properties vary with degree of substitution and ionic radii of both rare earth and doping atoms. The size mismatch of the ions substituted into the perovskite lattice modify the Mn-O-Mn bond angles and thereby, the conduction bandwidth. Based on bandwidth, manganites are classified into three. They are large, intermediate and low bandwidth manganites. The bandwidth increases when the magnetic ions are closer to each other and the broader bandwidth enables the excitation of electrons to higher energy states.

In the region where x=0.5, Mn^{3+} and Mn^{4+} are equal in number. Goodenough has reported that at x=0.5 ordering of Mn^{3+} and Mn^{4+}species occurs over the lattice leading to charge ordering and co-existence of antiferromagnetism and ferromagnetism [54]. Below this composition FM phases are more favourable and above this composition AFM phases are favourable. As FM and AFM phases co-exist for charge ordered composition x=0.5, strong competition between these magnetic phases develops and thus arises a magnetically frustrated glass state, spin glass. Hence the composition x = 0.5 is critical and physical properties close to this composition is unique.

Tokura showed that the robustness of the charge/orbital ordering at x = 1/2 critically depends on bandwidth [111]. In large bandwidth manganites, atomic orbitals are strongly over-lapping and valence electrons are more delocalized, whereas charge-ordering is a fully localized electron phenomenon. Hence charge ordering (CO) is absent in large bandwidth

manganites. With decreasing bandwidth this state is more and more stabilized due to their increasing tendency of localization and hence CO tendencies are present for intermediate bandwidth manganites at x=1/2 [63]. For low bandwidth compounds, their magnetization, conductivity and magnetic ordering temperatures are lower when compared to manganites based on lighter rare earths. The replacement of lighter rare earth elements in mixed valent manganites by heavier rare earth elements induce lattice distortion associated with modification of tolerance factor which in turn influence the double exchange mechanism and hence influence magnetic interactions. Due to smaller ionic radii of heavier rare earth R atom, Mn-O-Mn bond distribution is maximum and hence a weak double exchange results [112]. Thus a stable charge ordered phase exists over a wide range of doping (x = 0.3 - 0.7) in small bandwidth manganites [113].

It has been pointed out that various effects such as localization due to charge ordering, short range magnetic ordering due to spin glass, electron – electron correlation, electron magnon scattering and electron phonon scattering strongly modify the temperature dependence of transport properties especially thermoelectric power.

Recently Sagar *et.al* observed colossal thermoelectric power in $Gd_{0.5}Sr_{0.5}MnO_3$ and the observed colossal thermoelectric power was explained based on charge and orbital ordered spin-glasses [114]. Intermediate band width manganites based on calcium, especially, the charge ordered composition, $La_{0.5}Ca_{0.5}MnO_3$, is interesting not only from a fundamental angle but also from an applied perspective as they are likely to exhibit colossal thermoelectric power as observed in $Gd_{0.5}Sr_{0.5}MnO_3$. Moreover, it is presumed that these materials also could be another system to check the veracity of this mechanism proposed in the case of $Gd_{0.5}Sr_{0.5}MnO_3$. This is an objective of the present investigation.

Most of the existing reports in literature deals with the structural, electrical and magnetic properties of manganites based on lighter rare earth elements having larger ionic radii and of weak magnetic nature. However there are very few literature reports dealing with heavy rare earth elements (Eu, Gd, Tb, Dy) based manganites [115-117]. Since heavy rare earth elements exhibit largest magnetic moments of all the series a diverse magnetic response of the overall manganite system is expected by incorporating them instead of lighter ones. Troyanchuk *et.al* reported that compounds with smaller ionic radii such as Sm, Eu and Gd exhibit properties of spin glass [118]. Large difference in the ionic radii of RE and AE ions results in the Mn-O-Mn bond angle variation which in turn leads to spin glass state [119].The average radius of A site cation ($<r_A>$) regime of 1.20±0.02 Å in $RE_{0.5}AE_{0.5}MnO_3$, exhibiting complex phenomena and properties, including re-entrant transitions, deserves greater attention. Average A site ionic radii ($<r_A>$) of $Gd_{1-x}Sr_xMnO_3$ fall in this regime.

The role of grain boundary and grain size on the thermoelectric properties of manganites is less studied. Since the contribution to thermoelectric power from different scattering phenomena such as magnon drag, phonon drag, charge ordering and spin glass strongly depends on grain size, it is imperative to study the grain size dependant transport properties in charge ordered $Gd_{1-x}Sr_xMnO_3$ (x =0.3, 0.5 and 0.6) samples. Garcia Landa *et. al* observed the coexistence of charge ordered insulator (COI) and cluster glass (CG) states for this compound to occur below 42 K [120]. Though the thermoelectric power is appreciable, it was observed at low temperatures. From an application point of view, the magnetic transition temperature where the thermoelectric power peak coincides has to be enhanced. Also these manganites are found to be exhibiting magnetic reversal. Magnetic reversal is found to be an important phenomenon in magnetism and is

utilized in magnetic data storage processes. To fabricate a rich variety of electronic and magnetic devices, thin film form of $Gd_{1-x}Sr_xMnO_3$ (x =0.3, 0.5 and 0.6) with unique physical properties is necessary. A systematic study of both the spin reversal and spin glass existence in the charge ordered region of both bulk and thin film form of $Gd_{1-x}Sr_xMnO_3$ assume significance. So it is in this context that a thorough investigation on thin film forms of $Gd_{1-x}Sr_xMnO_3$ is relevant. This is a virgin area and rich Physics can be derived out of these investigations. This is one of the motivations of the present work.

Phenomena like the co-existences of ferromagnetic and antiferromagnetic phases and of charge ordering (CO) in $La_{0.5}Ca_{0.5}MnO_3$ and $Gd_{1-x}Sr_xMnO_3$ (x =0.3, 0.5 and 0.6) is also an interesting aspect and worth investigating. It will be our endeavour to apply suitable models for theoretical fitting of colossal thermoelectric power to propose a plausible mechanism for explaining the phenomenon of colossal thermoelectric power. This is yet another motivation of the present study.

Several groups had explained the giant TEP peak value observed at low temperatures and related it to the existence of spin-glass [121-123]. Fischer calculated the thermoelectric power of spin-glasses on the basis of spin interactions by means of time dependent perturbation theory [124]. Mandal explained the thermoelectric power in the ferromagnetic phase of $La_{1-x}Ca_xMnO_3$ on the basis of electron-magnon scattering [125]. It will be our endeavour to apply these models to explain the colossal thermoelectric power of $La_{0.5}Ca_{0.5}MnO_3$ and $Gd_{1-x}Sr_xMnO_3$ (x =0.3, 0.5 and 0.6) by dividing the entire temperature regime into three regions and to propose a plausible mechanism for explaining the phenomenon of colossal thermoelectric power.

Charge ordering is generally not found in large bandwidth manganites. $La_{0.5}Sr_{0.5}MnO_3$, a prototypical double exchange ferromagnet is a representative of large bandwidth manganites. It was subjected to extensive investigations, especially, on the thermoelectric properties. This study is intended to provide a comparison vis a vis large, small and intermediate bandwidth manganites. Curie temperature of LSMO with 50% substitution of Lanthanum by Strontium is substantially large. Hence conduction mechanism in the paramagnetic and ferromagnetic region of $La_{0.5}Sr_{0.5}MnO_3$ manganites is significant.

Besides the hole doped manganites, Substitution of Ytterbium in $CaMnO_3$ will yield, $Ca_{0.9}Yb_{0.1}MnO_3$. This composition is envisaged to be a candidate material displaying appreciable thermoelectric power at near room temperatures and above. Preliminary investigation on this compound on all the performance characteristics of a thermoelectric material is yet another objective of the present investigation

1.11 Objectives

- Synthesis of charge ordered small bandwidth manganites belonging to the series $Gd_{1-x}Sr_xMnO_3$ (x =0.3, 0.5 and 0.6) by wet solid state reaction method with varying sizes.
- Evaluation of size effect on the thermoelectric power in charge ordered small bandwidth manganites based on Gd-Sr.
- Deposition of thin films of $Gd_{1-x}Sr_xMnO_3$ using Pulsed Laser Deposition on silicon substrate.
- Study the phenomenon of the existence of spin reversal and spin glass in the charge ordered regions of both bulk and thin film form of $Gd_{1-x}Sr_xMnO_3$ through magnetic measurements.

- Synthesis of charge ordered intermediate bandwidth manganite, $La_{0.5}Ca_{0.5}MnO_3$, by mechanical milling.
- Evaluation of thermoelectric power of $La_{0.5}Ca_{0.5}MnO_3$.
- Study co-existence of spin glass and charge ordering through magnetic studies.
- Modelling of colossal thermoelectric power observed in the small and intermediate bandwidth manganites.
- Synthesis of $La_{0.5}Sr_{0.5}MnO_3$ by citrate gel method and evaluation of its thermoelectric power.
- Correlation of results.

References

[1] D. M. Rowe, (ed.) CRC Handbook of thermoelectrics (CRC, Boca Raton, 1995).

[2] T. J. Seebeck, "Magnetic polarization of metals and minerals by temperature differences", Treatises of the Royal Academy of Sciences in Berlin 265 (1822).

[3] J.C. Peltier "New experiments on the heat effects of electric currents", Ann.Chimie et de Physique, **56** , 371 (1834).

[4] G. J. Snyder and E. S. Toberer, Nat.Mater.**7**, 105 (2008).

[5] M. Cutler, J. F. Leavy and R. L. Fitzpatrick, Phys. Rev. **133,** A1143 (1964).

[6] K. Koumoto, I. Terasaki, and R. Funahashi, Mater. Res. Soc. Bull. **31**, 206 (2006).

[7] G. J. Snyder, T. Caillat, and J. P. Fleurial, Phys. Rev. B **62,** 10185 (2000).

[8] G. D. Mahan, and J. O. Sofo, Proc. Natl. Acad. Sci. USA, **93**, 7436 (1996).

[9] G. A. Slack, (ed.) Solid State Physics (Academic Press, New York, 1979).

[10] C. Dames and G. Chen, in Thermoelectrics Handbook Macro to Nano (ed. D. M.Rowe) Ch. 42 (CRC, Boca Raton) (2006).

[11] G. A. Slack in CRC Handbook of &thermoelectrics (ed. Rowe, M.) 407–440 (CRC, Boca Raton, (1995).

[12] C. Wood, Rep. Prog. Phys., **51**, 459 (1988).

[13] J. Zheng, Front. Phys. China.**3**, 269 (2008).

[14] J-F. Li, W-S.Liu, L-D. Zhao and M. Zhou, NPG Asia Mater. **2(4)**, 152 (2010).

[15] L. E. Bell, Science **321**, 1457 (2008).

[16] http://www.mpoweruk.com/thermoelectricity.htm.

[17] H. J. Goldsmid and G. S. Nolas, 20th International Conference on Thermoelectrics (2001).

[18] C. Sales, D. Mandrus, R. K. Williams, Science **272**, 1325 (1996).

[19] G. S. Nolas, D. T. Morelli, T. M. Tritt, Annu. Rev. Mater. Sci. **29**, 89 (1999).

[20] G. S. Nolas, J. L. Cohn, G. A. Slack, S. B. Schujman, Appl. Phys. Lett. **73**, 178 (1998).

[21] J. L. Cohn, G. S. Nolas, V. Fessatidis, T. H. Metcalf and G. A. Slack, Phys. Rev. Lett. **82**, 779 (1999).

[22] F. Meng, N. V. Chandra Shekar, J. V. Badding, and G.S. Nolas, J. Appl. Phys. **89**, 1730 (2001).

[23] A. M. Guloy, R. Ramlau, Z. Tang, W. Schnelle, M. Baitinger, and Y. Grin, Nature, **443**, 320 (2006).

[24] L. D. Hicks, M. S. Dresselhaus, Phys. Rev. B **47**, 12727 (1993).

[25] J. Hejtmanek, M. Veverka, K. Knizek, H. Fujishiro, S. Hebert, Y. Klein, A. Maignan, C. Bellouard, and B. Lenoir, Mater. Res. Soc. Symp. Proc. **886**, 0886-F01-07.1(2006).

[26] P. Oleynikov, J. Hanson, J. C. Zheng, L. Wu, V.Volkov, Q. Jie, Q. Li, and Y. Zhu, Electron Microscopy Study of Layered Thermoelectric Cobalt Oxide $[Ca_2CoO_3]_{0.6}2CoO_2$, Workshop of "Electronic Structure and Functionality of Thermoelectric Materials", Reykjavik,Iceland, Jul. 30–Aug. 1, (2007).

[27] L. D. Hicks and M. S. Dresselhaus, Phys. Rev. **47**, 16631 (1993).

[28] R. Venkatasubramanian, E. Siivola, T. Colpitts, B. O'Quinn, Nature **413**, 597 (2001).

[29] T. C. Harman, P. J. Taylor, M. P. Walsh, B. E. LaForge, Science **297**, 2229 (2002).

[30] J. P. Heremans, V. Jovovic, E. S. Toberer, A. Saramat, K. Kurosaki, A. Charoenphakdee, S. Yamanaka and G. J. Snyder, Science **321**, 554 (2008).

[31] W.-S. Liu, L.-D. Zhao, B.-P. Zhang, H.-L. Zhang, J.-F. Li, Appl. Phys. Lett. **93**, 042109 (2008).

[32] K. F. Hsu, S. Loo, F. Guo, W. Chen, J. S. Dyck, C. Uher,T. Hogan, E. K. Polychroniadis and M. G. Kanatzidis, Science, **303**, 816 (2004).

[33] A. I. Hochbaum, R. Chen, R. D. Delgado, W. Liang, E. C.Garnett, M. Najarian, A. Majumdar, and P. Yang, Nature, **451**, 163 (2008).

[34] A. I. Boukai, Nature, **451**, 168 (2008).

[35] Gabriel Kotliar and Dieter Vollhardt, Physics Today, 53-59, (2004).

[36] E. Dagotto, Science, **309**, 257 (2005).

[37] Y. Tokura, Rep. Prog. Phys. **69**, 797 (2006).

[38] A-M Haghiri-Gosnet and J-P Renard, J. Phys. D: Appl. Phys. **36**, R127 (2003).

[39] A. Asamitsu, Y. Moritomo and Y. Tokura, Phys.Rev.B **53**, R2952 (1996).

[40] E. O. Wollan and W. C. Koehler, Phys.Rev.B **100**, 545 (1955).

[41] S. Jin, T. H. Tiefel, M. McCormack, R. A. Fastnach, R. Ramesh, and L. H. Chen, Science **264**, 413 (1994).

[42] Tapati Sarkar, A. K. Raychaudhuri, A. K. Bera and S. M. Yusuf New J. Phys. **12**, 123026 (2010).

[43] A. M. Shuvaev, A. A. Mukhin and A. Pimenov, J. Phys. Condens. Matter **23**, 113201 (2011).

[44] M-H. Phan, S.C. Yu, J. Magn. Magn. Mater. **308**, 325 (2007).

[45] P. Raychaudhuri, T. K. Nath, P. Sinha, C. Mitra, A. K. Nigam, S.K. Dhar and R. Pinto, J. Phys.: Condens. Matter, **9**, 10919 (1997).

[46] L. M. Wang, Jian-Hong Lai, Jyh-Iuan Wu, Y.-K. Kuo, C. L. Chang, J. Appl. Phys. **102**, 023915 (2007).

[47] C. N. R. Rao, A. K. Kundu, M. M. Seikh, and L. Sudheendra, Dalton Transactions 3003 (2004).

[48] M. Imada, A. Fujimori, and Y. Tokura, Rev. Mod. Phys.**70**, 1039 (1998).

[49] J. C. Loudan, N. D. Mathur, and P. A. Midgley, Nature **420**, 797 (2002).

[50] G. H. Jonker and J. H. Van Santen, Physica **16** 337 (1950).

[51] J. H. Van Santen and G. H. Jonker *P*hysica **16** 599 (1950).

[52] G. H. Jonker, Physica **20**, 1118 (1954).

[53] P. W. Anderson and H. Hasegawa, Phys.Rev.**100**, 675, (1955).

[54] J. B. Goodenough, Phys.Rev.B **100**, 564 (1955).

[55] C. Zener Phys. Rev. **81**, 440 (1951).

[56] de Gennes P G Phys. Rev. **118** 141 (1960).

[57] J. Volger, Physica (Amsterdam) **20**, 49 (1954).

[58] J. Tanaka, M. Umehara, S. Tamura, M. Tsukioka, and S.Ehara, J. Phys. Soc. Jpn. **51**, 1236 (1982).

[59] T. Kasuya, and A. Yanase, Rev. Mod. Phys. **40**, 684 (1968).

[60] N. Mott and E. Davis, Electronic Processes in Non-Crystalline Materials, Clarendon Press, Oxford (1971).

[61] R.Von Helmolt, J. Wecker, B. Holzapfel, L.Schultz , K. Samwer, Phys. Rev. Lett. **71**, 2331-2333, (1993).

[62] Y. Tokura, Colossal Magneto-resistive oxides, Gordon and Breach Science Publishers, New York (2000).

[63] J. M. D. Coey and M. Viret, Advances in Physics **48**, 167 (1999).

[64] A. P. Ramirez, J. Phys. Condens. Matter, **9**, 8171-8199 (1997).

[65] P. K. Siwach, H. K. Singh, O. N. Srivastava, J. Phys. Condens. Matter **20**, 273201 (2008).

[66] C. N. R. Rao, B. Raveau, (Eds.) "Colossal Magnetoresistance, Charge-ordering and Related Aspects of Manganese Oxides", World Scientific, 1998, Reprinted, (2005).

[67] S. M. Yusuf, K. R. Chakraborty, S. K. Paranjpe, R. Ganguly, P. K. Mishra, J. V. Yakhmi, and V. C. Sahni, PhysRevB.**68**, 104421 (2003).

[68] N. A. Spaldin, Magnetic Materials: Fundamentals and Applications, 2nd ed., Cambridge University Press, New York (2011).

[69] Jeremy K. Burdett, Chemical Bonds: A Dialog, John Wiley & sons, England (1997).

[70] C. Zener, Phys. Rev. **82**, 403 (1951).

[71] H. A. Kramers, Physica **1**, 182 (1934).

[72] A. Millis, B. Shraiman, and P. Littlewood, Phys. Rev. Lett. **74**, 5144 (1995).

[73] A. J. Millis, B. I. Shraiman, R. Mueller, Phys. Rev. Lett. **77**, 175 (1996).

[74] A. J. Millis Nature, **392**, 147 (1998).

[75] K. Kubo, N. Ohata J. Phys. Soc. Jpn., **33**, 21 (1972).

[76] J. A. Mydosh, Spin glasses: an experimental introduction Taylor & Francis (1993).

[77] T. Elovaara, H. Huhtinen, S. Majumdar and P. Paturi, J. Phys. Condens. Matter **24**, 216002 (2012).

[78] M. N. Baibich, J. M. Broto, A. Fert, F. N. V Dau, F. Petroff, P. Etienne, G. Creuzct, A. Friedrich and J. Chazelas, Phys. Rev. Lett. **61**, 2472 (1988).

[79] G. Binasch, P. Gr¨unberg, F. Saurenbach, and W. Zinn. Phys.Rev. B, **39**, 4828 (1989).

[80] E. Dagotto, 'Nanoscale Phase Separation and Colossal Magnetoresistance', Springer, Germany (2003).

[81] T. Saitoh, A. Sekiyama, K. Kobayashi, T. Mizokawa, A. Fujimori, D. D. Sarma, Y. Takeda and M. Takano Phys. Rev. B **56**, 8836 (1997).

[82] E. Dagotto, T. Hotta and A. Moreo, Phys. Rep. **344**, 1 (2001).

[83] F. Duan and J. Guojun , Introduction to Condensed Matter Physics (Singapore: World Scientific) (2005).

[84] V. Goldschmidt Naturwissenschaften **14** 477 (1926).

[85] Z. Jirak, S. Krupicka , Z. Simsa , M. Dlouha and S. Vratislav, J. Magn.Magn.Mater. **53**,153 (1985).

[86] C. N. R. Rao, Anthony Arulraj, A. K. Cheetham and Bernard Raveau, J. Phys. Condens. Matter **12**, R83–R106 (2000).

[87] J. Kanamori, J. Phys. Chem. Solids, **10**, 87 (1959).

[88] Y. Tokura, N. Nagaosa, Science, **288**, 462 (2000).

[89] J.Orenstein, A. J.Millis, Science **288**, 468-474 (2000).

[90] Y. Tokura, Y. Tomioka J. Mag. Mag. Mat. **200**, 1 (1999).

[91] H. Kuwahara, Y. Tomioka, A. Asamitsu, Y. Morimoto and Y. Tokura, Science **270**, 961 (1995).

[92] Y. Tokura, Y. Tomioka, H. Kuwahara, A. Asamitsu, Y. Morimoto and M. Kasai, J. Appl. Phys. **79** 5288 (1996).

[93] P. Schiffer , A. P. Ramirez, A. W. P. Bao and S.W. Cheong, Phys. Rev. Lett. **75**,3336 (1995).

[94] Giri, Poddar, and Nath AIP Advances **1**, 032110 (2011).

[95] B. Hong , "Charge Order, Orbit Order, Spin Order of Perovskite Manganites and Their Interaction" [Dissertation], University of Science and Technology of China, Hefei, (2007).

[96] P. Zhensheng, Y. Gang, W. Guiying, T. Yonggang, G. Huanyin and M.Qiang, Rare Metals **30**, 241 (2011).

[97] N. Furukawa J. Phys.Soc. Japan, **64**, 3164-3167 (1995).

[98] P. G. Radaelli, D. E. Cox, M. Marezio and S-W.Cheong, Phys. Rev. B **55,** 3015 (1997).

[99] A. Urushibara, Y. Moritomo, T. Arima, A. Asamitsu, J. Kido, and Y. Tokura, Phys. Rev. B **51**,14103 (1995).

[100] H. Fujishiro, M. Ikebe, and Y. Konno, J. Phys. Soc. Jpn. **67**, 1799 (1998).

[101] Y. Moritomo, T. Akimoto, A. Nakamura, K. Ohoyama, and M. Ohashi, Phys. Rev. B **58**, 5544 (1998).

[102] A.Ramirez, P.Schiffer, S.-W. Cheong, C. Chen, W. Bao, T. Palstra, P. Gammel, D. Bishop, and B. Zegarski, Phys. Rev. Lett. **76**, 3188 (1996).

[103] P. Pichanusakorn, P. Bandaru, Mater. Sci. Eng. **R 67**, 19 (2010).

[104]K. Koumoto, Y. Wang, R. Zhang, A. Kosuga and R. Funahashi, Annu.Rev. Mater. Res.**40**, 363 (2010).

[105] Y. Lan, A. Jerome Minnich, G.Chen, and Z. Ren, Adv. Funct. Mater. **20**, 357 (2010).

[106] T. M. Tritt and M.A. Subramanian, MRS Bull. **31**,188 (2006).

[107] N. B. Duarte, G.D. Mahan and S. Tadigadapa, NanoLett. **9**, 617 (2009).

[108] G. Mahan, B. Sales and J. Sharp, Phys.Today **50**, 42 (1997).

[109] A. Bentien, S. Johnsen, G.K.H. Madsen, B. B. Iversen and F. Steglich, Europhys. Lett. **80**, 17008 (2007).

[110] B. C. Cong, T. Tsuji, P. X. Thao, P. Q. Thanh, and Y. Yamamura, Physica B **352**, 18 (2004).

[111] Y. Tokura Fundamental features of colossal magnetoresistive manganese oxides. In: Tokura, Y. (Ed.), Contribution to Colossal Magnetoresistance Oxides, Monographs in Condensed Matter Science. Gordon & Breach, London (1999).

[112] O.Pena, M.Bahout, K.Ghanimi, P.Duran, D.Gutierrez and C. Moure, J. Mater. Chem. **12**, 2480 (2002).

[113] M. Svedberg, S. Majumdar, H. Huhtinen, P. Paturi and S. Granroth, J. Phys. Condens. Matter **23**, 386005 (2011).

[114] S. Sagar, V. Ganesan, P. A. Joy, S. Thomas, A. Liebig, M. Albrecht and M. R. Anantharaman, Europhys. Lett. **91**, 17008 (2010).

[115] G. Jeffrey Snyder, C. H. Booth, F. Bridges, Ron Hiskes, Steve DiCarolis, M. R. Beasley and T. H. Geballe, Phys. Rev. B **55**, 6453 (1997).

[116] T. Kimura, T. Goto, H. Shintani, K. Ishizaka, T. Arima and Y. Tokura, Nature **426**, 55 (2003).

[117] W. Eerenstein, N. D. Mathur and J. F. Scott, Nature **442**, 759 (2006).

[118] I.O. Troyanchuk, S.V. Trukhanov, and H. Szymczak, Crystallography Reports, **47**, 652 (2002).

[119] S.V. Trukhanov, I.O. Troyanchuk, M. Hervieu, H. Szymczak, K. Bärner Phys. Rev. B **66**, 184424 (2002).

[120] B. Garcia-Landa, J. M. De Teresa, M.R. Ibarra, C. Ritter, R. Drost and M.R. Lees, J. Appl. Phys. **83**, 7664 (1998).

[121] D.Huo, J. Sakurai, T.Kuwai, Y.Isikawa, Q. Lu, Phys. Rev. B **64**, 224405 (2001).

[122] D. K. C. MacDonald, W. B. Pearson, I.M Templeton, Proc.R.Soc. London Ser.A **266**, 161 (1962).

[123] A. Kjekshus, W.B. Pearson, Can. J. Phys. **40**, 98 (1962).

[124] K.H. Fischer, Z. Phys. B Con. Mat.**42**, 245 (1981).

[125] P. Mandal, Phys. Rev. B **61**, 14675 (2000).

Chapter 2

Experimental techniques

This chapter takes a look at major experimental techniques employed in the characterization of bulk and thin film samples. A description about both High Energy Ball Milling unit and the thin film deposition technique by pulsed laser deposition is provided in the beginning of this chapter. Analysis of samples are carried out using state of the art tools such as X-ray Diffraction (XRD), Transmission Electron Microscope (TEM), Scanning Electron Microscope (SEM), Atomic Force Microscopy (AFM), X-Ray Photoelectron Spectroscopy (XPS), Rutherford Backscattering Spectrometry (RBS), Thermoelectric power measuring set up, Magnetoresistance measurement set up, Vibrating Sample Magnetometer (VSM) and Superconducting Quantum Interference Device Magnetometer (SQUID Magnetometer). This chapter also discusses the details of Zero Field Cooled-Field Cooled magnetisation measurements.

Experimental techniques are an important component in any investigation conducted in the realm of experimental Solid state Physics. Both preparative techniques as well as analytical techniques are equally important. A good understanding of the techniques is highly essential for the right interpretation of the results. Emphasis is laid in synthesizing samples rather than outsourcing because it is believed that proper interpretations are directly linked to the sample history. Hence this chapter discusses the preparative techniques and working principle of major experimental techniques employed for characterization of both bulk as well as thin film samples. A detailed description of the sample preparation is provided in other chapters.

2.1 High Energy Ball Milling Unit (HEBM)

High Energy Ball Milling unit is employed to produce varying sizes of particles. HEBM was developed in 1970's as an industrial process to synthesize new alloys and phase mixtures. This is a top-down technique widely employed in the preparation of nanomaterials for reducing the grain size of particles.

In the present work a planetary type ball- milling unit device, 'Fritsch pulverisette 7 planetary micro mill' is used. Photograph of the high energy ball milling unit used is shown in figure (2.1). In this ball milling unit, the grinding bowls (vials) rotate on their own axis while simultaneously rotating through an arc around the central axis. The grinding balls and the material in the grinding vial are thus acted upon by the centrifugal forces, which constantly change in direction and intensity resulting in efficient, fast grinding process. The grinding bowl and the supporting disc rotate in opposite directions, so that the centrifugal forces alternatively act in the same and opposite directions. This cause frictional effect between the balls and vial and impact effect due to the balls impacting against the opposite wall of

the vial. This results in excellent grinding performance with considerably shorter grinding times. Atmospheric contamination can be minimized by sealing the vial with a flexible 'O' ring after the powder has been loaded. If a milling medium-a fluid (usually an organic fluid, in the present work acetone) is used, contamination by the milling tools can be prevented and also it minimizes the wear.

Figure 2.1 Fritsch planetary micro mill, 'pulverisette 7' high energy ball millimg unit.

The reduction in grain size is accomplished by the kinetic energy transfer from balls to powder. Since the kinetic energy of the balls is a function of their mass and velocity, dense materials like steel or tungsten carbide are preferred. The hardness of the grinding vial and grinding balls must be higher than that of the materials used for grinding. Usually vial and balls of the same material will be chosen.

In this work, tungsten carbide vials and balls (with density~14.75 g/cm^3) are used. In the initial stage of milling, a fast decrease of grain size occurs which slows down after extended milling [1, 2].

2.2 Thin film deposition

2.2.1 Pulsed Laser Deposition (PLD)

Pulsed laser deposition is a thin film deposition technique for obtaining high quality thin film of materials. In this technique a high power

pulsed laser beam is focused to strike a target of desired composition placed inside a vacuum chamber. Material is then vaporized from the target and deposited as a thin film on a substrate. This process can occur in ultra-high vacuum or in the presence of a background gas, such as oxygen. Oxygen gas is commonly used when depositing oxides to fully oxygenate the deposited films. PLD is applicable to almost any material especially to compounds that are difficult to produce in thin film form by other techniques. By PLD technique one can retain exactly the same stoichiometry as the target material in thin film forms. Although laser assisted film growth started years back in 1960's, origin of PLD technique was in 1987 when Xindi Wu, Dirk Dijkkamp and T Venkatesan successfully laser deposited a superconducting film of $YBa_2Cu_3O_7$. Since then, laser deposition has been widely accepted for thin film preparation. In a PLD system, the target material is locally heated to the melting point, melted and vaporized in vacuum. The laser pulses may also provide photo emitted electrons from the target surface to make a plasma plume which is termed as laser ablation. This ablation produces a transient, highly luminous plasma state called plume, which spans the region between target and the substrate. Plasma plume (vaporized material containing ions, electrons etc.) traverses to the substrate placed in the other end of the chamber, gets deposited and thus thin film growth takes place [3,4]. The evaporation process may be complex as it includes both the thermal process and plasma process.

The schematic diagram of a PLD system is shown in figure (2.2). It consists of a large chamber with a rotating target holder (or a carousel) and substrate holder. A heater is attached to the substrate holder to heat the substrate if necessary. A laser beam is allowed to incident on the target through a SiO_2 window and produces plasma plume between target and substrate. Plume of target material ions hits the surface of substrate and such

sputtered species from the substrate and the target material are the source for condensation of particles. When the condensation rate is high, a thermal equilibrium is reached enabling the growth of film on the surface of the substrate [4,5].

As the deposition conditions depends on several factors like laser fluence, substrate temperature, target to substrate distance and chamber pressure, the laser deposition process is not so simple. In most cases, background gases like nitrogen or oxygen are also used for deposition and the background gas pressure too determines thin film characteristics. Optimization of the deposition parameters is one of the main part of PLD technique. PLD deposition process thus goes through four major crucial steps [6,7]:

- Laser ablation of target and plasma plume formation
- Dynamic or movement of plasma plume guided by coulomb repulsion and recoil from the target surface
- Deposition of the ablated material on the substrate
- Nucleation and growth of thin film on the surface of substrate

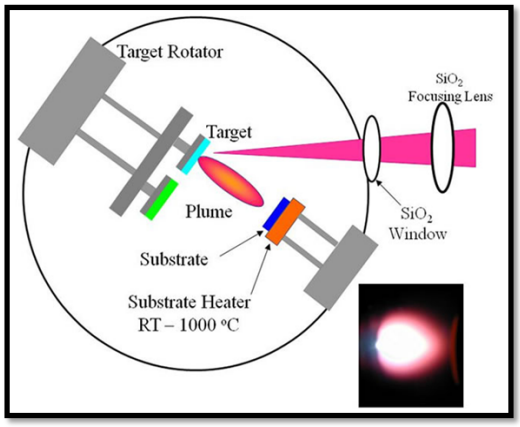

Figure 2.2: Schematic diagram of PLD.

PLD has significant advantages over other thin film deposition techniques. 1) stoichiometry of the target can be retained in the deposited films. 2) higher deposition rates at moderate laser fluences and the control of film thickness by means of number of laser pulses 3) laser as an external source cleans the process without any filaments and the deposition can occur in reactive and inert gases 4) using a carousel for placing more than one target enables multilayer deposition without breaking vacuum for the next deposition. In spite of the said advantages of PLD, there are some setbacks for this deposition technique such as 1) smaller area of deposition (~ 1cm^2) makes it unsuitable for industrial usage 2) possibility of having macroscopic globules of ablated material over the substrate surface 3) fundamentals of plasma plume are not understood fully and therefore deposition of novel materials require extensive optimization. Recently modifications have been introduced into PLD systems to obtain high quality films. Raster scan of laser pulses over the target surface and movement of the substrate during deposition results in obtaining thin films with uniform thickness and composition. Mechanical velocity filter and techniques like collision of plasma plumes and off axis deposition removes the material particles from the film surface. Thus pulsed laser deposition offers excellent quality stoichiometric films with a good control over the thickness of deposition [4-8].

2.3 Analysis tools and techniques

2.3.1. X-Ray Diffraction (XRD)

X -Ray Diffraction (XRD) is the most widely used analytical technique that has long been used to address all issues related to the crystal structure of solids which include lattice constants and geometry, orientation, identification of unknown materials, defects and stresses Each crystalline solid has its unique characteristic X-ray powder diffraction pattern which

may be used as a "fingerprint" for its identification. X-ray powder diffraction (XRD) is primarily used for phase identification of a crystalline material and can provide information on unit cell dimensions. It is now a common technique for the study of crystal structures and atomic spacing. The particular advantage of X-ray diffraction analysis is that it discloses the presence of a material without individually identifying each atom.

X-rays are high energy electromagnetic radiation having energies ranging from about 200 eV to 1 MeV and wavelength close to 1 Å [9]. An X-ray diffractometer consists of mainly three basic components, namely, X-Ray source, specimen or sample stage and X-ray detector as shown in figure (2.3). Sample to be analysed is spread on a flat non diffracting glass slide and is exposed to the X-ray beam. If an element in the sample has an atomic number slightly below that of the target metal, the X-rays will be strongly absorbed leading to decrease in intensity of the diffracted beam. The most commonly used target material for X-ray diffraction is Cu. The XRD patterns of the samples were recorded on the X-ray diffractometer (Rigaku Dmax-C) using Cu K_α radiation (λ=1.5418 Å), which has an energy of 8.04 keV [9, 10].

X-rays generated by a cathode ray tube, are filtered to produce monochromatic radiation, collimated to concentrate, and directed toward the sample. The interaction of the incident rays with the sample produces constructive interference (and a diffracted ray) when conditions satisfy Bragg's Law. When a collimated beam of X-ray with a wavelength of 1.5406Å is incident on a specimen it is diffracted by the crystalline planes in the specimen according to the Bragg's law as given by equation 2.1. W.H. Bragg and his son Sir W.L. Bragg developed this equation connecting crystalline planes and diffraction angle in 1913 [10, 11].

$$n\lambda = 2dSin\theta \qquad (2.1)$$

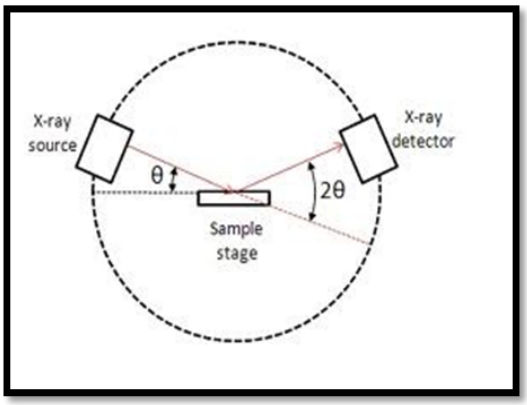

Figure 2.3 Schematic diagram of X-ray diffractometer

Where λ is the wavelength of the X-radiation, *n* is an integer, *d* is the spacing between atomic planes in the crystalline planes and θ is known as diffraction angle. This law relates the wavelength of electromagnetic radiation to the diffraction angle and the lattice spacing in a crystalline sample. The intensity of diffracted X-rays was measured and plotted as a function of diffraction angle 2θ. From the 2θ values of the peaks, the lattice spacing (d) can be calculated. Experimentally obtained diffraction patterns of the sample are compared with the standard powder diffraction files published by the International Centre for Diffraction Data (ICDD).

The directions of possible diffractions depend on the size and shape of the unit cell of the material. Lattice parameter 'a' can be calculated assuming cubic symmetry by employing the Bragg relation. The intensities of the diffracted waves depend on the kind and arrangement of atoms in the crystal structure. The simplest and extensively used method for estimating the crystallite size is by Debye Scherrer formula:

$$D = \frac{0.9\lambda}{\beta Cos\theta} \qquad (2.2)$$

where *D* is the crystallite size, β is the angular width (in radians) which is equal to the full width at half maximum (FWHM).

2.3.2. Rietveld Refinement

Rietveld refinement is a technique used for performing fine structure refinement using X-ray diffraction or neutron diffraction in characterizing the crystalline samples. It utilizes the diffraction data of peak reflections vs angle values in evaluating various material characteristics like lattice parameters and space group. Rietveld method was first devised by Hugo rietveld and uses a least squares approach to refine a theoretical line profile to match with measured profile. The method was first reported for the diffraction of monochromatic neutrons with reflection-position expressed in terms of Bragg angle 2θ. Same terminology is widely used for refinement although alternative scales such as X-ray energy or neutron time-of-flight are also in practice. Refinement parameters like fundamental lattice vectors, angle between them, positions and occupancy of ions are varied and the theoretical profile is made to match with the measured profile. Thus the principle of rietveld refinement involves minimizing a function M which is the difference between a calculated profile y (calc) and the observed data y(obs) [12].

$$M = \sum_i w_i \{ y_i^{obs} - \frac{1}{c} y_i^{calc} \}^2 \qquad (2.3)$$

where w_i is the statistical weight and c is the scaling factor such that $y^{calc} = c\, y^{obs}$. The introduction of this technique is a significant step forward in the diffraction analysis of powder samples as it relies on strongly overlapping reflections and gives accurate values of lattice parameters [13].

2.3.3 Transmission Electron Microscopy (TEM)

The transmission electron microscopy is a very powerful technique in material science to determine the size and shape of the nanostructured materials as well as to obtain structural information. An electron microscope uses an electron beam to produce the image of the object and magnification

is obtained by electromagnetic fields; unlike light or optical microscopes, in which light waves are used to produce the image and magnification is obtained by a system of optical lenses. Geometry of transmission electron microscope is shown in figure (2.4).

The electron source consists of a cathode and an anode. The cathode is a tungsten filament which emits electrons when being heated. The beam is then accelerated towards the specimen by the positive anode. The electron source works like a cathode ray tube. This electron beam is tightly focused using electromagnetic lens and metal apertures. The system only allows electrons within a small energy range to pass through, so the electrons in the electron beam will have a well-defined energy. The beam goes to imaging system through the specimen. The imaging system consists of another electromagnetic lens system and a screen. This electromagnetic lens system contains two lens, one for refocusing the electrons after they pass through the specimen, and the other for enlarging the image and projecting it onto the screen. The screen has a phosphorescent plate which glows when being hit by electrons.

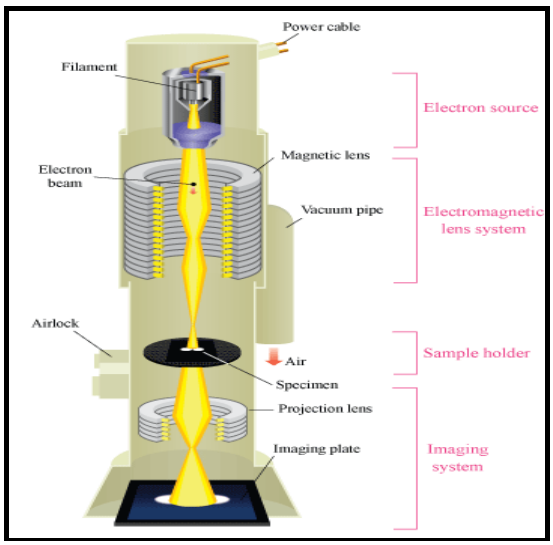

Figure 2.4: Schematic of Transmission Electron Microscope

Operation

The operation of TEM requires an ultra-high vacuum and a high voltage. In TEM, there are two methods for specimen observation, diffraction mode and image mode. In diffraction mode, an electron diffraction pattern is obtained on the fluorescent screen, originating from the sample area illuminated by the electron beam. The diffraction pattern is entirely equivalent to an X-ray diffraction pattern: a single crystal will produce a spot pattern on the screen, a polycrystal will produce a powder or ring pattern (assuming that the illuminated area includes a sufficient quantity of crystallites), and a glassy or amorphous material will produce a series of diffuse halos. The image mode produces an image of the illuminated sample area. The image can contain contrast brought about by several mechanisms: mass contrast, due to spatial separations between distinct atomic constituents; thickness contrast, due to non-uniformity in sample thickness; diffraction contrast, which in the case of crystalline materials results from scattering of the incident electron wave by structural defects; and phase contrast. If the unscattered beam is selected for image formation, one obtains the Bright Field Image. Dark Field Images are obtained if diffracted beams are selected by the objective aperture. Also in TEM, analysis can be done with EDS (Energy Dispersive X-ray spectroscopy), EELS (Electron Energy Loss Spectrum) and EFTEM (Energy Filtered Transmission Electron Microscopy) data [14, 15].

2.3.4. Scanning Electron Microscope (SEM)

The Scanning Electron Microscope (SEM) is an electron microscope which utilizes electrons similar to optical microscope which utilizes visible light. SEM uses a focussed beam of high energy electrons to generate a variety of signals at the surface of solid specimens. The signal that derive from electron sample interactions reveal information about the external

morphology, chemical composition, crystal structure and other properties such as electrical conductivity of the sample [15 - 16]. There are many advantages for using the SEM instead of a light detector. The SEM has a large depth of field, which allows more of a specimen to be in focus at one time. The SEM also has much higher resolution, so closely spaced specimens can be magnified at much higher levels.

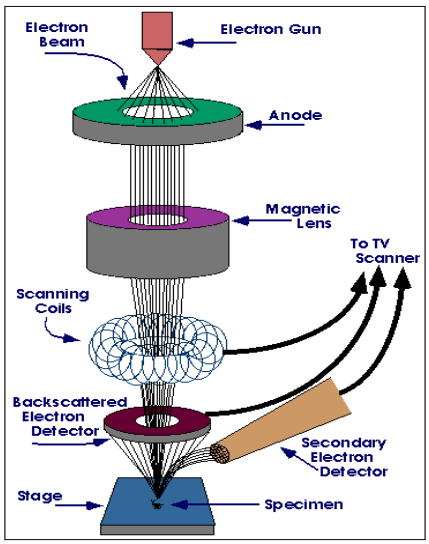

Figure 2.5: Schematic of SEM

Schematic of SEM is shown in figure (2.5). An electron gun produces electrons of high energy which is accelerated by an anode. The beam is defocused by a series of magnetic lenses. Each lens has an associated defining aperture that limits the divergence of the electron beam. The top lenses are called condenser lenses, and are often operated as if they were a single lens. When the current through the condenser lens increases, the focal length decreases and the divergence increases. The lens therefore passes less beam current on to the next lens in the chain. The beam next arrives at the final lens-aperture combination. The final lens does the ultimate focusing of the beam onto the surface of the sample. The sample is attached to a specimen stage that provides x and y motion, as well as tilt with

respect to the beam axis and rotation about an axis normal to the specimen's surface**.** The two dimensional map of the signal yields a SEM image [18]. The main applications of SEM are in surface topography and elemental mapping.

2.3.5. Atomic Force Microscopy (AFM)

Scanning probe microscopes (SPM) are usually designed to measure properties like height, magnetism, friction with a probe. Atomic Force Microscopy (AFM) is one kind of SPM which maps surface property on an atomic or nanometre scale. AFM was invented by Binning, Quate, and Gerber in 1986. AFM senses the forces between the tip and the sample [19]. Force acting between the atoms on the tip and sample surface is picked up and is utilized for imaging. This microscope can image surfaces with atomic resolution by scanning a sharp tip across the surface at forces smaller than the forces between atoms. AFM tip experiences the very short range Born repulsive forces for 0.1nm and the long range Van der Waals (VdW) forces up to 10 nm. As the Van der Waals forces decay rapidly on moving away from the surface, it will be negligible for 100-500 nm above the surface where long-range electric - magnetic and capillary forces are prevalent [20].

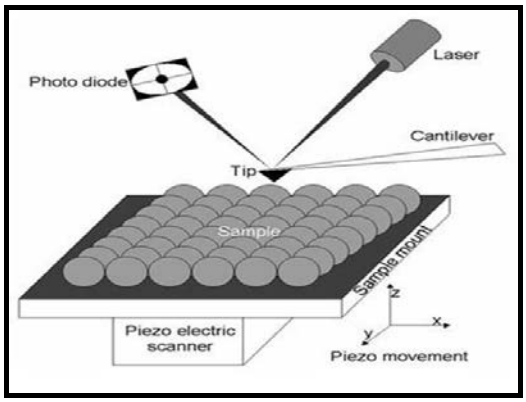

Figure 2.6: Schematic of an AFM

The basic principle of AFM is the interactions between the sample and the probe tip which result in a deflection in cantilever. Van der Waals attractive forces between the atoms are strong enough to move macroscopic objects like AFM cantilevers. When the scanning tip further approaches the sample, the electronic wave functions of the atoms at the tip and sample atoms start to overlap and this gives rise to strong repulsive forces called Born repulsive forces.

Schematic of an AFM is shown in figure (2.6). It consists of piezoelectric scanner like arrangement on which sample is mounted, a cantilever with probe tip, laser and a photodiode. Position of the sample surface with respect to the tip along x, y and z directions is determined by a three dimensional piezoelectric drive. The interatomic forces between the tip and the sample surface atoms compel the cantilever to deflect. A feedback loop is used to keep the force acting on the stylus at a constant level. The cantilever displacement is measured by a deflection sensor. Typically sensors can detect deflections as small as 10^{-2} Å. Measuring the deflection of the cantilever while the tip is scanned over the sample allows the surface topography to be mapped.

Basic equations:

The cantilever with the attached stylus is sandwiched between the AFM sample and the tunnelling tip. It is fixed to a small piezoelectric element called the modulating piezo which is used to drive the cantilever beam at its resonant frequency. The interatomic forces between the tip and the sample surface atoms cause the cantilever to deflect. The AFM sample is connected to a three dimensional piezoelectric drive i.e, the x,y,z scanner .A feedback loop is used to keep the force acting on the stylus at a constant level. The cantilever displacement is measured by a deflection sensor. Typically sensors can detect deflections as small as 10^{-2} Å. Measuring the

deflection of the cantilever while the tip is scanned over the sample allows the surface topography to be mapped [21].

Van der Waals potential between two interacting molecules is given by

$$U_{VdW} = -\frac{C_1}{z^6} \qquad (2.4)$$

where z is the distance between interacting molecules.

Born repulsive interaction expressed as potential is given by

$$U_{rep} = \frac{C_2}{z^{12}} \qquad (2.5)$$

Total intermolecular potential given by the sum of attractive and repulsive force is

$$U = \frac{C_2}{z^{12}} - \frac{C_1}{z^6} \qquad (2.6)$$

where C_1 and C_2 are coefficients for attractive and repulsive interactions respectively.

VdW potential between the spherical tip end and the plane surface is expressed as,

$$U_{VdW} = -\left(\frac{AR}{6z}\right) \qquad (2.7)$$

where A is the radius of the sphere and R is Hamaker constant.

According to the nature of the tip motion, AFM operates in three different modes namely contact mode, tapping mode and non-contact mode. Contact mode is also known as repulsive mode. In this mode an AFM tip is brought in soft physical contact with the surface of the sample at a certain value of the force. The sharp probe tip which is of a pyramidal-shaped etched silicon nitride tip, is attached to the cantilever with a low spring constant, typically between 0.06 N/m and 0.6 N/m. Contact force causes deflection in cantilever in accordance with the crest and troughs on surface as it traces the tip across the sample. In tapping mode, the silicon probe tip

oscillates at a frequency near to the resonance frequency as it rasters across the sample surface. A suitable height from the sample surface is always maintained by the cantilever and in turn, amplitude of oscillation is lowered by the interactive forces whenever the tip approaches surface. Tapping mode does not provide much atomic resolution but appears to be advantageous considering the less damage done to sample surface. In non-contact mode, the tip does not touch the sample surface. Long range forces acting between the tip and sample reduce the resonance frequency which in turn maintains constant amplitude of oscillation or frequency by adjusting the tip to sample distance. This distance is used to generate the topographical image of the sample surface without damaging the sample surface [22-24].

An advantage of AFM is that it is applicable for studying all types of surfaces, conducting, semiconducting and insulating since it functions on interatomic forces other than diffraction or electron bombardment.

2.3.6. Composition Analysis

2.3.6.1. X-Ray Photoelectron Spectroscopy (XPS)

X-Ray photoelectron spectroscopy (XPS) also known as Electron Spectroscopy for Chemical Analysis (ESCA) is a chemical surface analysis method. It is an ideal tool for ascertaining the surface structure and composition where the sensitivity extends to a few monolayers on the surface. ESCA is a quantitative spectroscopic technique that measures the elemental composition, empirical formula, chemical state and electronic state of the elements that exist on the surface of the specimen (top 1 to 10nm). The basic principle behind X-Ray photoelectron spectroscopy is the photoelectric effect. In XPS, X-rays bombard a sample creating ionized atoms and ejecting free electrons. Photo-ionization and analysis of the kinetic energy distribution of the emitted photoelectrons are utilized to study the composition and electronic state of the surface region of a sample. X-

rays with a photon energy of 200-2000 eV called soft X-rays are generally used in XPS to examine core-levels.

X-ray photon is absorbed by an atom in a molecule or solid, leading to ionization and the emission of a core (inner shell) electron. The number of emitted photoelectrons as a function of their kinetic energy is measured using any appropriate electron energy analyser and a photoelectron spectrum is thus recorded. Figure (2.7) shows the photoelectron emission process involved in XPS.

The process of photoionization can be considered as follows.

$$A + h\nu \rightarrow A^{+} + e^{-} \qquad (2.8)$$

Conservation of energy then requires that :

$$E(A) + h\nu = E(A^{+}) + E(e^{-}) \qquad (2.9)$$

Since the electron's energy is present solely as kinetic energy (KE) this can be rearranged to give the following expression for the KE of the photoelectron:

$$KE = h\nu - (E(A^{+}) - E(A)) \qquad (2.10)$$

The final term in brackets represents the difference in energy between the ionized and neutral atoms which is generally called the binding energy (BE) of the electron which leads to the following commonly quoted equation :

$$KE = h\nu - BE \qquad (2.11)$$

In addition, Φ is the work function of the solid when KE is counted near surface, however, KE is detected by analyzer then Φ is the work function of analyzer. Considering the work function Φ, KE relation changes to

$$KE = h\nu - BE - \Phi \qquad (2.12)$$

Intensity of photoemission is proportional to the intensity of photons and kinetic energy of photoemission is inversely proportional to binding energy. Since each element has unique set of core levels, KE's can be used

to fingerprint the element. There will be no photoemission for hν<ϕ and from levels with BE+ϕ> hν.

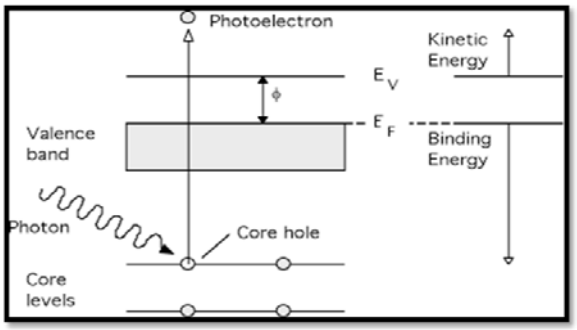

Figure 2.7: Photoelectron emission process in XPS

The basic requirements for a photoemission experiment are:

1. A source of fixed-energy radiation (an X-ray source).
2. An electron energy analyzer (which can disperse the emitted electrons according to their kinetic energy, and thereby measure the flux of emitted electrons of a particular energy).
3. A high vacuum environment (to enable the emitted photoelectrons to be analyzed without interference from gas phase collisions).

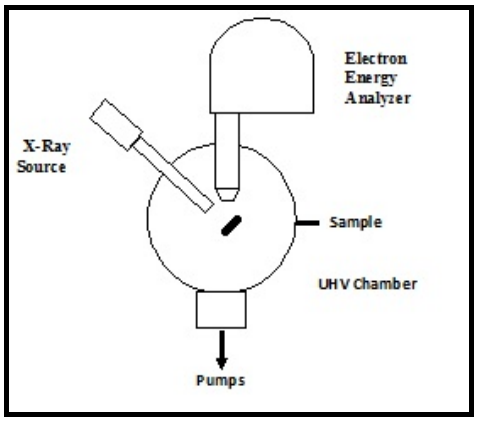

Figure 2.8: Schematic of XPS

Schematic of XPS is shown in figure (2.8). As the photons of X-ray strike the sample, photoelectrons will be ejected. A lens system focuses the

photoelectrons into an energy analyzer. The analyzer is hemispherical. It filters the photoelectrons depending on their kinetic energy. The photoelectrons enter the analyzer in straight line. They will be exposed to an electrostatic field and their paths will be bended with different radius for different kinetic energy. The curved paths will reach a detector. The electrons arriving at the detector will be converted to a signal [14, 16].

2.3.6.2. Rutherford Backscattering Spectrometry (RBS)

Rutherford Backscattering Spectrometry (RBS) is a method of material analysis and takes advantage of the elastic scattering of projectile ions on atomic nuclei. By measuring the backscattering of a beam of high energy ions, information about composition and thickness of the film can be obtained. An RBS instrument consists of an ion source, an electrostatic ion accelerator and a detector. The interaction of the projectile ion with the target atoms is carried out via Coulomb forces [17].

The RBS theory is based on the elastic scattering of the incident ions due to the Coulomb repulsion between ions and target atoms. An ion with initial energy E_0 and mass M_i has, after scattering on a target atom with mass M_t (initially at rest), the energy of the back-scattered ion E_1 is given by:

$$E_1 = E_0\left[\left(\frac{1}{M_i + M_t}\right)\left(M_i\cos\theta + \sqrt{M_t^{\,2} - M_i^2\sin^2\theta}\right)\right]^2 \qquad (2.13)$$

$$E_1 = E_0 K \qquad (2.14)$$

where θ and K are the scattering angle and the kinematic scattering factor, respectively.

From this equation, the mass of the target atom can be determined by measuring the energy of ions back scattered in a given angle. The change in E_1 when M_t changes is observed to exhibit a maximum for the scattering with $\theta=180^0$, which means that the optimum mass resolution is achieved

when the detector is placed as close as possible to direct backscattering through φ = 180◦

If the scattering is due to the Coulomb interaction between the incident ion with charge Zi and a target nucleus with charge Zt, then we define the differential scattering cross section as:

$$\frac{d\sigma}{d\Omega} = \frac{A}{I_0 N}\frac{dI}{d\Omega} \qquad (2.15)$$

where A is the bombarded area , N the number of scattering centers, I is number of scattering events per unit time and I_0 is the number of incident particles per unit time, $\frac{dI}{d\Omega}$ is the observed scattering events in the solid angle dΩ. In the limit Mi<<Mt, scattering cross section is

$$\frac{d\sigma}{d\Omega} = \left[\frac{Z_i Z_t e^2}{16\pi\varepsilon_0 E_i}\right]^2 \frac{1}{\sin^4(\theta/2)} \qquad (2.16)$$

Z_i and Z_t are the atomic numbers of the projectile ions and target atoms respectively. E_i is the incident ion energy, e is the elementary charge. From this equation it is clear that, a large atomic number of projectile ion leads to higher scattering rate. Therefore usually Helium ions are preferred as compared to lighter hydrogen ions. Also the cross section is proportional to E^2.

Another important and material-specific process is the energy loss of the ions as it passes through matter. The dominant process is the scattering of electrons. The energy loss in the material leads to broadened peaks in the spectrum instead of lines. From the peak width layer thickness can be estimated.

The area under the peak A,is given by

$$A = I_0 t_0 \Delta\Omega \left.\frac{d\sigma}{d\Omega}\right|_{E_i} \left[\frac{N}{A}\right] \qquad (2.17)$$

t_0 is the measurement time, $\Delta\Omega$ is the solid angle , N/A is the surface density which is given by

$$\frac{N}{A} = nd\ , \qquad (2.18)$$

where n is the particle density of the known material , d is the thickness of the layer.

For a layer which is composed of two elements, the concentration ratio of the elements can be obtained from combining the above two equations so that

$$\frac{A_1}{A_2} = \left(\frac{n_1}{n_2}\right) \frac{\left.\frac{d\sigma}{d\Omega}\right|_{E_i}^{1}}{\left.\frac{d\sigma}{d\Omega}\right|_{E_i}^{2}} = \left(\frac{n_1}{n_2}\right)\left(\frac{Z_1}{Z_2}\right)^2 , \qquad (2.19)$$

where Z_i's and A_i's are the atomic numbers and areas of the constituent elements respectively [17].

2.3.7. Thermoelectric power measurements

The thermoelectric power (TEP) of the samples was estimated by employing a DC differential method using a home-made set up. In this method, one end of the sample is heated to have a small temperature gradient ΔT across the sample. The thermo emf ΔV is measured across the sample against a reference (refn) material by making a refn-sample-refn thermo couple. The thermoelectric power (S) of the sample is calculated as $S_{sample} = S_{measured} - S_{refn}$, where $S_{measured}$ is $\Delta V/\Delta T$. For an easy and fast sample mounting, the sandwich method was adopted. Low temperature is attained by a 4 K close cycle refrigerator (CCR). Using a controller of the type DRC - 93C from Lakeshore Cryotronics, the temperature difference is controlled so

as to produce a constant thermoelectric voltage by the thermocouple [25 - 26].

The sample with freshly clean surfaces is placed between two identical copper blocks. A chromel-AuFe (0.07%) thermocouple is used to extend the precise measurements down to 4 K. A temperature controller is used to maintain the temperature difference ΔT between the two blocks using the chromel-AuFe (0.07%) thermocouple and a heater wire wound on the lower block. The ΔT can be set to a desired value, say, 2 K. The emf developed across the sample and emf corresponding to the chromel-AuFe (0.07%) thermocouple were measured precisely using a Keithley nanovoltmeter and a scanner system. The Seebeck coefficient of the copper reference (S_{refn}) is subtracted from the measured S_{meas} such that the Seebeck coefficient of the sample is calculated. To obtain the better and stable data, each data point is recorded within 8 s measuring ΔV and ΔT thrice and taking their averages.

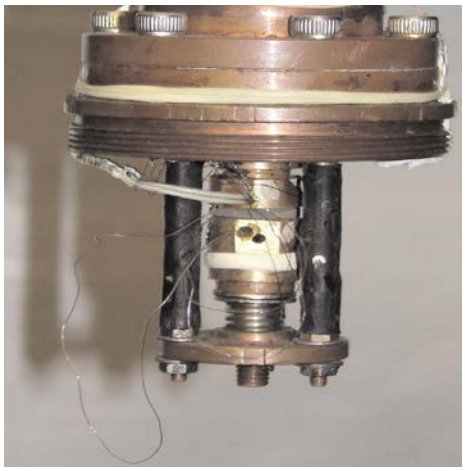

Figure 2.9: Photograph of the thermopower setup built on the cold head of a 4K CCR.

With 4K CCR, the set-up is cooled down to the lowest temperature of 4 K and allowed to warm up naturally by switching off the compressor.

The sample space is evacuated to a vacuum better than 10^{-4} mbar at 300 K before starting the cool down. The dimensions of the setup are so chosen that the typical cool down time is about 75–90 min. The typical time of natural warm-up from 4 to 300 K is about 15 h. The time for changing the sample between two successive runs is about 1 h when the system is at room temperature. Temperature-controlled precise measurement is also possible using CCR. However, this requires the compressor of the CCR to be switched on all the time during experiment. In this case we need two temperature controllers, one for T control and another for ΔT control.

2.3.8. Resistivity and Magnetoresistance Measurements

2.3.8.1Resistivity Measurements

The low temperature DC conductivity of manganite sample is taken by cooling the sample using CTl-CRYOGENICS Model 22C cryodyne cryocooler. Helium is used as the refrigerant and the system is designed to interface with many kinds of apparatus that requires cryogenic temperatures. The pressure maintained in the compressor is 400 PSIG/2758 kPa. The temperature is controlled using Lake Shore Model 321 Autotuning Temperature Controller, which has a stability of ±0.1 K. With the help of INDO VISION Vacuum Pumping System Model VPS-l00 the pressure inside the cryocooler is maintained at 10^{-5}mB.

Resistivity measurements on all the samples were made using conventional d.c. four probe technique. Both the source voltage and current are simultaneously measured by Keithlcy 236 Source Measuring Unit (SMU). This system is automated using a data acquisition system employing Interactive Characterization Software (ICS) version 3.4.1 developed by Metrics Technology Inc. (1997).

For a material of uniform cross section, resistivity ρ is given by

$$\rho = \frac{RA}{l} \qquad (2.20)$$

where R is the resistance of the sample, A is the cross-section area and l is the length across which current is passed.

2.3.8.2 Magnetoresistance Measurement

The magnetoresistive (MR) ratio is defined as the ratio of the change in resistance or resistivity of a material when the field is applied to the resistance/resistivity at zero field, that is,

$$MR = \frac{R_H - R_0}{R_0} \qquad (2.21)$$

where R_H and R_0 represents the resistance of the material in the applied field and zero field respectively.

The resistivity and magnetoresistance measurements are carried out with a conventional d.c. four probe technique by using Keithley source meter and a sensitive voltmeter. This can be measured in two different modes: i) Magnetoresistance as a function of temperature at constant magnetic field. In this mode resistance can be measured as a function of temperature in the absence and in the presence of constant magnetic field. ii) MR as function of magnetic field at constant temperature which can be obtained by measuring the resistance at various magnetic fields at that temperature. If the magnetic field is parallel to the current direction it is known as the longitudinal magnetoresistance A super conducting magnet is used for the production of large magnetic field of the order of several tesla.

An insert for resistivity and magnetoresistance is fabricated. It consists of a sample holder made of square OHFC copper block (12x l2x40 mm'"). On the two opposite faces of each face of the copper block a cigarette paper is fixed with the help of GE varnish. The cigarette paper is used to electrically insulate the samples from the sample holder. Four samples can be loaded on each face. At the four corner of the block, copper strips are attached, on which PCB strips has been fixed as electrical terminals. From

these terminals four uninsulated copper wires (two each for current and voltage leads) for each sample are taken for electrical contacts. The electrical contacts are made with the help of silver paste or indium solder. For temperature measurement, a calibrated Cernox temperature sensor (model no. CX- 1050-SD) is fixed on the sample holder with the help of GE7031 varnish. The sensor has been calibrated with respect to a calibrated Cernox temperature sensor purchased from Lakeshore Cryogenics. A pair-wise twisted manganin wire is wounded around both the ends of copper block as a heater for homogeneous heating. This copper block is connected to about one meter long SS tube of diameter 10mm. Ten copper baffles which are equally spaced and having thickness 1mm and diameter 36mm were brazed on the SS tube. These baffles perform as a radiation shield and also utilize the enthalpy of outgoing He gas for efficient cooling. The copper wires of SWG 44 (0.081 mm diameter) are used as electrical leads from sample and temperature sensor to the room temperature end of the insert. SWG 34 (0.234 mm diameter) copper wire is used for the sample holder heater. Both the voltage and current leads are pair-wise twisted separately, for each sample holder. Large numbers of copper wire coming from room temperature to the sample holder may prevent to achieve the lowest temperature. Therefore careful thermal anchoring has been done to overcome this problem.

In this insert, sixteen samples can be loaded at a time. It can be used for resistivity measurements in the absence of a magnetic field in the temperature range 1.5 K - 300 K, with the general-purpose variable temperature insert. For infield measurements same resistivity insert is used with the magnet system, which provides a magnetic field up to 100 kOe and temperature variation 1.5 K to 300 K. The samples are fixed on the sample holder with the help of GE varnish. Silver paint is used for making electrical

contacts. In some cases indium contacts are also used. After making the contact the insert is placed inside the cryostat (VTI or Magnet system) for resistivity and magneto resistance measurements.

Lakeshore temperature controller (DRC-93CA) is used for measuring and controlling the temperature of the sample holder. Keithley Switching System (model 7002) is used to select different samples. A nanovolt scanner card (model 7168) is used for switching between the voltage leads of different samples and a general-purpose scanner card (model 7056) for switching between the current leads. Keithley source meter (model 2400) is used for sending the current through the current leads, and the voltage across the voltage leads is measured by Keithley sensitive digital voltmeter (model 182). The automation program is written in Quick Basic. A PC (HP486) is used for controlling and collecting automated data through IEEE-488 interface. The measurement is started by controlling the temperature of interest using Lakeshore temperature controller. Once the temperature is controlled the scanner selects a particular sample. Then a specified current is passed through the sample and voltage is measured across the voltage leads. After that the current direction is reversed and voltage is measured again. The process is repeated few times to improve the accuracy of the measurement. After that the scanner selects the next sample for measurement and repeats the process. Since one nanovolt scanner card can scan voltage of only eight samples, it is possible to carry out the measurements of a maximum eight samples at a time. Once the measurements of all the samples are completed, the temperature controller sets the next temperature. The process of measurement is repeated after achieving the required temperature stability. The collected data is plotted as resistance versus temperature [27].

2.3.9. Magnetic Measurements

2.3.9.1 Vibrating Sample Magnetometer

Vibrating Sample Magnetometer or VSM is used to measure the magnetic behaviour of magnetic materials. Based on the idea of Faraday's Law of induction, it was put forth by Simon Foner at Lincoln Laboratory MIT in 1955 [28]. Faraday's law tells us that a changing magnetic field will produce an electric field. This electric field can be measured and provides us information about the changing magnetic field. The hysteresis loop parameters namely saturation magnetisation (M_s), coercive field (H_c), remanence (M_r) and squareness ratio (M_r/M_s) can be derived by using VSM. The schematic of a vibrating sample magnetometer is shown in figure (2.10).

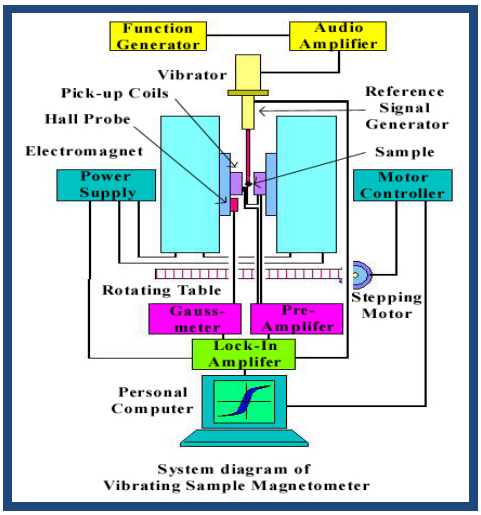

Figure 2.10: Vibrating Sample Magnetometer

In a VSM, the sample to be studied is placed in a constant magnetic field. If the sample is magnetic, this constant magnetic field will magnetize the sample by aligning the magnetic domains or the individual magnetic spins, with the field. The stronger the constant field, the larger the magnetization. The magnetic dipole moment of the sample will create a

magnetic field around the sample, which is called the magnetic stray field. As the sample is moved up and down, this magnetic stray field change as a function of time and can be sensed by a set of pick up coils. A transducer converts a sinusoidal ac drive signal provided by a circuit located in the console in to a sinusoidal vertical vibration of the sample rod and the sample is thus made to undergo a sinusoidal motion in a uniform magnetic field. Coils mounted on the pole pieces of the magnet pick up the signal resulting from the sample motion.

The alternating magnetic field will cause an electric field in the pick-up coil as according to Faradays law of induction, and the current will be proportional to the magnetisation of the sample. The greater the magnetisation, the greater will be the induced current. The induction current is amplified by a trans-impedance amplifier and a lock-in amplifier. The various components are interfaced with a computer. By controlling and monitoring via the software, the system can tell us how much the sample is magnetized and how magnetisation depends on the strength of the constant magnetic field. For a particular field strength, the corresponding signal received from the probe is translated into a value of magnetic moment of the sample. When the constant field varies over a given range, a plot of magnetisation versus magnetic field strength is generated.

When a sample is placed in a uniform magnetic field M, a dipole moment is induced in the sample. Then the amount of magnetic flux linked to the coil placed in the vicinity of this magnetic field is given by

$$\phi = \mu_0 n \alpha M \qquad (2.22)$$

where μ_0 is the permeability of free space, n the number of turns per unit length of coil and α represents the geometric moment decided by position of moment with respect to coil as well as shape of coil.

Anharmonic oscillator of the type,

$$Z = Z_0 + A\exp(j\omega t) \qquad (2.23)$$

induces an emf in the stationary detection coil. The induced emf is given by

$$V = -\frac{d\phi}{dt} = -j\omega\mu_0 nMA(\frac{\partial\alpha}{\partial z})e^{j\omega t} \qquad (2.24)$$

If amplitude of vibration (*A*), frequency ω and $\frac{\partial\alpha}{\partial z}$ are constant over the sample zone then induced voltage is proportional to the magnetic moment of the sample. A cryogenic setup attached to the sample permits low temperature measurements. This is the basic idea behind VSM [23, 24].

2.3.9.2 SQUID Magnetometer

A SQUID (superconducting quantum interference device) magnetometer is a device used to measure extremely sensitive magnetic fields of the order of 10^{-14} T with low noise levels. It consists of two superconductors separated by thin insulating layers to form two parallel Josephson junctions so that electrons can pass through in both directions. Its high sensitivity is associated with measuring changes in magnetic field associated with one flux quantum (h/2e). A schematic of SQUID is shown in figure (2.11).

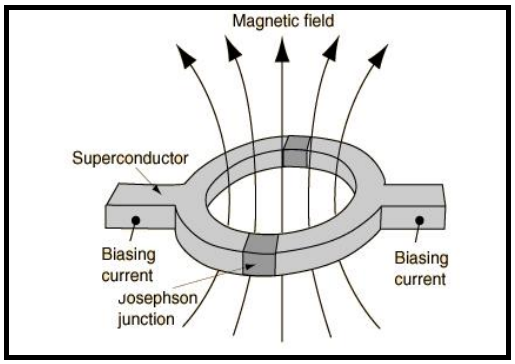

Fig. 2.11: Schematic of a SQUID

The basic principle that follows in a SQUID magnetometer is that, when a constant bias current is maintained in the SQUID device, the measured voltage oscillates with the changes in phase at the two junctions.

This change in phase is caused by change in magnetic flux. Counting the oscillations directly evaluate the flux change which has occurred.

Thus working principle of SQUID is that when the sample is moved through the superconducting magnetic coils, a flux change is induced in the pickup coils. SQUID is basically a flux-to-voltage transducer. Flux-to-voltage characteristic has increased the demand of SQUID for detecting small magnetic field, current, voltage, inductance and magnetic susceptibility. SQUIDs have been used for a variety of testing purposes that demand extreme sensitivity including engineering, biomagnetism and geological equipment including mineral exploration and earthquake prediction [29]. Highly magnetic sample should be moved slowly through the coils without exceeding the maximum slewing rate of the electronic system [23, 30].

2.3.9.3 Field Cooled and Zero Field Cooled Measurements

Zero field cooled (ZFC) and Field cooled (FC) measurements are temperature dependent magnetization measurements which provide a means of investigating the effects of the various magnetic interactions. In an ZFC measurement, sample is cooled from very high temperatures usually much above the T_C for ferromagnets to liquid helium temperatures in the absence of magnetic field. On reaching lowest possible temperature, a small uniform external filed is applied and the net magnetisation is measured while heating the sample at a constant rate. At low temperature and in the zero applied magnetic field, the sample is in equilibrium state, hence exhibits no net magnetization. When sample is cooled in the absence of magnetic field, magnetic moments tend to align along the preferred crystal directions in the lattice, thus lowers the magnetocrystalline energy. Since the orientation of each crystallite differs from the other, net moment is zero. When a small magnetic field is applied, equilibrium state is broken due to Zeeman energy.

But magnetic moments will be locked in their respective orientation and no substantial change in magnetization will be observed since system cannot attain an equilibrium state at such low temperature. As the sample is heated, more thermal energy is available and more moments will be aligned in the direction of magnetic field thus minimizes the Zeeman energy. Thus sample attains an equilibrium state through a relaxation process as temperature goes up. Eventually at a particular temperature, the net magnetization of the system reaches a maximum where the greatest population of moments will have aligned with the external field. On further increasing the temperature, thermal energy will exceed Zeeman energy and the moments will be randomized leading to decrease in magnetization as per Curie's law.

Field cooled measurements proceed in a similar manner to ZFC except that the constant external field (a small magnetic field which lies in the initial permeability region) is applied while cooling and heating. Measurements are carried out as sample is heated to high temperatures. In both FC and ZFC measurements, applied magnetic field should be smaller than the anisotropy field so as to get information of competing magnetic interactions. Also, there is divergence in FC and ZFC curves. This is because, in ZFC, spins corresponding to each particle tend to align with different crystalline axes and will be frozen in that state at low temperatures while in FC, spins from each particle will tend to align with the easy crystalline axis that is closest to the applied field direction and remain frozen in that direction at low temperature. FC and ZFC measurements are considered as most sensitive magnetic measurements for analyzing a close inspection of magnetic behaviour [24, 31].

References

[1] Santhosh D. Shenoy, Ph.D. thesis, Department of Physics, Cochin University of Science and Technology (2004).

[2] E. Muhammad Abdul Jamal, Ph.D. thesis, Department of Physics, Cochin University of Science and Technology (2009).

[3] T. Venkatesan and Steven M. Green, The industrial physicist, **2**, 3, 22-24, (1996).

[4] Andor, an Oxford Instruments company, http://www.andor.com/learning-academy/pulsed- laser-deposition-an-introduction-to- pulsed-laser-deposition.

[5] Yves Pauleau, Chemical Physics of Thin Film Deposition Processes for Micro- and Nanotechnologies, Kluwer Academic publishers, Netherlands (2002).

[6] C. Barry Carter, M. Grant Norton, Ceramic Materials: Science and Engineering, Springer, New York (2007).

[7] Milton Ohring, Materials Science of Thin Films, 2nd edn., Academic press, Santiago, USA (2002).

[8] John Venables, Introduction to Surface and Thin Film Processes, Press Syndicate of the University of Cambridge, United Kingdom (2000).

[9] Scintag, Inc., Chapter 7, Basics of X-ray diffraction, www.scintag.com.

[10] C. Kittel, Introduction to solid state physics, John-Wiley &Sons, New York (1997).

[11] C. Suryanarayana, M. Grant Norton, X-Ray Diffraction: A Practical Approach, Plenum press, Springer, New York (1998).

[12] H. M. Rietveld J. Appl. Crystallogr., **2** (2), 65–71 (1969).

[13] Full Prof manual, http://www.psi.ch/lns-diffraction/MacEN/fullprof-manual.pdf.

[14] Hysen Thomas, Ph.D. thesis, Department of Physics, Cochin University of Science and Technology (2012).

[15] M. Watt, The principle and practise of electron microscopy, Cambridge Uni. Press, Cambridge (1997).

[16] B. David, M.P. Seah, Practical Surface Analysis by Auger and X-Ray Photoelectron Spectroscopy, John Wiley and Sons Ltd, Chichester (1990).

[17] M. Mayer, Rutherford Backscattering Spectrometry (Trieste) (2003).

[18] C. Richard Brundle, Charles A. Evans Jr., Shaun Wilson, Encyclopedia of Materials Characterization, surfaces, Interfaces, thin films, Manning Publications Co.Reed Publishing, USA (1992).

[19] K. Oura, V. G. Lifshits, A. A. Saranin, A. V. Zotov, M. Katayama, Surface science, an Introduction, Springer-Verlag Berlin Heidelberg, Germany (2003).

[20] Greg Haugstad, Atomic Force Microscopy: Understanding Basic Modes and Advanced Applications, John Wiley & sons, New Jersey (2012).

[21] John. C. Vickerman, Surface analysis – the principal techniques, John Wiley & Sons (1997).

[22] W. Richard Bowen, Nidal Hilal, Atomic Force Microscopy in Process Engineering: An Introduction to AFM for improved processes and products, Butterworth Heinmann, USA (2009).

[23] N. Sethulakshmi, Ph.D. thesis, Department of Physics, Cochin University of Science and Technology (2014).

[24] T. N. Narayanan, Ph.D. thesis, Department of Physics, Cochin University of Science and Technology (2010).

[25] L. S. Sharath Chandra, Archana Lakhani, Deepti Jain, Swati Pandya, P. N. Vishwakarma, Mohan Gangrade, and V. Ganesan Rev. Sci. Instrum. **79**, 103907 (2008).

[26] A. Soni and G. S. Okram, Rev. Sci. Instrum. **79**, 125103 (2008).

[27] S. Sagar, Ph.D. thesis, Department of Physics, Cochin University of Science and Technology (2010).

[28] S. Foner, Rev. Sci. Instr. **30**, 548 (1959).

[29] J.C Denardin, A.L Brandl, M Knobel, A.B Pakhomov. H Lin, X.X Zhang, Phys. Rev.B. **65**, 061122 (2002).

[30] K. Gramm, L. Lundgren, Beckman, Physica Scripta. **13**, 93 (1976).

[31] David J. Sellmyer, Yi Liu, D. Shindo, Handbook of Advanced magnetic materials, volume 1: Advanced magnetic materials Nanostructural effects, Tsinghua University press, Springer (2005).

Chapter 3

Colossal thermoelectric power in charge ordered lanthanum calcium manganites ($La_{0.5}Ca_{0.5}MnO_3$)

This chapter deals with the synthesis of Lanthanum calcium manganites ($La_{0.5}Ca_{0.5}MnO_3$) with a composition close to charge ordering, by high energy ball milling and discusses its thermoelectric power in the temperature range of 5K- 300K. Mandal's model has been applied to fit thermoelectric power data in the region below the Curie temperature (T_C). For temperatures lower than120K, due to the co-existence of a charge ordered state with a spin-glass state, the variation of thermoelectric power is maximum and exhibited a colossal peak value. This has been explained by incorporating Kondo properties of the spin-glass along with magnon scattering. FC-ZFC magnetization measurements indicate the existence of a glassy state in the region corresponding to a maximum value of thermoelectric power. Mott's polaronic model has been employed to explain the thermoelectric power observed in the high temperature region ($T>T_C$). X-ray Photoelectron Spectroscopy has been utilised to estimate the Mn^{4+}/Mn^{3+} ratio and it has been found that the ratio is optimal characteristic of a charge ordered compound.

The work discussed in this chapter has been reported in: ***Journal of Applied Physics 116, 213701 (2014)***

3.1 Introduction

Thermoelectric materials are eco-friendly and are promising candidate for energy conversion and are the focus of research recently. Thermoelectric power or Seebeck coefficient is the rate of change of thermoelectric voltage with temperature. It may be noted here that possible applications of thermoelectric materials are in eco-friendly refrigeration, electric power generation by using waste heat and solar heat, temperature controlled-seats, portable picnic coolers and in satellites [1-4]. For a good thermoelectric material, it must have high thermoelectric figure of merit ZT, for practical applications, ZT > 1 [4]. Thermoelectric materials can also find applications in the area of refrigeration based on the principle of Peltier cooling [4]. If the efficiency is significantly improved, thermoelectric devices can be a good solution to today's energy crisis. In order to maximize the thermoelectric figure of merit, a large value of Seebeck coefficient is a pre requisite.

Manganites represent highly correlated electron system and they exhibit a variety of phenomena such as charge, orbital and magnetic ordering, colossal magneto resistance and Jahn-Teller effect [5]. The strong inter-dependence between the magnetic order parameters and the transport coefficients in manganites make much research interest in their thermoelectric power properties [6]. Perovskite class of compounds belonging to the manganites $RE_{1-x}AE_xMnO_3$ [where RE is a rare earth metal and AE is a divalent cation] series satisfies the requirement of low lattice thermal conductivity. Here, large thermal motion or rattling of rare earth atoms (R) with localized magnetic moments is believed to be responsible for low thermal conductivity of these compounds. The 4f levels in these compounds, lying near to the Fermi energy, create large density of states at

the Fermi level and hence they can exhibit a high Seebeck coefficient [7]. Thus manganites are potential materials for thermoelectric applications [8].

The physical properties of mixed valent manganites are determined by both the amount of substitution and average radius of substituted divalent cations [9]. With substitution, the antiferromagnetic (AFM) interactions arising from Mn^{3+}-O-Mn^{3+} tend to compete with the ferromagnetic (FM) interactions resulting from Mn^{3+}-O-Mn^{4+} leads to the evolution of various magnetic phases namely AFM, canted AFM (CAFM) and FM making them magnetically diverse. This is illustrated in their rich magnetic phase diagrams [10]. Out of various compositions in the phase diagram, the composition $R_{0.5}AE_{0.5}MnO_3$ is most interesting [11]. Here, Mn^{3+} and Mn^{4+} are equal in number at this composition and hence ordering of Mn^{3+} and Mn^{4+} species occurs over the lattice, leading to charge ordering and co-existence of antiferromagnetism and ferromagnetism. Below this composition, FM phases are more favourable and above this composition, AFM phases are predominant. As FM and AFM phases co-exist for the charge ordered composition, x=0.5, strong competition between these magnetic phases lead to a magnetically frustrated glassy state (spin-glass) which in turn prevents the occurrence of long range magnetic order [12]. Hence the composition corresponding to x = 0.5 is critical and physical properties close to this composition are unique. It has been pointed out that various effects such as localization due to charge ordering [13], short range magnetic ordering due to spin-glass [12], electron–electron correlation [14], electron-magnon scattering and electron-phonon scattering strongly modify the temperature dependence of transport properties, especially their thermoelectric power [15-17].

Intermediate bandwidth manganites based on calcium, especially, the charge ordered composition, $La_{0.5}Ca_{0.5}MnO_3$, is interesting not only

from a fundamental angle but also from an applied perspective as they are likely to exhibit colossal thermoelectric power. In this chapter we report the thermoelectric power measurements of $La_{0.5}Ca_{0.5}MnO_3$ (coded as LCMO5) prepared by high energy ball milling. Emphasis is laid in studying the phenomenon of colossal thermoelectric power observed at low temperature where magnetic ordering present. Phenomena like the co-existences of ferromagnetic and antiferromagnetic phases in $La_{0.5}Ca_{0.5}MnO_3$ and of charge ordering (CO) is also an interesting aspect in these compounds [18-19]. The valence state of manganese ions and exact composition of powder samples were examined by high resolution core energy level x-ray photoelectron spectroscopy (XPS).

3.2 Experimental

3.2.1 Method of synthesis

Polycrystalline $La_{0.5}Ca_{0.5}MnO_3$ samples were prepared by high energy ball milling based mechano synthesis technique. Stoichiometric amounts of precursor materials La_2O_3, CaO and MnO_2 were mixed and subjected to milling using a planetary model high energy ball mill (Fritsch pulverisette 7). Milling was carried out for 180 minutes with 400 rotations per minute. The powder obtained after milling was calcined in air at 900^oC for 12 hours and then pressed into pellets of cylindrical discs with diameters of 12mm and thickness of 2mm. The pellets were then sintered at 1050^oC for 12 hours.

3.2.2 Characterization

The crystal structure of the sample was determined by using a Rigaku D- Max –C, X-ray diffractometer using Cu K_α radiation of 1.54Å and the fine structure was refined by using Rietveld refinement [FullProf Studio, version2]. The magnetic measurements were performed with a Quantum Design- superconducting quantum interference device (SQUID)-

vibrating sample magnetometer (VSM). Low temperature electrical resistivity measurements were carried out using an indigenous resistivity/magnetoresistance setup along with superconducting 8-Tesla magnet. Resistance is measured in longitudinal geometry using a standard four probe technique. The thermoelectric power (TEP) of the sample was estimated by employing a DC differential method over a temperature range of 5K-300K using a home-made set up. To determine the average Mn valence and composition, x-ray photoelectron spectroscopy was performed [Omicron Nanotechnology XPS system with a monochromatic Al K_α radiation ($h\upsilon$ = 1486.6 eV), source voltage: 15 kV and emission current: 20 mA]. The XPS spectra was then deconvoluted using the Casa XPS program (Casa Software Ltd, UK) in which the background correction was simulated using the Shirley function and peak fitting using a Gaussian-Lorentzian function. The recorded binding energy (BE) spectra were calibrated employing BE of aliphatic carbon at 284.6 eV with a sensitivity of ± 0.2 eV.

3.3 Results and Discussions

3.3.1 Structural studies using XRD

The crystal structure of the sample was determined by using X-ray diffraction. The X-ray powder diffraction pattern of LCMO5 is shown in figure 3.1.a. The XRD peaks correspond to an orthorhombically distorted perovskite structure with Pbmn space group. All peaks are indexed as per ICDD no.46-0513. The average particle size estimated from XRD data using Scherrer's formula is 34nm. The XRD data have been analyzed by refining the experimental data using a standard Rietveld refinement technique. The Rietveld refined pattern of XRD is shown in figure 3.1.b. The refined lattice parameters determined at room temperature are as follows: a = 5.414 Å, b = 7.683 Å and c = 5.428 Å, which are consistent with earlier reports [20]. The

occupancy of La^{3+} and Ca^{2+} obtained from the Rietveld analysis is found to be 0.498 and 0.501, respectively.

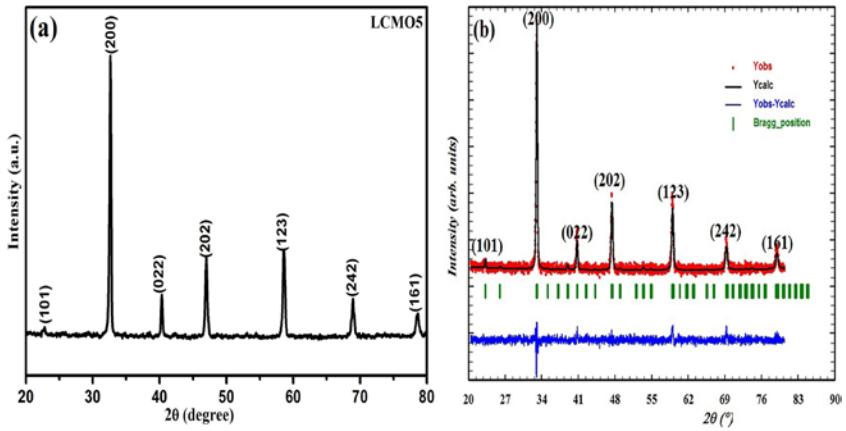

Figure 3.1: (a) XRD pattern for LCMO5. (b) Rietveld refinement performed on LCMO5.

3.3.2 Compositional analysis using XPS

Since the mixed valence ratio of manganese (Mn^{4+}/Mn^{3+}) is a crucial factor in controlling magnetic and transport properties, XPS measurements of charge ordered manganite, $La_{0.5}Ca_{0.5}MnO_3$, were performed. A typical wide scan XPS spectrum for LCMO5 is shown in figure 3.2. The spectrum exhibits characteristic photoelectron lines of Ca, La, O, Mn and C. The C 1s peak corresponds to the unavoidable contaminant carbon on the top surface of the specimen. For a thorough interpretation of the XPS data, a slow scan of the core energy levels with peaks having highest intensities corresponding to Mn 2p, La 3d, La 4d, Ca 2p and O 1s were recorded. Peaks corresponding to Mn 2p [21], La 3d [22], La 4d [23], Ca 2p [24], and O 1s [25] are consistent with earlier reports. The surface stoichiometry is found to be $La_{0.494}Ca_{0.505}MnO_3$ where the ratio of La^{3+} and Ca^{2+} ions is 0.978, which is comparable with the value of 0.995 obtained from XRD.

Figure 3.3.a shows the detailed XPS spectrum of Ca 2p which contains a doublet where the line positions of $Ca2p_{3/2}$ and $Ca2p_{1/2}$ are respectively assigned to binding energies 347.5± 0.2eV and 351.2± 0.2eV. The observed spin orbit splitting between $Ca2p_{3/2}$ and $Ca2p_{1/2}$ components is about 3.7eV. The single peak structure of Ca 2p of LCMO reveals that Ca in LCMO exists in a single oxidation state of +2. The binding energies of Ca 2p are almost identical to previous studies [24].

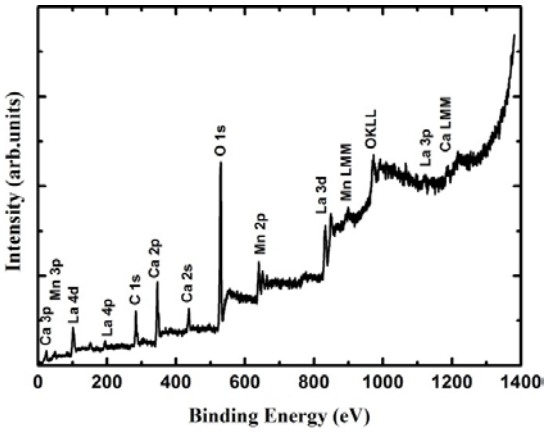

Figure 3.2: XPS survey scan of LCMO5

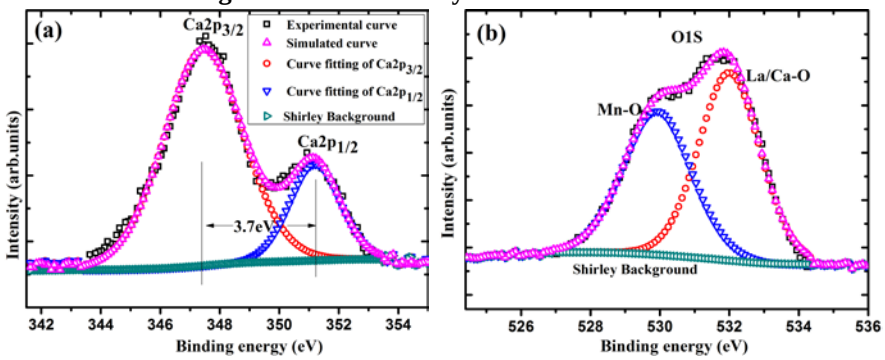

Figure 3.3: (a) Ca 2p XPS spectrum (b) O 1s XPS spectrum

The narrow scan spectrum of the oxygen 1s core level of $La_{0.5}Ca_{0.5}MnO_3$ is shown in figure 3.3.b. For a perfect Lorentzian- Gaussian curve fitting, oxygen peaks corresponding to O1s can be resolved into two components; one at around 529.9± 0.2eV and the other at about 532.1±

0.2eV.This doublet peak of O1s agrees with the earlier reports on ABO_3 type perovskites [22, 26-27]. Jaewu Choi *et. al* observed two peaks at 529eV and 531.4 eV for O 1s in $La_{0.65}Ca_{0.35}MnO_3$ and $La_{0.9}Ca_{0.1}MnO_3$ [25]. Daniel Hsu *et. al* assigned this doublet peak to the chemical shifts in the oxygen core level arising out of two kinds of chemical bonding, the lower binding energy component corresponding to Mn-O bonding and the higher binding energy to La/Ca-O bonding [28]. Since the intensities of peaks 529.9± 0.2 eV and 532.1± 0.2eV are comparable, both these bonds have equal probability of occurrence.

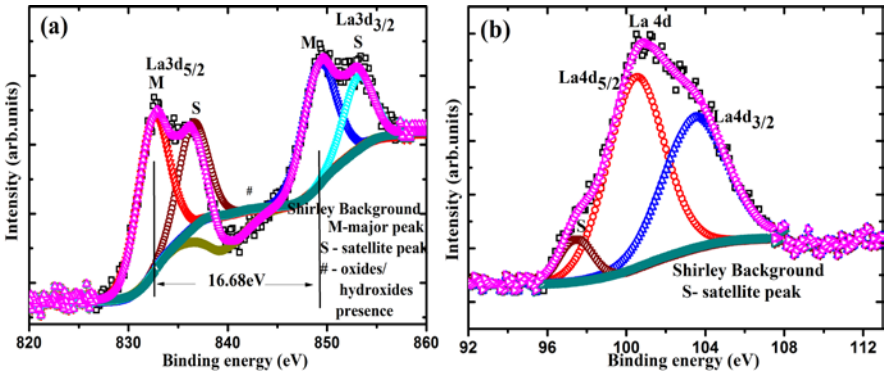

Figure 3.4: XPS spectrum of (a) La3d (b) La4d

Figure 3.4.a shows the resolved spectrum of La 3d doublet. Due to spin – orbit interaction 3d spectrum of Lanthanum consists of two peaks corresponding to $3d_{5/2}$ and $3d_{3/2}$ in the range of 830eV-860eV. These doublets show double peak structures in addition to an oxide /hydroxide peak of La compounds by accompanying satellite peaks with comparable intensity to main peaks. The satellite peaks observed have been interpreted in terms of electron transfer process where an outer electron from the lower energy valence p orbital of oxygen ligand is excited to the empty 4f orbital of Lanthanum. Thus each double correspond to states with configurations $3d^9 4f^0 L$ for lower binding energy main peak and $3d^9 4f^1 \underline{L}$ for higher binding energy satellite, where L represents oxygen ligand and the underlining

indicates a hole. According to Gauss fitting curves, the lower binding energy peak of La $3d_{5/2}$ is found to be at 832.5± 0.2eV and the other at 836.5± 0.2eV corresponds to higher binding energy satellite. Also for La $3d_{3/2}$ the lower BE peak state $3d^9 4f^0 L$ and higher BE satellite state $3d^9 4f^1 \underline{L}$ are respectively observed at 849.2± 0.2eV and 853.2± 0.2eV.The spin orbit splitting between $3d_{5/2}$ and $3d_{3/2}$ is around 16.7eV which is close to the reference values of 16.8eV [22]. The detailed XPS spectrum of La 4d shows that peak of $La4d_{5/2}$ with satellite peak at 97.4± 0.2eV is observed at 100.5± 0.2eV and the one corresponding to La $4d_{3/2}$ is observed at 103.5± 0.2eV, which are also close to the reference values. The XPS spectrum of La 4d is shown in figure 3.4.b.

The mixed valence of manganese in perovskite manganites was determined by analysing the manganese doublet spectra (figure 3.5). The spin–orbit split of manganese 2p peaks correspond to $Mn2p_{3/2}$ and $Mn2p_{1/2}$ are located at around 642.1eV and 653.5eV respectively (figure 3.5. a) and the doublet separation is around 11.5eV, which is in good agreement with earlier reported value of 11.8 eV in LCMO [28].

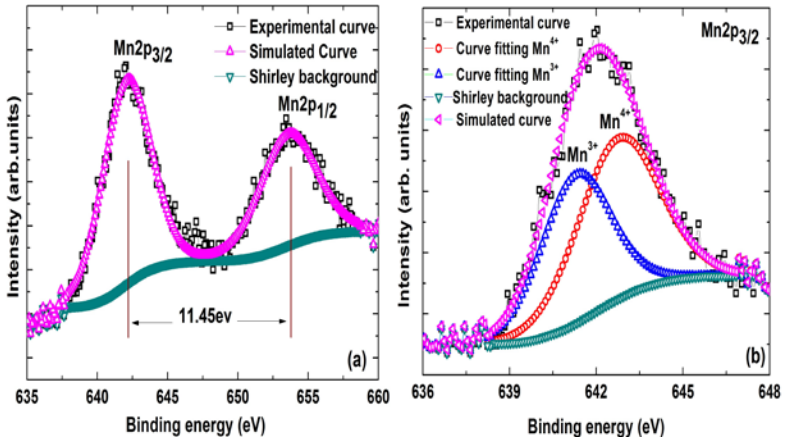

Figure 3.5: (a) Mn 2p core level XPS spectra including the $Mn2p_{1/2}$ and $Mn2p_{3/2}$ core levels and (b) $Mn2p_{3/2}$ spectrum and fitted curves.

Evidence for the existence of mixed valence states of manganese is obtained from the curve fitting results correspond to the Mn $2p_{3/2}$ spectra. It

is evident from figure (3.5.b) that two valence states of manganese are needed for a proper fit. From literature, it is observed that Mn^{2+} peaks are assigned with lower binding energy than Mn^{3+} and $Mn^{4+}$and also Mn^{3+}peaks are observed at 641.7eV. Hence in the present study, the high binding energy component located at 642.7 ± 0.2eV with FWHM (full width at half maximum) of 2.6eV corresponds to Mn^{4+} while the lower one located at 641.3 ± 0.2eV with FWHM of 2.2eV is related to the presence of Mn^{3+}. These values are in close proximity with reference values of 641.3 and 642.8 eV of Mn $2p_{3/2}$ in $La_{2/3}Sr_{1/3}MnO_3$ composites [21]. Average concentration of Mn^{3+} obtained by analyzing the Mn 2p doublet structure is found to be 48.28% and that of Mn^{4+} is 51.72%. The mixed valence manganese ratio of Mn^{4+}/Mn^{3+} in the present case is ~1.07,which is characteristic of a charge ordered compound.

3.3.3 Magnetic Characterization using FC/ZFC and MH loops

Temperature dependent ZFC and FC magnetization was measured in different applied magnetic fields of 25, 50 and 200 Oe to correlate the co-existence of spin-glass ordering with charge ordering (CO) in LCMO5.

The results are presented in figure 3.6. It can be noted that there is irreversibility in the FC and ZFC magnetisation for temperatures less than 250 K. For higher temperatures, both FC and ZFC magnetisation have similar temperature dependencies. From the FC magnetisation obtained by applying a field of 200 Oe it is clear that a paramagnetic to ferromagnetic transition takes place at around 235 K. Just below this ordering temperature, a slope change in the M-T plot is observed at 200K which is attributed to the charge ordered transition (T_{CO}) in this composition [29]. In the FC mode, as the temperature is further reduced, the magnetisation increases resulting in a slope change in M-T curve at around 55K. Thereafter below 50 K, the magnetisation is nearly independent of temperature. On the other hand, the

magnetisation recorded after zero field cooling shows a peak at intermediate temperatures of around 55 K. During zero field cooling from 300 K to 10 K, the moments will be randomly frozen to form a glassy state due to the competing FM-AFM interactions in the system. Subsequent warming of the system in an applied magnetic field will aid the randomly frozen moments to align along the field direction. This result in a rise in ZFC moment and once the thermal energy overrules Zeeman interaction, the ZFC moment starts decreasing resulting in a peak in ZFC magnetisation around the spin-glass transition temperature.

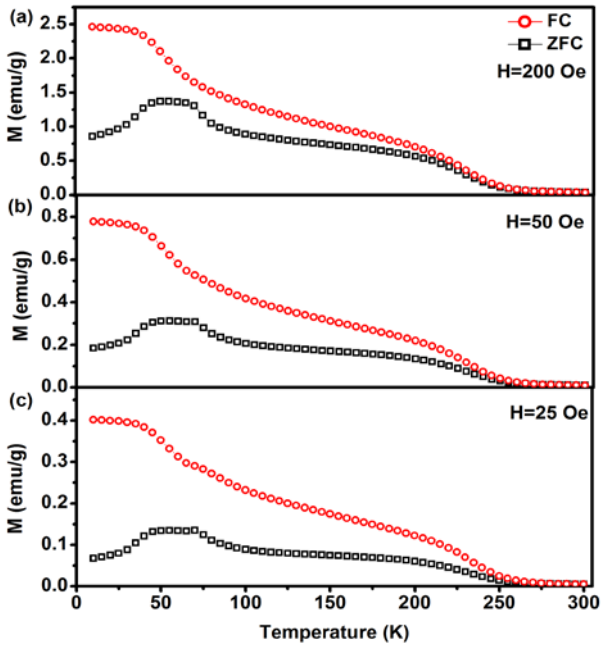

Figure 3.6: Magnetization measurements under ZFC and FC conditions in a magnetic field of (a) 200 Oe, (b) 50 Oe and (c) 25 Oe.

Moreover, from figure 3.6 it can be noted that the irreversible temperature in the FC/ZFC magnetisation increases with decrease in the applied field, which is also a characteristic of a spin-glass system. Dagotta *et al.* reported an AFM spin ordering referred to as canted AFM spin ordering at low temperatures for charge ordered compositions [12]. Since the nominal

ratio, Mn^{4+}/Mn^{3+} ~ 1, LCMO5 qualifies to be a charge ordered composition. The broad peak at low temperatures observed in ZFC can be because of the overlapping of peaks and can be due to both the frustrated glassy transition and the AFM spin ordering [12, 30]. The results indicate that a frustrated magnetic phase has nucleated below T_{CO} due to the co-existence of COAFM and FM phases at very low temperatures [30]. Earlier, Garcia-Landa *et.al* has claimed the co-existence of charge order state with a cluster glass state at low temperatures in $Gd_{0.5}Sr_{0.5}MnO_3$ [31]. Hence at low temperature, in LCMO5, the charge ordered state coexists with a spin-glass state.

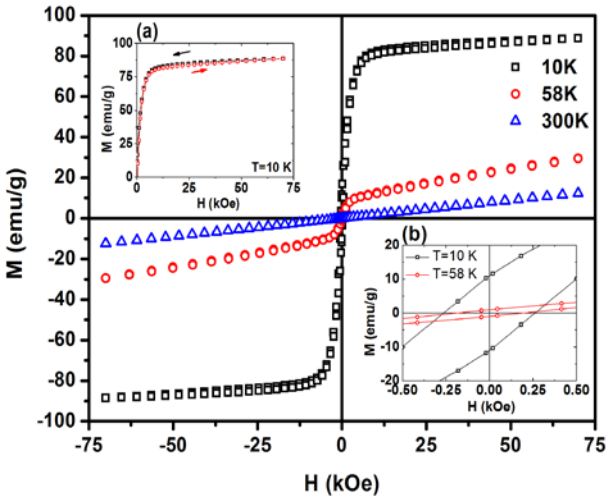

Figure 3.7: M-H loops of $La_{0.5}Ca_{0.5}MnO_3$ at 10K, 58K and 300K. The inset (a) shows an enlarged view of M-H at 10K and the inset (b) shows the zoom in figure of M-H at 10K and 58K

The M-H loops of $La_{0.5}Ca_{0.5}MnO_3$ measured at 10K, 58K and 300K are presented in figure 3.7. Please note that the magnetisation measurements were performed by sweeping the field from +70kOe to -70kOe and vice versa. The magnetisation curves show a non saturating behaviour even after the application of a fairly high magnetic field of 70 kOe. For the M-H curve measured at 10 K, the magnetisation shows two distinct field dependencies. In the high field part, the magnetisation is non saturating and the

susceptibility is small indicating contributions from a CO antiferromagnetic phase. While in the low field regime, the susceptibility is high similar to that expected from a ferromagnetic phase. Further, a hysteresis can be observed in the high field part of the M-H curve (inset (a) in fig 3.7). This indicates the existence of a meta magnetic FM phase formed by the partial transformation of the COAFM phase under high field. This meta magnetic transition is associated with the quenching of the CO state and emergence of FM ordering. The appearance of a meta magnetic transition for LCMO5 is a clear signature of the coexistence of FM and COAFM phases and the competing FM-AFM interaction in LCMO5 results in a spin-glass transition at T<50K. Earlier reports on calcium doped praseodymium manganites with x= 0.3, 0.4, 0.5 strongly supports the presence of such meta magnetic transitions at higher fields [18, 32]. Previous reports on the meta magnetic transition in manganites is based on the co - existence of a FM phase in the COAFM matrix [32-34]. When the temperature is increased to 58K, signatures of this meta magnetic transition is still visible although the high field hysteresis is reduced due to thermal excitation. At 300 K, the measured M-H curve for LCMO5 is characteristic of a typical paramagnet. The hysteresis loop of LCMO5 at 10K exhibits a coercive field of 260 Oe, whereas at 58K the coercivity decreases to 150 Oe (inset b in fig 3.7). This coercivity decrement with increasing temperature also supports spin-glass like transition in LCMO5. It is to be noted that preparative conditions do alter size/ grains of particles of magnetic materials and therefore, preparative conditions do have an indirect bearing on the coercivity of these samples [35-36]. Earlier, Iniama *et al* reported on the particle size dependence of LCMO5 on coercivity [37]. They reported that coercive field is negligible for bulk samples, whereas with decreasing particle size, coercivity enhances.

3.3.4 Thermoelectric power studies

The temperature dependent thermoelectric power (S) of $La_{0.5}Ca_{0.5}MnO_3$ measured in the temperature range from 5K to 300K is shown in figure 3.8. The temperature dependence of S is more pronounced below the Curie temperature, and a further decrease in temperature results in a broad peak at around 58K exhibiting a colossal thermoelectric power of -80mV/K. It may be noted that a large value of the order of 80mV/K for TEP is not found to be reported in literature. Negative thermoelectric power throughout the whole temperature region indicates the presence of electrons as charge carriers which is consistent with earlier reports on thermoelectric power of heavily doped calcium lanthanum manganites [38-39]. The most important temperature region for this composition is $T<T_C$ especially $T<200K$ (T_{CO}) where the system enters into the charge ordered state. The variation of electrical resistivity with temperature as shown in the inset of figure 3.8 indicates that there is a semiconductor like behaviour with an upturn at charge ordered (CO) state temperature. In addition to this, a weak dependence of resistivity with temperature below 120K indicates the existence of Kondo behaviour.

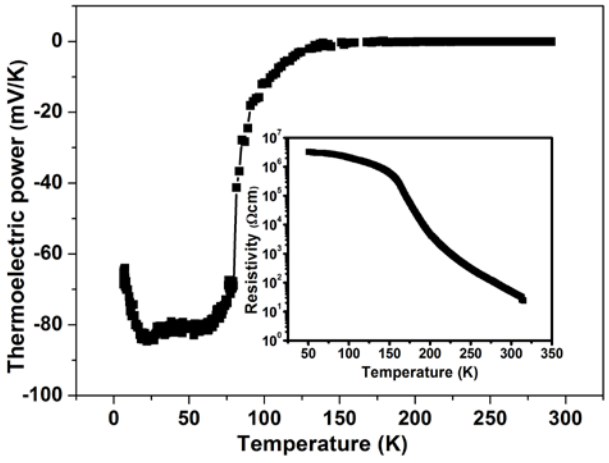

Figure 3.8: Temperature dependence of thermoelectric power from 5K to 300 K. The inset shows the resistivity as a function of temperature.

3.3.4.1 Low temperature behaviour

A major variation in thermoelectric power is observed in this charge ordered region, where for temperatures T<120K, this variation of thermoelectric power is maximal and exhibit a peak value of -80mV/K at 58K. For this specific region, the charge ordered state co-exists with the spin-glass state as deduced from ZFC magnetization measurements. Hence the above mentioned prominent variation in thermoelectric power with respect to temperature below T_C has been analyzed based on the charge ordered spin-glass state.

There is no general relationship to interpret TEP corresponding to the FM region. Earlier Blatt *et al.* explained the broad peak observed in S at low temperature for iron by magnon drag [40]. Later Mandal interpreted the low temperature TEP data of divalent doped manganites by adopting a spin wave theory giving due attention for magnon drag interactions [6]. He analyzed the TEP data in the FM phase using an expression

$$S = S_0 + S_{3/2}T^{3/2} + S_4T^4 \qquad (3.1)$$

where S_0 (S at T=0) is a constant which accounts for truncating the low temperature thermoelectric power data, $S_{3/2}T^{3/2}$ is attributed to the magnon drag contribution which strongly influences the low temperature TEP data in manganites and S_4T^4 is accredited to the spin wave contribution. The present TEP data in the low temperature region, especially where CO co-exist with a spin-glass, the prominent peak observed at 58K cannot be completely fitted by the model presented by Mandal. Since LCMO5 is a critical composition which lies in the boundary between the FM and COAFM phase of this series, FM and COAFM phases co-exist leading to a magnetically frustrated glassy state.

In the present investigation, the temperature corresponding to the colossal thermoelectric power peak value of ~80mV/K observed is close to

the spin-glass transition temperature. FC/ZFC magnetization measurements in the charge ordered spin-glass region (T<120K) indicates the existence of both frustrated glassy state and a AFM spin ordering. Thus by both glassy and AFM spin ordering, charge carriers are localized at the sites. Hence the role of competing AFM phases due to charge ordering, and spin-glass becomes more prominent in this region. Below this transition temperature, TEP tends to decrease which can be due to an increase in magnetic ordering with decrease in temperature. Earlier reports on thermoelectric power of spin-glasses showed giant values at low temperatures [41-43]. Later K.H Fischer modelled the TEP in the spin-glass region by considering a Kondo term, S_2T^2, and a resonance term, S_1T, with opposite sign which lead to a change of sign of TEP at a characteristic temperature T_0 [44]. But in the present system, there is no change of sign of TEP. So the term corresponding to this sign change, the resonance term, is not considered. Therefore, it is possible to explain the observed prominent peak at 58K by incorporating Kondo properties of the spin-glass along with magnon scattering as proposed by Mandal. Thus in the low temperature region (T<120K) we have analyzed the TEP data by using the expression

$$S = S_0 + S_{3/2}T^{3/2} + S_2T^2 + S_4T^4 \qquad (3.2)$$

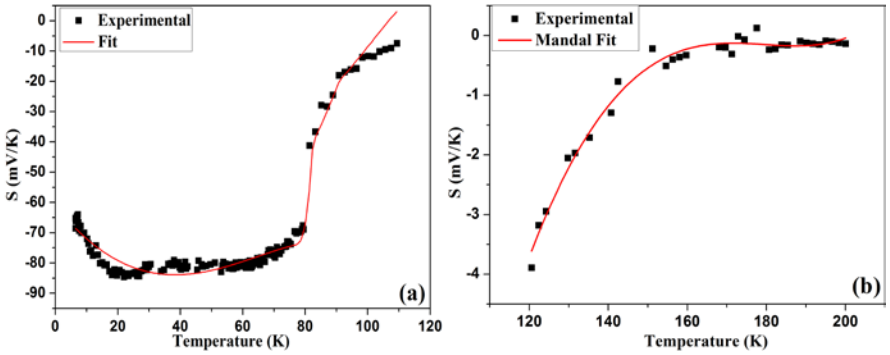

Figure 3.9: Variation of S with T (a) at T<120K, (b) at 120K<T<T_C. The solid line gives the best fit to equations.

The experimental data fits well as per equation 3.2 and is shown in figure 3.9.a and the fitted parameters are listed in table 3.1. It can be seen that the TEP in the very low temperature regime not only consists of term corresponds to magnonic origin but also have a charge ordered spin-glass contribution as well. However, to explain TEP data in the region $120K<T<T_C$ instead of the spin-glass contribution, a phonon drag term is included in Mandal's model. Fitting of TEP in the remaining CO regime using the following equation

$$S = S_0 + S_{3/2}T^{3/2} + S_3T^3 + S_4T^4 \qquad (3.3)$$

points out that in addition to magnon drag produced by electron-magnon interaction, a T^3-dependence of S due to phonon drag produced by electron-phonon interaction is also significant in this region. The TEP data measured in the temperature range $120K<T<T_C$ fitted to equation 3.3 is shown in figure 3.9.b. From the fitted values the magnon drag contribution is more prominent since due to charge ordering the magnetic phase is transformed to AFM. Thus the combined contribution of both spin-glass and charge ordering gives rise to a colossal thermoelectric power in the low temperature regime ($T< T_C$).

Table 3.1. The best fit parameters of the experimental TEP data measured in the temperature range T<120K and 120K<T<T_C. NC stands for no contribution.

Temperature region	S_0 *(mV/K)*	$S_{3/2}$ *(mV/K$^{5/2}$)*	S_2 *(mV/K^3)*	S_3 *(mV/K^4)*	S_4 *(mV/K^5)*
T<120K	**-61.12**	**1.27**	**-0.018**	**NC**	**7.49E-7**
120K<T<T_C	**-61.76**	**0.69**	**NC**	**-2.15E-5**	**5.98E-8**

3.3.4.2 High temperature behaviour

The charge ordered composition LCMO5 exhibits an appreciable Seebeck coefficient in the high temperature region ($T>T_C$). Due to the optimal Mn^{4+} -Mn^{3+} concentration in LCMO5, distortion became prominent so that the charge carriers are trapped and gives rise to polarons. Hence the transport mechanism involves hopping through polarons. The thermoelectric power data in the high temperature region ($T>T_C$) is interpreted by using Mott's well known equation [45] based on polaron hopping.

$$S = \frac{k_B}{e}\left[\frac{E_S}{k_B T} + \alpha'\right] \qquad (3.4)$$

where k_B is the Boltzmann constant, e is the electronic charge, E_s is the activation energy for conduction obtained from thermoelectric power data and α' is a constant of proportionality between the heat transfer and kinetic energy of an electron. α' < 1 implies the existence of small polarons, while for α' > 2 suggests that the conduction involves large polarons [46]. From the slope of the straight line fit to the S versus 1/T plot, activation energy of $E_S = 17.14 meV$ and from the y intercept, the constant $\alpha' = 0.315$ is obtained. The value of α' < 1 indicates the presence of small polaron carriers in the high temperature region. Figure 3.10 shows the best fit curve of S versus 1/T plot.

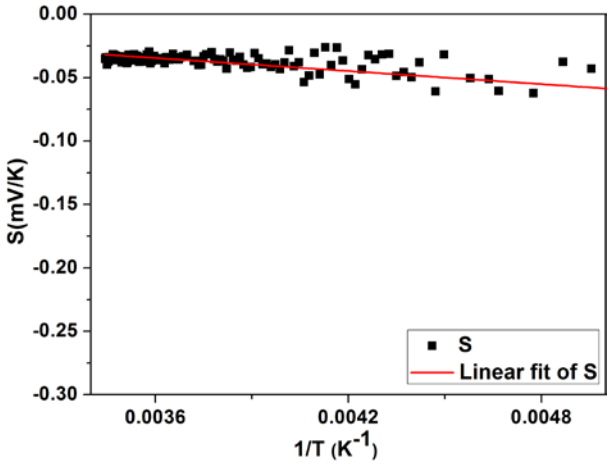

Figure 3.10: Variation of S with 1/T for T >T_C. The solid line gives the best fit to equation (3.4).

3.4 Conclusions

The single phase charge ordered composition $La_{0.5}Ca_{0.5}MnO_3$ was synthesized by high energy ball milling. The sample possessed a distorted orthorhombic perovskite structure with a Pbmn space group. A colossal thermoelectric power of -80mV/K at 58K was observed. Both the surface composition and the optimal Mn^{4+}- Mn^{3+} concentration in charge ordered LCMO5 was examined by XPS analysis. A strong competition between the FM and AFM order due to charge ordering results in a spin-glass state in the temperature regime T<120K. The observed colossal thermoelectric power was explained based on the charge ordered spin-glass state. The colossal Seebeck coefficient value at 58K was explained by incorporating Kondo properties of the spin-glass along with magnon scattering as proposed by Mandal. The Kondo dependence is clearly visible from the resistivity variation. TEP data in the charge ordered region (120<T<T_C) is explained by including a phonon drag term in Mandal's model, instead of a spin-glass contribution.Thermoelectric power in the region above the Curie temperature is due to the presence of small polaron carriers in the high temperature

region. The frustrated glassy state and AFM spin ordering at low temperatures leads to localization of charge carriers which manifests in the form of colossal thermoelectric power.

References

[1] L. E. Bell, Science **321**, 1457 (2008).

[2] J-F. Li, W-S.Liu, L-D. Zhao and M. Zhou, NPG Asia Mater. **2(4)**, 152 (2010).

[3] J. Zheng, Front. Phys. China.**3**, 269 (2008).

[4] G. J. Snyder and E. S. Toberer, Nat.Mater.**7**, 105 (2008).

[5] J.M. D. Coey, M. Viret, and L. Ranno, Phys. Rev. Lett. **75**, 3910 (1995).

[6] P. Mandal, Phys. Rev. B **61**, 14675 (2000).

[7] T. M Tritt and M. A. Subramanian, MRS Bull.**31,** 188 (2006).

[8] A.Maignan, S.Hebert, P.Li, D.Pelloquin, C.Martin, C.Michel, M. Hervieu and B.Raveau, Cryst. Eng.**5**, 365 (2002).

[9] J. M. D. Coey,M. Viret and S. von Molnaír, Adv. Phys.**48**, 167 (1999).

[10] P. Schiffer, A. P. Ramirez, W. Bao, and S.-W. Cheong, Phys. Rev. Lett. **75**, 3336 (1995).

[11] P. G. Radaelli, D. E. Cox, M. Marezio and S-W.Cheong, Phys. Rev. B **55,** 3015 (1997).

[12] E. Dagotto, T. Hotta and A. Moreo, Phys. Rep. **344**, 1(2001).

[13] C. N. R.Rao and B.Raveau, Colossal Magneto Resistance, Charge Ordering and Related Properties of Manganese Oxides, (World Scientific, Singapore, 1998).

[14] A. Urushibara, Y. Moritomo, T. Arima, A. Asamitsu, G. Kido and Y. Tokura, Phys. Rev. B **51**, 14103 (1995).

[15] T. T. M. Palstra, A. P. Ramirez, S-W. Cheong, and B. R. Zegarski, P. Schiffer, J. Zaanen, Phys.Rev.B**56**, 5104 (1997).

[16] V.Sen, G.L. Bhalla , N.Panwar , W.K. Syu, N. Kaurav , Y.K. Kuo A. Rao, S.K. Agarwal, Physica B **405**, 1 (2010).

[17] G. J. Snyder, R. Hiskes, S. DiCarolis, M. R. Beasley, and T. H.Geballe, Phys. Rev. B **53**, 14434 (1996).

[18] R. K. Zheng, G. Li, A. N. Tang, Y. Yang, W. Wang, and X. G. Li,Z.D Wang and H.C.Ku Appl. Phys. Lett. **83**, 5250 (2003).

[19] X. G. Li, R. K. Zheng, G. Li, H. D. Zhou, R. X. Huang, J. Q. Xie, Z. D.Wang, Europhys. Lett.**60**, 670 (2002).

[20] S. Bhattacharya, A. Banerjee, S. Pal, R.K. Mukherjee, and B.K. Chaudhuri, J.Appl. Phys.**93**, 356 (2003).

[21] Q. Zhou, M. Dai, R. Wang, L.Jin, S. Zhu, L. Qian, Y. Wu, J.Feng, Physica B**391**, 206 (2007).

[22] E.Beyreuther, S.Grafstrom, L. M. Eng,C. Thiele and K. Dorr, Phys. Rev. B**73**, 155425 (2006).

[23] M.F. Sunding, K. Hadidi, S. Diplas, O.M. Løvvik, T.E. Norby, A.E. Gunnaes, J. Electron. Spectrosc.Relat.Phenom.**184**, 399 (2011).

[24] S.Kumar, and V.S. Raju, S. Bera, K. Vijaynandhini, and T.R.N. Kutty, Nucl. Instr. and Meth.in Phys. Res. B **237**, 623 (2005).

[25] J. Choi, J. Zhang, S.-H.Liou, P. A. Dowben and E. W. Plummer,Phys. Rev. B**59**, 13453 (1999).

[26] L. Wang and J. Gao, J. Appl.Phys, **105**, 07E514 (2009).

[27] A. Santoni, G. Speranza, M. R. Mancini, F. Padella, L. Petrucci and S. Casadio, J. Phys.: Condens.Matter **11**, 3387–3393 (1999).

[28] D. Hsu, A. Mani, C. H. Chuang, C. H. Chen, M.-T.Lin, and J. G. Lin, J. Appl. Phys. **105**, 07D505 (2009).

[29] S. K. Hasanain, W. H. Shah, M. J. Akhtar, and M. Nadeem, Phys. Rev. B **65**, 144442 (2002).

[30] T. Elovaara, H. Huhtinen, S. Majumdar and P. Paturi, J. Phys. Condens.Matter **24**, 216002 (2012).

[31] B. Garcı´a-Landa, J. M. De Teresa, and M. R. Ibarra,C. Ritter, R. Drost and M.R. Lees J. Appl. Phys., **83**, 7664 (1998).

[32] S. S. Rao and S. V. Bhat, J. Phys. Condens.Matter **22**, 116004 (2010).

[33] M. Svedberg, S. Majumdar, H. Huhtinen, P. Paturi and S. Granroth, J. Phys. Condens. Matter **23**, 386005 (2011).

[34] T. Tang, R.S. Huang and S.Y. Zhang, Solid State Commun.**147**, 190 (2008).

[35] P. Kumar, M. G. Krishna and A K Bhattacharya, Bull. Mater.Sci., **32**, 263 (2009).

[36] P. Kumar, Nanoscale Res.Lett.**5**, 1596 (2010).

[37] G. Iniama, P. Presa, J. M. Alonso, M. Multigner, B. I. Ita, R. C.Gil, M. L. R.González, A. Hernandoand J. M. G. Calbet, J. Appl. Phys. **116**, 113901 (2014).

[38] R. Mahendiran, S. K. Tiwary, A. K. Raychaudhuri, T. V. Ramakrishnan,R. Mahesh, N. Rangavittal, and C. N. R. Rao, Phys. Rev. B **53**, 3348(1996).

[39] R Mahendiran, S. K. Tiwary and A. K. Raychaudhuri,Solid State Commun.**98**,701 (1996).

[40] F. J. Blatt, D. J. Flood, V. A. Rowe, P. A. Schroeder, and J. E.Cox, Phys. Rev. Lett. **18**, 395 (1967).

[41] D.Huo, J. Sakurai, T.Kuwai, Y.Isikawa, Q. Lu,Phys. Rev. B**64**, 224405 (2001).

[42] D.K.C.MacDonald, W.B.Pearson, I.M Templeton, Proc.R.Soc. London Ser.A**266**, 161 (1962).

[43] A. Kjekshus, W.B. Pearson, Can. J. Phys. **40**, 98 (1962).

[44] K.H. Fischer, Z. Phys. B Con. Mat.**42**, 245 (1981).

[45] N. F. Mott and E. A. Davis, Electronics processes in non-crystalline materials, (Clarendon, Oxford, 1971).

[46] A. Banerjee, S. Pal, S. Bhattacharya, H. D. Yang, and B. K. Chaudhuri, Phys. Rev. B **64**, 104428 (2001).

Chapter 4

Size effect on the colossal thermoelectric power in charge ordered small bandwidth manganites based on Gd-Sr

Earlier we observed colossal thermoelectric power in charge ordered intermediate bandwidth manganite $La_{0.5}Ca_{0.5}MnO_3$ and was explained based on charge ordering and occurrence of spin glass states. With a view to extending such a study on small bandwidth Gd-Sr manganites, both unmilled and milled forms of $Gd_{1-x}Sr_xMnO_3$ (x =0.3, 0.5, and 0.6) samples were prepared. This chapter discusses the size effect on the contribution to thermoelectric properties from different scattering mechanisms. Charge ordered compositions, both milled and unmilled forms, exhibited colossal thermoelectric power. Compared to unmilled samples, thermoelectric power of charge ordered milled samples exhibit higher values. Emphasis is laid in studying the role of grain boundary and grain size on different scattering mechanisms responsible for colossal thermoelectric power in charge ordered manganites. The absolute value of thermoelectric power almost doubled in the case of milled samples and attained a maximum value of -69 mV/K at 42K, where a spin glass transition takes place. In order to explain the occurrence of transition at ~42K, Field cooling and Zero field cooling magnetic measurements were conducted.

The work discussed in this chapter has been reported in: ***Material Research Express 2, 055504 (2015)***

4.1 Introduction

Recent advances on thermoelectric materials points to nano structuring approach to enhance thermoelectric properties [1-3]. For good thermoelectricity, phonon scattering should be high, while electron scattering should be low. This can be achieved by reducing the average grain size comparable to or lower than the phonon mean free path while it should be greater than electron mean free path [4]. Since the grain size is greater than the mean free path of electrons, electrons are confined while phonons are not confined to move so that phonon scattering due to grain boundaries (GB) is larger. There are numerous reports on the improvement of power factor by introducing interface scattering of phonons by grain boundaries due to nano structuring [1, 5-6]. Besides phonon and electron scattering, electron - magnon scattering should also be considered while nano engineering interfaces. Such nano structuring influences the mobility of charge carriers and eventually permits tailoring of S, κ and σ.

When the grain size decreases to nanometric scales, the density of electronic states (DOS) is increased significantly due to quantum confinement [7]. In order to suppress lattice thermal conductivity and also to enhance GB - phonon scattering, low dimensional nano structuring techniques are required. Several researchers reported that with nano structuring, lattice thermal conductivity is reduced due to phonon scattering introduced at nano interfaces [8-11].

There are a large number of reports on the structural, magnetic and electrical properties of perovskite manganites based on lighter rare earths. However, investigations on small bandwidth manganites based on heavy rare earth are very rare in literature. They are potential materials with high Seebeck coefficient [12]. Small bandwidth manganites exhibit stable charge ordered (CO) state [13-15]. In CO, the ordering of Mn^{3+} and Mn^{4+} species

occurs over the lattice which leads to the coexistence of ferromagnetic clusters within an antiferromagnetic matrix.

Colossal thermoelectric power has been observed in our recent investigations carried out on charge ordered composition of intermediate bandwidth manganite $La_{0.5}Ca_{0.5}MnO_3$ [16]. As FM and AFM phases are of co-exist for charge ordered composition, strong competition between these magnetic phases arises a magnetically frustrated glass state, spin glass. Hence the mechanism leading to colossal thermoelectric power is based on the charge ordered spin-glasses. Several researchers reported unique electric and magnetic phenomena exhibited by charge ordered $Gd_{1-x}Sr_xMnO_3$ [17-18]. Garcia Landa *et al.* observed the coexistence of charge ordered insulator (COI) and cluster glass (CG) states for this compound to occur below 42 K [19].Though the thermoelectric power is appreciable, it was observed at low temperatures. From an application point of view, the magnetic transition temperature where the thermoelectric power peak coincides has to be enhanced.

The role of grain boundary and grain size on the thermoelectric properties of manganites is less studied. Since the contribution to thermoelectric power from different scattering phenomena such as magnon drag, phonon drag, charge ordering and spin glass strongly depends on grain size, it is valuable to study the grain size dependant transport properties in charge ordered $Gd_{1-x}Sr_xMnO_3$ (x =0.3, 0.5, and 0.6) samples. When the grain size of the material becomes comparable to or smaller than the mean free path of the phonon carriers, phonon scattering is increased significantly and hence affect thermoelectric properties. To investigate the effect of grain boundary and grain size on different scattering mechanisms responsible for colossal thermoelectric power in charge ordered manganites and to check whether nano structuring tunes the temperature exhibiting maximum

thermoelectric power, we carried out transport measurements on both the milled and unmilled form of charge ordered $Gd_{1-x}Sr_xMnO_3$, synthesized by solid state reaction method. To understand the nature and origin of charge ordered spin glasses, field cooled-zero field cooled (FC-ZFC) magnetization measurements were carried out. To confirm charge ordering, an exact estimation of the valence states of Mn is required. The valence state of manganese ions were examined by X-ray Photoelectron Spectroscopy (XPS).

4.2 Method of synthesis

Bulk samples of $Gd_{1-x}Sr_xMnO_3$ (x = 0.3, 0.5, 0.6), coded as GSMO3, GSMO5 and GSMO6, were prepared by a wet solid state reaction. Stoichiometric amounts of precursors, namely, Gd_2O_3, $SrCO_3$ and MnO_2 were mixed in concentrated nitric acid. The solution was heated and excess nitric acid was boiled off. They were then calcined in air at 900^0C for 12 hours. After pre sintering, the black powder were ground and pressed into pellets and sintered at 1200^0C in air for 72 hours. For preparing nano samples, bulk samples synthesized by solid state reactions were subjected to mechanical milling for 12 hours by high energy ball milling. These powders were cold pressed along with a Poly Vinyl Alcohol (binder) and heat treated at 250^0C for completely removing the binder.

4.3 Results and Discussions

4.3.1 Structural characterization

X-ray powder diffraction pattern of both unmilled and ball milled GSMO samples are shown in figures (4.1.a) and (4.1.b) respectively. The room temperature XRD pattern shows that the samples are single phasic and orthorhombic with a Pbnm space group in accordance with their respective bulk samples. This is in agreement with previous reports [19]. Broad XRD lines of milled powder with large Full Width at Half Maximum (FWHM)

indicate the formation of nano - crystalline powders. The difference between XRD pattern of both milled and unmilled samples is evidenced by the broadening of diffraction peaks induced by the reduced crystallite size and strain. The XRD data have been analysed by refining the experimental data using a standard Rietveld refinement technique using Full PROF program. The Rietveld refined XRD pattern of unmilled GSMO samples are shown in figure (4.2.a to 4.2.c). Representative Rietveld refined pattern of XRD of ball milled $Gd_{0.5}Sr_{0.5}MnO_3$ is shown in figure (4.2.d). The average grain sizes and cell parameters of both the unmilled and ball milled samples as determined by XRD are shown in table 4.1. Figure 4.3 shows the TEM of the ball milled $Gd_{0.5}Sr_{0.5}MnO_3$ powder. The average particle size obtained from TEM is around 20 nm.

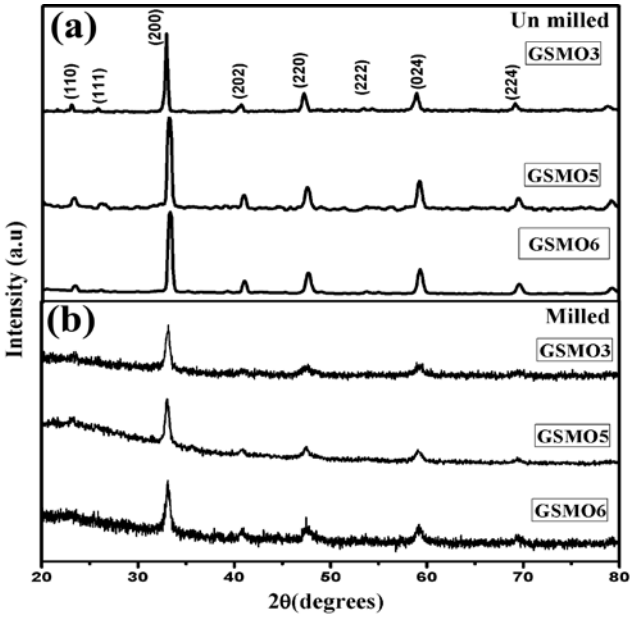

Figure 4.1: XRD pattern of (a) unmilled and (b) ball milled $Gd_{1-x}Sr_xMnO_3$ (x = 0.3, 0.5, 0.6).

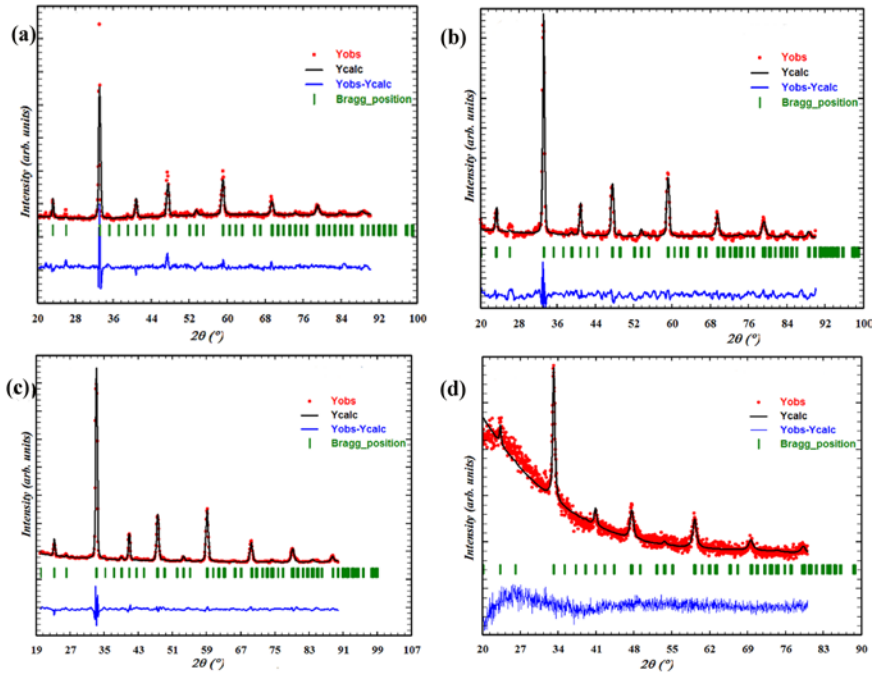

Figure 4.2: Rietveld refined XRD pattern of un milled (a) $Gd_{0.7}Sr_{0.3}MnO_3$ (b) $Gd_{0.5}Sr_{0.5}MnO_3$ (c) $Gd_{0.4}Sr_{0.6}MnO_3$ and (d) Representative Rietveld refined XRD pattern of ball milled $Gd_{0.5}Sr_{0.5}MnO_3$.

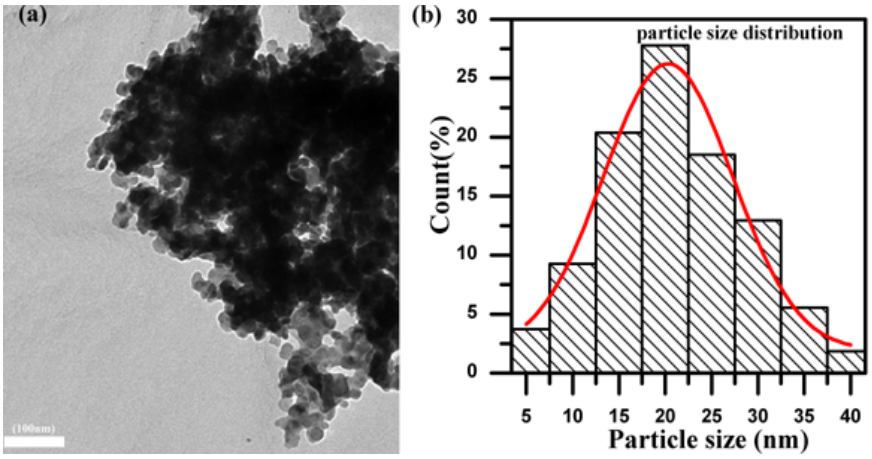

Figure 4.3: (a) TEM micrographs of ball milled $Gd_{0.5}Sr_{0.5}MnO_3$ and (b) shows particle size distribution.

Table 4.1. Structural parameters of GSMO unmilled and milled samples.

Sample	Unmilled /Milled	a Å	b Å	c Å	Crystallite size (nm)	Cell volume $(Å)^3$
GSMO3	Milled	5.399± 0.002	5.408± 0.002	7.671± 0.004	16.5	223.976 ±0.003
	Unmilled	5.41± 0.01	5.42± 0.02	7.69± 0.01	43	225.07± 0.01
GSMO5	Milled	5.394± 0.003	5.402± 0.003	7.668± 0.004	16.4	223.433 ±0.003
	Unmilled	5.395± 0.002	5.41± 0.02	7.68± 0.01	41	224.07± 0.01
GSMO6	Milled	5.35± 0.01	5.40± 0.01	7.65± 0.01	16.2	221.13± 0.01
	Unmilled	5.359± 0.001	5.407± 0.002	7.681± 0.003	34	222.565 ±0.002

4.3.2 Compositional analysis using XPS

As charge ordering owes its origin to the oxidation states of Mn, the mixed valence ratio of manganese (Mn^{4+}/Mn^{3+}) is a crucial factor in deciding the magnetic and transport properties. XPS measurements were performed on charge ordered manganite $Gd_{1-x}Sr_xMnO_3$ (x =0.3, 0.5, and 0.6). Figure 4.4 is a survey scan of unmilled $Gd_{0.5}Sr_{0.5}MnO_3$ sample plotted with photo electron intensity as a function of binding energy (in eV). Characteristic photo electron lines of Sr 3d, O1s, Gd 4d, and Mn 2p are visible in the recorded spectrum. For a thorough interpretation of the XPS data, a slow scan of the most intense peaks is recorded. The surface stoichiometry is also estimated from the XPS analysis and the ratio of Gd^{3+} and Sr^{2+} ions is found to be 1:1.

Figure 4.5 shows the detailed XPS spectrum of Sr 3d which contains a doublet where the line positions of Sr $3d_{5/2}$ and Sr $3d_{3/2}$ are respectively assigned to binding energies of 134.7eV and 132.9eV. The binding energies of Sr 3d are almost identical to previous studies [20]. The spin orbit splitting

between Sr $3d_{5/2}$ and Sr $3d_{3/2}$ components observed at about 1.8eV is also in good agreement with earlier results [20].

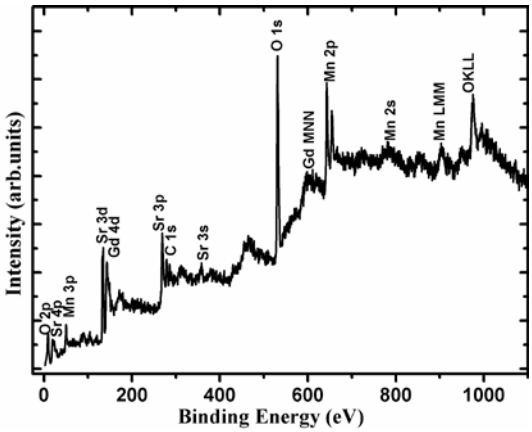

Figure 4.4: XPS survey scan of unmilled $Gd_{0.5}Sr_{0.5}MnO_3$

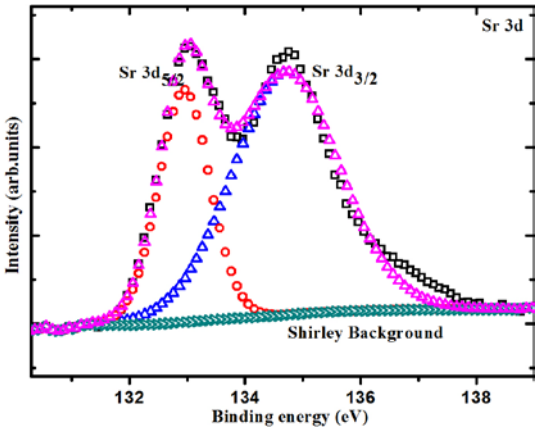

Figure 4.5: Sr 3d XPS spectrum

Peaks observed in the range of 138 eV – 150 eV is identified as peaks of doublets of Gd 4d: Gd $4d_{5/2}$ and Gd $4d_{3/2}$. Figure 4.6.a shows the resolved spectrum of Gd 4d doublet. The average binding energy is 141.4 eV for the Gd $4d_{5/2}$ transition and 146.3 eV for the Gd $4d_{3/2}$ transition. This doublet splitting of Gd as reported earlier for various Gd compounds such as oxides and halides are due to splitting of (Gd 4f) emission into two spin orbit components, Gd $4d_{5/2}$ and Gd $4d_{3/2}$ [21-22]. Doublet separation is observed

around 4.8 eV. An accurate interpretation of the oxygen peaks in manganites is rather difficult since the literature presents a lot of contradicting arguments [22-23]. With the best fit adopted, oxygen peaks corresponding to O1s can be resolved into two components as shown in figure 4.6.b. Two major peaks observed at 529.91±0.2eV and 531.89±0.2eV applies to the earlier results on manganites system and attributed to the bonding of oxygen ions with Gd and Mn ions [24-25].

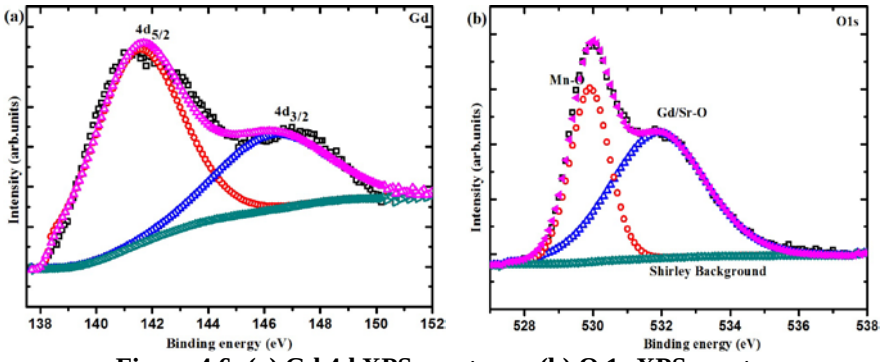

Figure 4.6: (a) Gd 4d XPS spectrum (b) O 1s XPS spectrum

Manganese peak analysis is the central part of XPS analysis in manganites. Evidence for mixed valence states of manganese in perovskite manganites is derived from the curve fitting results of Mn $2p_{3/2}$ spectra shown in figure 4.7. $Mn2p_{3/2}$ peaks are resolved into two, one at 641.1eV and the other at 642.54 eV. From literature, it is observed that Mn^{2+} peaks are assigned to lower binding energy than Mn^{3+} and Mn^{4+} and also Mn^{3+} peaks are observed at 641.7 eV [24,26-29]. Hence in the present study the high binding energy component located at 642.54 eV corresponds to Mn^{4+} while the lower one located at 641.1 eV corresponds to Mn^{3+}. These values are close to the reference values of 641.3 eV and 642.8 eV of $Mn2p_{3/2}$ in $La_{2/3}Sr_{1/3}MnO_3$ composites [30]. Average concentration of Mn^{3+} obtained by analysing Mn 2p doublet structure is found to be 48.8% and that of Mn^{4+} is 51.2%. Hence the mixed valence manganese ratio of Mn^{4+}/Mn^{3+} is ~ 1.04. Thus, both, Mn^{3+} and Mn^{4+} have almost the same concentration which

suggests that the composition of $Gd_{0.5}Sr_{0.5}MnO_3$ is charge ordered. Similarly for GSMO3 and GSMO6, Mn^{4+}/Mn^{3+} ratio is determined by XPS and the results are summarized in table 4.2. $Mn2p_{3/2}$ XPS spectrum of unmilled $Gd_{0.7}Sr_{0.3}MnO_3$ and $Gd_{0.4}Sr_{0.6}MnO_3$ is shown in figure 4.8.

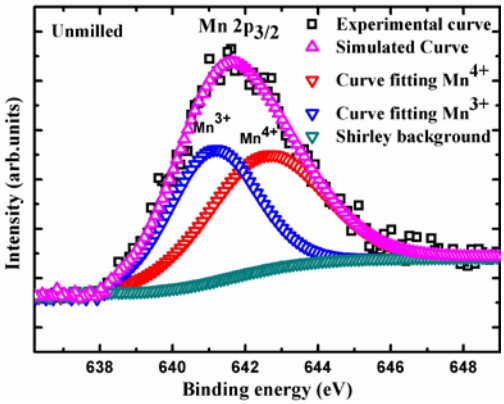

Figure 4.7: $Mn2p_{3/2}$ XPS spectrum of unmilled $Gd_{0.5}Sr_{0.5}MnO_3$

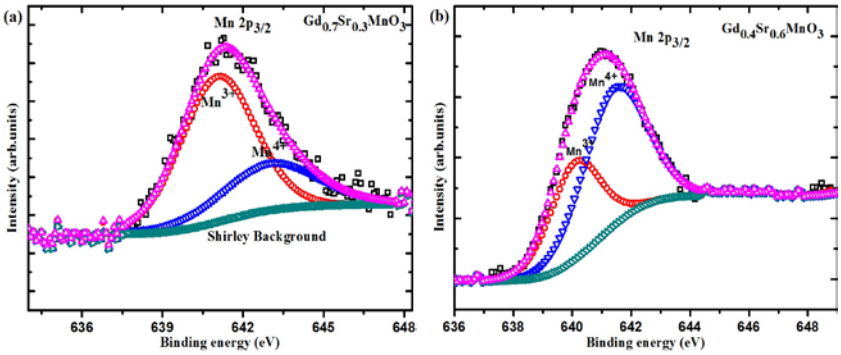

Figure 4.8: $Mn2p_{3/2}$ XPS spectrum of unmilled (a) $Gd_{0.7}Sr_{0.3}MnO_3$ and (b) $Gd_{0.4}Sr_{0.6}MnO_3$

Table 4.2. Stoichiometry of GSMO bulk samples.

Sample	Mn^{4+}/Mn^{3+}	
	Calculated	Measured
$Gd_{0.7}Sr_{0.3}MnO_3$	0.428	0.415
$Gd_{0.5}Sr_{0.5}MnO_3$	1	1.04
$Gd_{0.4}Sr_{0.6}MnO_3$	1.5	1.56

Composition analysis of ball milled $Gd_{0.5}Sr_{0.5}MnO_3$ samples using XPS shown in figure 4.9 points to the fact that Mn^{4+}/Mn^{3+} is ~1.05. This also indicates the existence of charge ordered phase after milling.

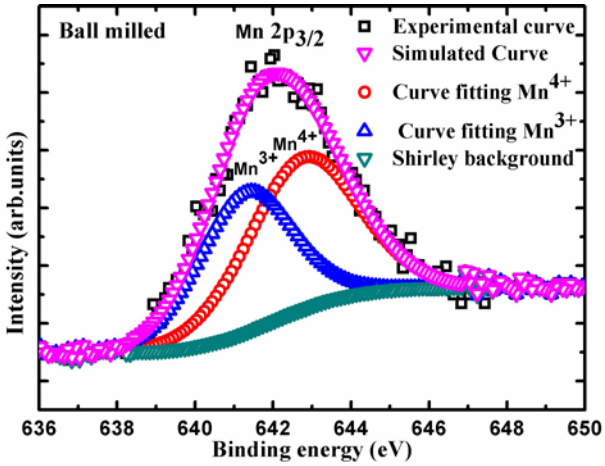

Figure 4.9: $Mn2p_{3/2}$ XPS spectrum of ball milled $Gd_{0.5}Sr_{0.5}MnO_3$.

4.3.3 Transport properties (Thermoelectric Power, Resistivity and Magnetic) of unmilled and milled GSMO samples

The variation of thermoelectric power with respect to temperature of unmilled and ball milled GSMO samples are shown in figures 4.10.a and 4.11.a respectively with the inset indicating resistivity variation with respect to temperature. The variation of resistivity for both unmilled and ball milled samples resembles that of a semiconductor in the measured temperature range. The resistivity exhibits an upturn at ~ 90K. This sudden increase in resistivity below 90K is similar to that observed for mixed valence compounds undergoing charge ordering [16, 19, 31-32]. Earlier Garcia Landa *et al*. have observed similar increase in resistivity below 90K in $Gd_{0.5}Sr_{0.5}MnO_3$ and reported that a charge ordering take place around 90K [19]. Hence resistivity upturn at around 90K can be attributed to the charge ordering in GSMO samples. Usually for charge ordered small bandwidth manganites, metal to insulator transition is not that obvious as its resistivity

is high [33, 19]. Earlier reports on magneto resistance of $Gd_{0.5}Sr_{0.5}MnO_3$ samples showed that a very high magnetic field is required to induce the metal to insulator transition [19]. For low bandwidth manganites, the charge ordering range extends to a wide range of doping (x = 0.3-0.7) [13-14].

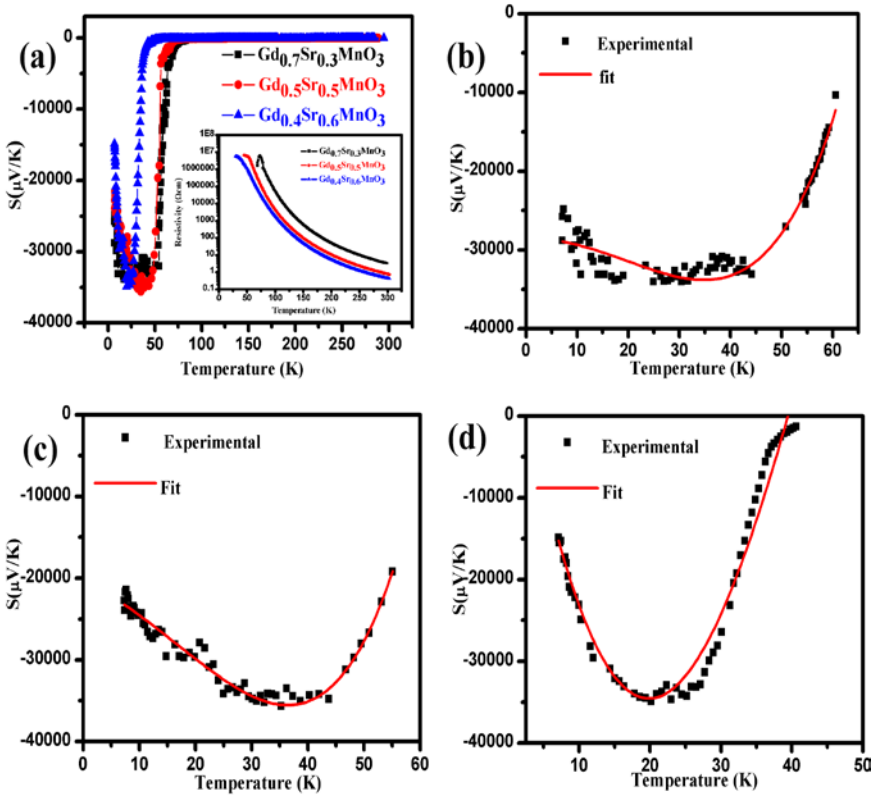

Figure 4.10: Temperature dependence of thermoelectric power of unmilled $Gd_{1-x}Sr_x\ MnO_3$ (x= 0.3, 0.5, 0.6) (a) from 5K to 300 K and its inset shows the resistivity as a function of temperature. Variations of S with T in the CO spin glass region for (b) $Gd_{0.7}Sr_{0.3}MnO_3$, (c) $Gd_{0.5}Sr_{0.5}MnO_3$ and (d) $Gd_{0.4}Sr_{0.6}MnO_3$. The solid line gives the best fit to equation (4.1).

The temperature variation of thermoelectric power showed that as temperature decreases, Seebeck coefficient exhibits a slight increase up to CO state temperature. When the temperature reaches the CO temperature ~ 90K of $Gd_{0.5}Sr_{0.5}MnO_3$, there is a dramatic increase of negative value of thermoelectric power and also a colossal peak value of about -36mV/K was

observed at 38K. After attaining this peak value, thermoelectric power decreases with temperature. For the other two compositions 0.3 and 0.6, colossal peak values are respectively -33mV/K and -35mV/K. Negative thermoelectric power throughout the whole temperature region indicates the presence of electrons as charge carriers.

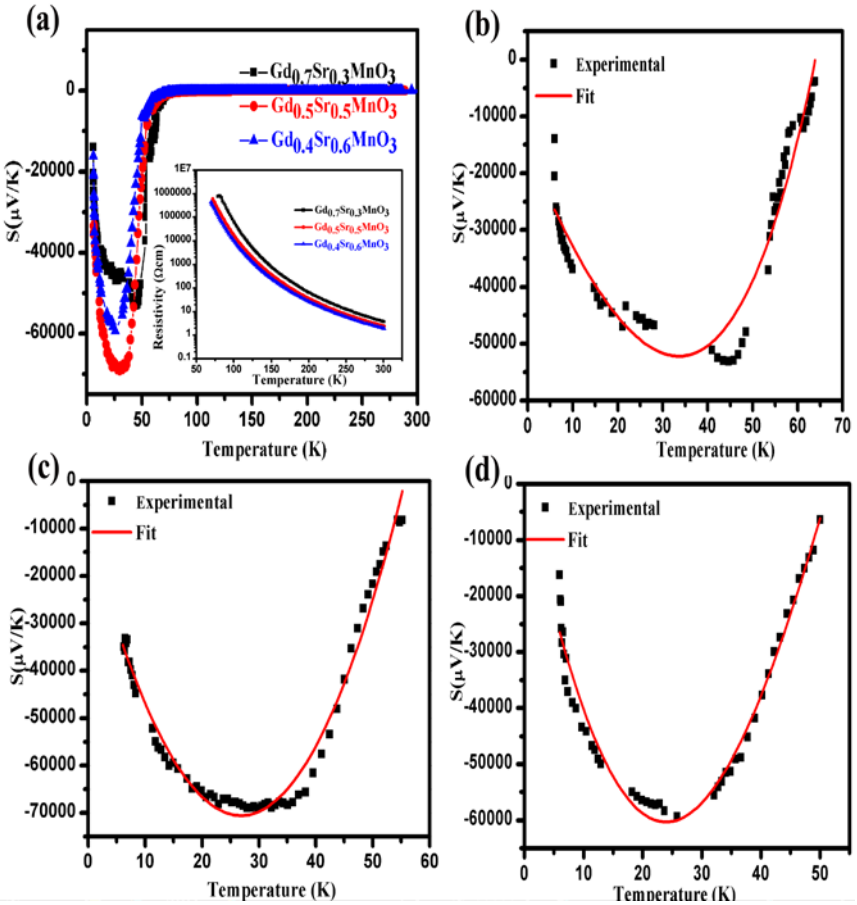

Figure 4.11: Temperature dependence of thermoelectric power of ball milled $Gd_{1-x}Sr_x\ MnO_3$ (x= 0.3, 0.5, 0.6) (a) from 5K to 300 K and its inset shows the resistivity as a function of temperature. Variation of S with T in the CO spin glass region (T<50K) for (b) $Gd_{0.7}Sr_{0.3}MnO_3$, (c) $Gd_{0.5}Sr_{0.5}MnO_3$ and (d) $Gd_{0.4}Sr_{0.6}MnO_3$. The solid line gives the best fit to equation (4.1).

For nano sized ball milled samples, resistivity is even higher and is beyond the measuring range below a particular temperature. Here also the

temperature dependent thermoelectric power shows a dramatic increase of negative value when the temperature attains its CO temperature of ~ 90K and reaches a colossal peak value of about -69 mV/K at 42K.

The most important region of thermoelectric power variation for these charge ordered compositions in both milled and unmilled form is in the regime $T<T_{CO}$, where the system enters into charge ordered state. In the earlier reports of Garcia Landa *et. al*, it has been mentioned that $Gd_{0.5}Sr_{0.5}MnO_3$ shows a spin glass transition near 42K [19]. In the present case, temperature dependent thermoelectric power exhibits a colossal peak value at this temperature. Thus in this specific region, the charge ordered state is expected to be coexisting with a spin - glass state. So to prove this and to propose an exact mechanism for the observed colossal thermoelectric power, magnetization studies have been carried out.

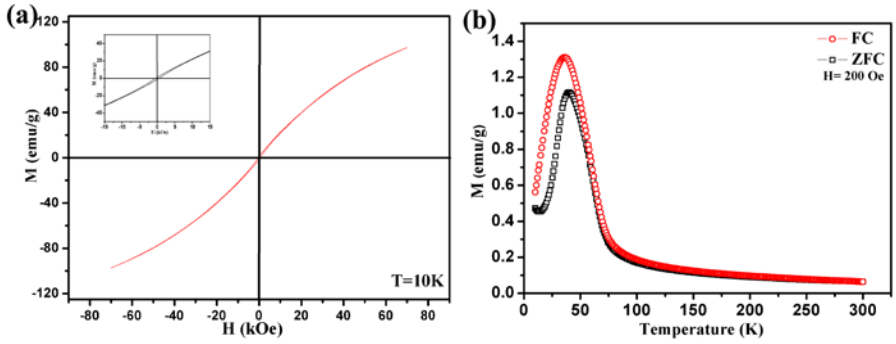

Figure 4.12: (a) M-H loops of un milled $Gd_{0.5}Sr_{0.5}MnO_3$ at 10K. The inset shows an enlarged view of M-H at 10K (b) Magnetization measurements under ZFC and FC conditions in a magnetic field of 200 Oe.

Magnetization as a function of applied field at 10K of unmilled $Gd_{0.5}Sr_{0.5}MnO_3$ sample is shown in figure 4.12.a. At 10K, with increasing field, the magnetization increases but does not saturate, even on an application of a fairly high magnetic field of 80 kOe. However the sample shows a minor hysteresis around zero field. This type of hysteresis loop behaviour is typical of short range ordered spin glass like states, where one encounters competing ferromagnetic and antiferromagnetic interactions.

There are several reports with respect to this type of magnetic behaviour exhibited by charge ordered manganites [13,15,34].The temperature dependent ZFC and FC magnetization measurements were also conducted to correlate the existence of charge ordering to spin glass in GSMO which is presumed to be responsible for the colossal thermoelectric power in the region below T_{CO}.

Temperature dependent magnetization studies under an applied field of 200 Oe of unmilled $Gd_{0.5}Sr_{0.5}MnO_3$ is shown in figure 4.12.b. Strong competition between FM phase and AFM phase results in the formation of a frustrated state at around 42K. Irreversibility is observed below 90K. Irreversibility and anomalies below 90K are purported to be the onset of charge ordering below this temperature [19]. The results indicate that a frustrated magnetic phase has nucleated below T_{CO} due to the co-existence of COAFM and FM phases at very low temperatures. It must be mentioned here that Prodi *et al.* carried out structural studies at low temperatures and found that charge ordering is responsible for the structural transformation [32, 35]. In our investigations we have procured additional proof from XPS studies for charge ordering apart from temperature dependent resistivity as well as magnetic measurements. Detailed analysis of magnetic characteristics in unmilled GSMO samples will be discussed in chapter 6.

Magnetic reversal and spin glass transition were exhibited by unmilled form of GSMO samples when cooled under a field very much lower than the coercive field. Magnetic reversal is due to the antiferromagnetic interaction of Gd sub lattice with Mn sub lattice. Earlier Snyder *et al.* also found a similar type of magnetic reversal in calcium substituted $GdMnO_3$ [36]. Spin glass transition was also observed in bulk form of $Gd_{1-x}Sr_xMnO_3$ (x = 0.3, 0.5, 0.6) at around ~ 40K. Hence in the regime $T<T_{CO}$, charge ordering co exists with glass transition at

temperatures, where the thermoelectric power also shows a peak in its temperature dependency.

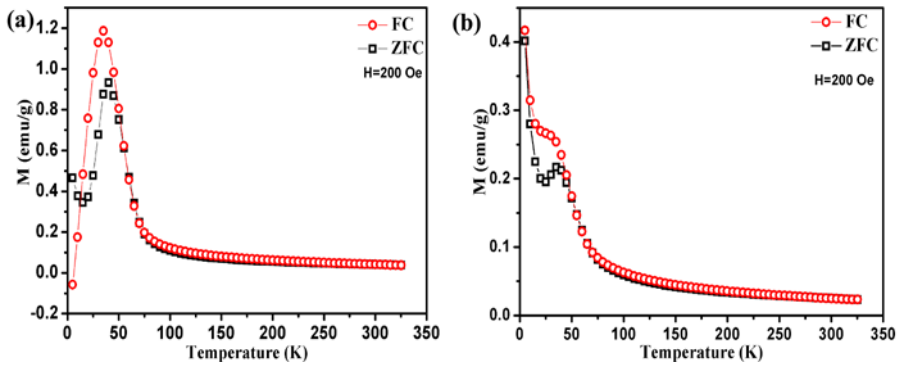

Figure 4.13: Magnetization measurements under ZFC and FC conditions in a magnetic field of 200 Oe for ball milled (a) $Gd_{0.7}Sr_{0.3}MnO_3$ and (b) $Gd_{0.4}Sr_{0.6}MnO_3$.

Temperature dependent magnetization studies of ball milled $Gd_{0.7}Sr_{0.3}MnO_3$ and $Gd_{0.4}Sr_{0.6}MnO_3$ in an applied field of 200 Oe under field cooling (FC) and zero field cooling (ZFC) protocol is shown in figures 4.13.a and 4.13.b respectively. Similar to bulk, FC- ZFC magnetization of ball milled GSMO samples can be described as a ferrimagnetic like system of two interacting magnetic sub lattices. The spin-glass like behaviour due to coexistence of FM – AFM and ferrimagnetic interaction introduced by Gd substitution suggests an AFM exchange coupling between Gd^{3+} and Mn^{3+}/Mn^{4+} sub lattice. Similar to bulk, a magnetic ordering was observed at very low temperatures ~ 42K for milled GSMO samples. But the observed transition temperature at which magnetic ordering occurs are found to be slightly higher for the ball milled samples than that for the unmilled $Gd_{1-x}Sr_xMnO_3$ manganites. For example, the magnetic ordering temperature in the unmilled GSMO6 sample takes place at 30K which is shifted to 36K in case of milled GSMO6 samples. The thermoelectric transition temperatures in case of milled samples are also slightly shifted to higher temperature side.

For explaining colossal thermoelectric power observed near glass transition temperature (T<50K), a Kondo term, S_2T^2, as pointed out by Fischer to explain Kondo properties of spin glass is incorporated with magnon scattering proposed by Mandal [37- 38]. Thus in the low temperature region (T<50K) we have analyzed the TEP data by using the expression

$$S = S_0 + S_{3/2}T^{3/2} + S_2T^2 + S_4T^4 \qquad (4.1)$$

The details of the equations used for fitting were described in the previous chapter. To analyse TEP data in the remaining charge ordered region 50K<T<T_{CO}, instead of spin glass contribution, a phonon drag term is included in Mandal's model [38]. Fitting of TEP in the remaining CO regime is done using the following equation

$$S = S_0 + S_{3/2}T^{3/2} + S_3T^3 + S_4T^4 \qquad (4.2)$$

Seebeck coefficient in the high temperature region due to polarons in both unmilled and milled samples is confirmed by Motts' equation in transport mechanism.

$$S = \frac{k_B}{e}\left[\frac{E_S}{k_BT} + \alpha'\right] \qquad (4.3)$$

Hence the whole thermoelectric power variation was analysed by dividing the entire temperature range into three regions namely (i) T<50K, (ii) 50K<T<T_{CO} and (iii) T>T_{CO}.

The experimental data of both unmilled and ball milled form of $Gd_{0.7}Sr_{0.3}MnO_3$, $Gd_{0.5}Sr_{0.5}MnO_3$ and $Gd_{0.4}Sr_{0.6}MnO_3$ samples fitted according to equation (4.2) and the fitted curves for region T<50K are respectively shown in figures (4.10.b, 4. 10. c, 4. 10.d) and (4.11.b, 4.11.c, 4.11.d). TEP in the remaining CO region of both bulk and nano form of GSMO3, GSMO5 and GSMO6 fitted to equation corresponding to 50K<T<T_{CO} are respectively shown in figures (4.14.a, 4.14.b and 4.14.c)

and (4.15.a, 4.15.b and 4.15.c). Thus by both glassy and CO AFM phases, charge carriers are localized at the sites and exhibits colossal thermoelectric power. In the region T<50K, in addition to magnon contribution, the fitting coefficient corresponding to the spin glass also increases with increasing strontium content. Hence the TEP in the low temperature is not only having charge ordered magnon contribution but also have that of charge ordered spin glass.

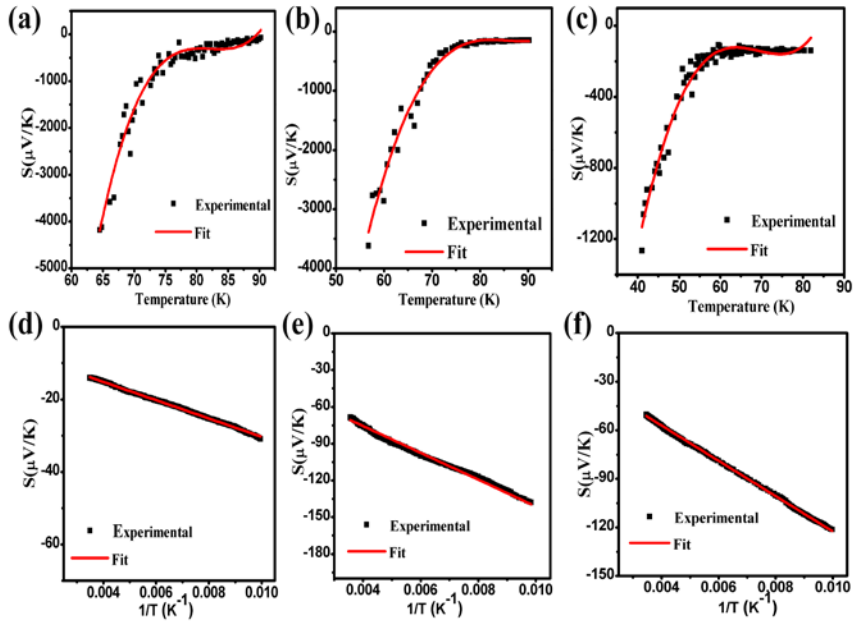

Figure 4.14: Variation of S with T at 50K<T<T_{CO} of unmilled (a) $Gd_{0.7}Sr_{0.3}MnO_3$, (b) $Gd_{0.5}Sr_{0.5}MnO_3$ and (c) $Gd_{0.4}Sr_{0.6}MnO_3$. Variation of S with1/ T (T>T_{CO}) of unmilled (d) $Gd_{0.7}Sr_{0.3}MnO_3$, (e) $Gd_{0.5}Sr_{0.5}MnO_3$ and (f) $Gd_{0.4}Sr_{0.6}MnO_3$. The solid line is a best fit to equations (4.2) and (4.3).

The fitting parameters corresponding to the region 50K<T<T_{CO} points out that besides magnon drag produced by electron-magnon interaction; a T^3 dependence of S due to phonon drag produced by electron-phonon interaction is also significant in this region. The best fit parameters of the experimental TEP data for unmilled and milled $Gd_{1-x}Sr_xMnO_3$ in the entire CO region are shown in table 4.3 and 4.4 respectively.

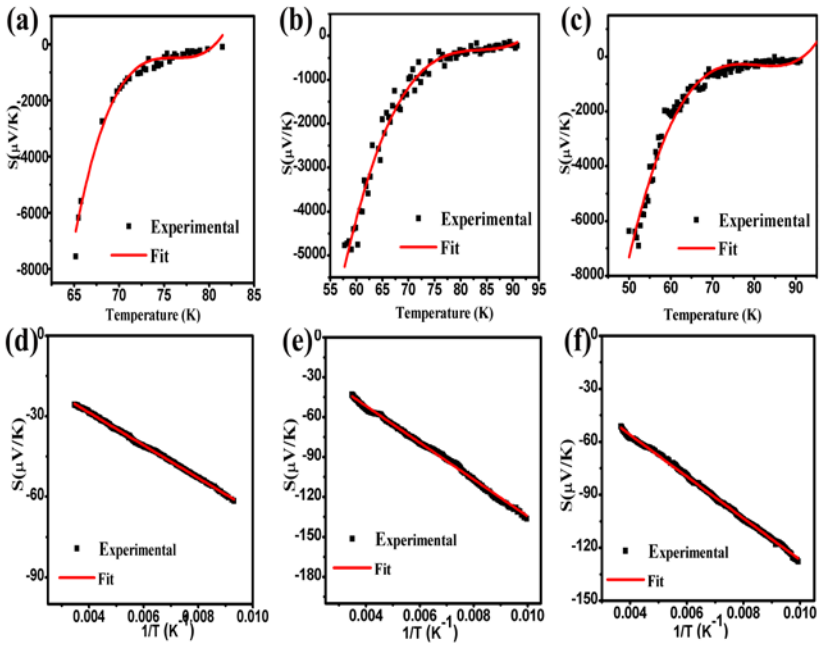

Figure 4.15: Variation of S with T at 50K<T<T_{CO} of ball milled (a) $Gd_{0.7}Sr_{0.3}MnO_3$, (b) $Gd_{0.5}Sr_{0.5}MnO_3$ and (c) $Gd_{0.4}Sr_{0.6}MnO_3$. Variation of S with1/ T (T>T_{CO}) of ball milled (d) $Gd_{0.7}Sr_{0.3}MnO_3$, (e) $Gd_{0.5}Sr_{0.5}MnO_3$ and (f) $Gd_{0.4}Sr_{0.6}MnO_3$. The solid line is a best fit to equations (4.2) and (4.3).

Table 4.3. The best fit parameters of the experimental TEP data for unmilled $Gd_{1-x}Sr_x$ MnO_3 (x= 0.3, 0.5, 0.6) measured in the temperature range T<50K and 50K<T<T_{CO}.

Sample Code	Temperature region	S_0 ($\mu V/K$)	$S_{3/2}$ ($\mu V/K^{5/2}$)	S_2 ($\mu V/K^3$)	S_3 ($\mu V/K^4$)	S_4 ($\mu V/K^5$)
GSMO3	T<50K	-28428.7	11.53	-8.38	NC	0.003
	50K<T<T_{CO}	-22585.4	5497.1	NC	-0.82	0.0045
GSMO5	T<50K	-20202.9	353.26	-8.5	NC	0.005
	50K<T<T_{CO}	-53009.3	1239.5	NC	-0.169	0.001
GSMO6	T<50K	-13608.2	5007.2	-134	NC	0.01
	50K<T<T_{CO}	-10345.1	299.9	NC	-0.064	0.0005

Table 4.4. The best fit parameters of the experimental TEP data for milled $Gd_{1-x}Sr_x MnO_3$ (x= 0.3, 0.5, 0.6) measured in the temperature range T<50K and 50K<T<T_{CO}.

Sample Code	Temperature region	S_0 ($\mu V/K$)	$S_{3/2}$ ($\mu V/K^{5/2}$)	S_2 ($\mu V/K^3$)	S_3 ($\mu V/K^4$)	S_4 ($\mu V/K^5$)
GSMO3	T<50K	-15495.3	1962.3	-22.6	NC	0.0029
	50K<T<T_{CO}	-80068.4	29271.7	NC	-5.05	0.033
GSMO5	T<50K	-10375.5	4472.9	-82.9	NC	0.00025
	50K<T<T_{CO}	-95627.5	2270.5	NC	-0.32	0.0019
GSMO6	T<50K	-816.62	5256.1	-116	NC	0.005
	50K<T<T_{CO}	-82623.5	2054.19	NC	-0.32	0.0019

It is found that for T<T_{CO} excluding spin glass region, the magnon drag is maximum in both bulk and nano for the optimum composition x = 0.3. This is because double exchange mechanism is maximum for this composition. While for spin glass region, due to glassy nature, both magnon drag and spin glass contribution is found to be increasing with increasing Sr content. As per earlier reports on thermoelectric power of nano samples the huge thermoelectric power exhibited by nano samples can be due to the scattering of phonons [4]. From table 4.3 and 4.4 it is evident that phonon scattering in the case of milled samples is 80% more than that of unmilled samples. Besides phonon scattering, both magnon scattering and also spin glass contribution in milled samples is found to be higher than their corresponding unmilled counterparts. This is because, when the grain size is reduced the grain surface region is enhanced compared to core of the grain. At the grain surface, due to the presence of large number of defects, the spins

will be randomly oriented. Hence the effect of spin glass will be predominant.

The activation energy for conduction obtained from thermoelectric power data in the high temperature region and α, proportionality factor determining small polaron hopping mechanism found out for both unmilled and ball milled samples from Mott's equation [39] are tabulated in table 4.5. At a temperature greater than $T_{CO,}$ it is seen from figures 4.14.d-4.14.f and 4.15.d-4.15.f that Seebeck coefficient of both unmilled and milled samples decreases with increasing temperature and attains a constant value after a particular temperature. This temperature independent behavior is typical of small polaron conduction. The value of $\alpha' < 1$ indicates the presence of small polaron carriers in the high temperature region. Thus the high thermoelectric power exhibited in the high temperature region is due to the contribution of small polaron.

Table 4.5. The activation energy and α', proportionality factor, of both unmilled and milled form of $Gd_{1-x}Sr_x MnO_3$ (x= 0.3, 0.5, 0.6) obtained from Mott's equation.

Sample	unmilled/milled	E_s (meV)	α'
GSMO3	**unmilled**	**3.1**	**-0.07**
	milled	**6.3**	**-0.04**
GSMO5	**unmilled**	**11.1**	**-0.36**
	milled	**14.7**	**-0.04**
GSMO6	**unmilled**	**10.1**	**-0.15**
	milled	**11.8**	**-0.10**

Since the grain size of milled sample is small, resistivity is higher and hence activation energy required for hopping of small polarons is relatively higher when compared to unmilled ones. In the case of unmilled samples, due to large grain size, grain to grain contact area is more and

therefore the barrier height for the hopping of small polarons is lower. Earlier Buch *et. al* reported that with increasing grain size, activation energy decreases due to lowering of barrier height by increasing grain to grain contact area [40]. With decreasing grain size the interconnectivity between grains decreases which disturbs the easy hopping of e_g electrons between neighbouring sites.

The Strontium content, x, dependence on colossal thermoelectric power value and transition temperature exhibiting the colossal value of both unmilled and ball milled samples are shown in figures (4.16.a) and (4.16.b). When compared to unmilled sample, the value of thermoelectric power of milled one is found to be twice. Besides thermoelectric power, resistivity is higher and also the transition peaks showing maximum thermoelectric power are found to be slightly shifted to higher temperature side. In ball milled samples, grain size is reduced, hence grain boundary is high, and then higher thermal energy is required to overcome the activation energy. Hence the transitions are shifted to higher values.

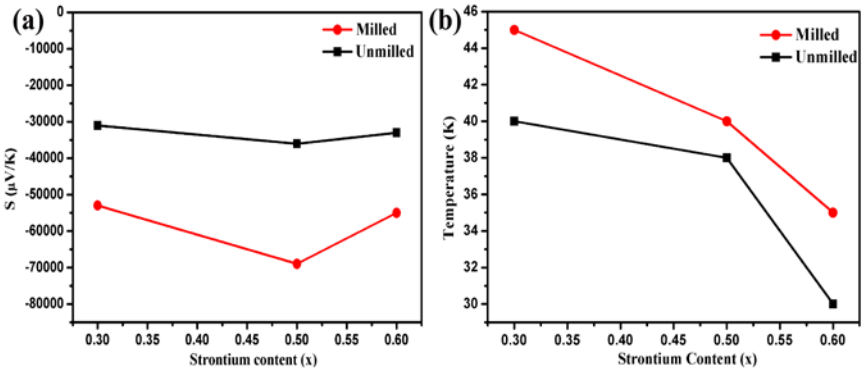

Figure 4.16: Variation of (a) colossal thermoelectric power value and (b) transition temperature exhibiting the colossal value of both unmilled and ball milled $Gd_{1-x}Sr_x MnO_3$ with respect to Sr substitution.

With decreasing grain size, the grain boundary region of individual grains increases and thereby enhance grain boundary scattering. Room

temperature thermoelectric power of both milled and unmilled samples are shown in figure (4.17). The signature of grain size effect can also be seen from the room temperature thermoelectric power data. This can be due to the grain boundary effect. This indicates that the grain size has significant dependence on thermoelectric power characteristics even at room temperature.

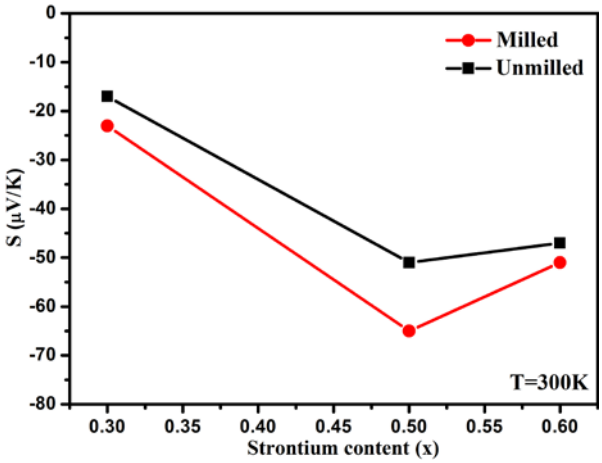

Figure 4.17: Variation of thermoelectric power with respect to Sr content of unmilled and ball milled $Gd_{1-x}Sr_x MnO_3$ samples at room temperature.

4.4 Conclusions

Single phase charge ordered low bandwidth manganites belonging to series $Gd_{1-x}Sr_xMnO_3$ (x = 0.3, 0.5and 0.6) were prepared using solid state reactions. A colossal thermoelectric power was observed. To study grain size effect on the contribution to thermoelectric properties from different scattering mechanisms, these samples are milled by high energy ball milling. Both the surface composition and the optimal Mn^{4+}- Mn^{3+} concentration in charge ordered milled and unmilled GSMO samples were examined by XPS. The colossal thermoelectric power obtained at the low temperature for both unmilled and milled samples was explained based on charge ordered spin glass state. The samples having smaller grain size show increased

thermoelectric power over the samples having larger grain size. This can be due to the increased phonon scattering.

References

[1] J-F. Li, W-S.Liu, L-D. Zhao and M. Zhou, NPG Asia Mater. **2(4)**, 152 (2010).

[2] J.Zheng, Front. Phys. China.**3**, 269 (2008).

[3] J. Snyder and E. S. Toberer, Nat.Mater.**7**, 105 (2008).

[4] K. Koumoto, Y. Wang, R. Zhang, A. Kosuga and R. Funahashi, Annu.Rev. Mater. Res.**40**, 363 (2010).

[5] Y. Lan, A. Jerome Minnich, G.Chen, and Z. Ren, Adv. Funct. Mater. **20**, 357 (2010).

[6] T. M. Tritt and M.A. Subramanian, MRS Bull. **31**,188 (2006).

[7] L. D. Hicks , M. S. Dresselhaus, Phys. Rev. B **47**, 12727 (1993).

[8] M. Takashiri, T. Borca-Tasciuc, A. Jacquot, K. Miyazaki, and G. Chen, J. Appl. Phys. **100**, 054315 (2006).

[9] D. M. Rowe and V. S. Shukla, J. Appl. Phys. **52**, 7421 (1981).

[10] K. Watari, K. Hirano, M. Toriyama, and K. Ishizaki, J. Am. Ceram. Soc. **82**, 777 (1999).

[11] N. Savvides and H. J. Goldsmid, J. Phys. C Solid St. Phys. **13**, 4657 (1980).

[12] S. Sagar, V. Ganesan, P. A. Joy, Senoy Thomas, A. Liebig, M. Albrecht and M. R. Anantharaman, Europhys. Lett. **91**, 17008 (2010).

[13] E. Dagotto, T. Hotta and A. Moreo, Phys. Rep. **344**, 1 (2001).

[14] Z Jirak, S Krupicka, Z Simsa, M Dlouha and S Vratislav J. Magn.Magn.Mater. **53**,153 (1985).

[15] M. Svedberg, S. Majumdar, H. Huhtinen, P. Paturi and S. Granroth, J. Phys. Condens. Matter **23**, 386005 (2011).

[16] Lija K. Joy, S.Shanmukharao Samatham, Senoy Thomas, V. Ganesan, Salim Al – Harthi, A. Liebig, M. Albrecht, and M. R. Anantharaman J. Appl. Phys. **116**, 213701, (2014).

[17] A. A. Wagh, P. S. Anil Kumar, H. L. Bhat and Suja Elizabeth J. Phys.: Condens. Matter **22**, 026005 (2010).

[18] A. A. Wagh, P. S. Anil Kumar, H. L. Bhat and Suja Elizabeth J Supercond Nov Magn **24**, 665 (2011).

[19] B. Garcia-Landa, J. M. De Teresa, M. R. Ibarra, C. Ritter, R. Drost and M. R. Lees, J. Appl. Phys., **83**, 7664 (1998).

[20] S. W. Han, J. D. Lee, K. H. Kim, H. Song, W. J. Kim and S. J. Kwon, H. G. Lee and C. Hwang, J. I. Jeong and J.-S. Kang, Journal of the Korean Physical Society, **40,** 501-510 (2002).

[21] K. Wandelt and C.R. Brundle, Surface Science **157**, 162-182 (1985).

[22] J.-J. Liang and H.-S. Weng, Ind. Eng. Chem. Res. **32**, 2563-2572 (1993).

[23] S. Ponce, M. A. Peña, and J. L. G. Fierro, Appl. Catal., B **24**, 193 (2000).

[24] A. Santoni, G. Speranza, M. R. Mancini, F. Padella, L. Petrucci and S. Casadio, *J*. Phys. Condens.Matter **11**, 3387–3393 (1999).

[25] J. Choi, J. Zhang, S.-H.Liou, P. A. Dowben and E. W. Plummer, Phys. Rev. B**59**, 13453 (1999).

[26] W-Y. Howng and R. Thorn, J. Chem. Phys. Lett, **56**, 463 (1978).

[27] P. Wang, L. Yao, M. Wang and W. Wu, J. Alloys Compd, **311**, 53 (2000).

[28] S. Mickevicius, V. Bondarenka, S. Grebinskij, A.K. Oginskis, R. Butkute, H. Tvardauskas, B. Vengalis , B.A. Orlowski, V. Osinniy, M. Pietrzyk and W. Drube, Acta Phys. Pol., A **113** 1071(2008).

[29] L. Wang and J. Gao, J. Appl.Phys, **105**, 07E514 (2009).

[30] Q. Zhou, M. Dai, R. Wang, L. Jin, S. Zhu, L. Qian, Y.Wu and J. Feng, Physica B **391**, 206 (2007).

[31] E. J. Verway Nature **144,** 327 (1939).

[32] A. Prodi, E. Gilioli, A. Gauzzi, F. Licci, M. Marezio, F. Bolzoni, Q. Huang, A. Santoro and J. W. Lynn, *Nat. Mater.* **3**, 48 (2004).

[33] J. M. D. Coey, M. Viret and S. von Molnair, Adv.Phys. **48**, 167 (1999).

[34] T Tang, R S Huang and S Y Zhang, Solid State Commun.**147**, 190 (2008).

[35] A Prodi, A Daoud-Aladine , F Gozzo, B Schmitt, O Lebedev, G van Tendeloo, E Gilioli, F Bolzoni, H Aruga-Katori, H Takagi, M Marezio and A Gauzzi, *Phys. Rev.* B **90**,180101(R) (2014).

[36] G J Snyder, C H Booth, F Bridges, R Hiskes, S DiCarolis, M R Beasley and T H Geballe, Phys.Rev. B **55**, 6453 (1997).

[37] K.H. Fischer, Z. Phys. B Con. Mat.**42**, 245 (1981).

[38] P. Mandal, Phys. Rev. B **61**, 14675 (2000).

[39] N. F. Mott and E. A. Davis, Electronics Process in Non-Crystalline Materials, Clarendon, Oxford (1971).

[40] J.J.U.Buch, T.K.Pathak, V.K.Lakshmi, N.H.Vasoya and K.B.Modi, J.Phys.D:Appl.Phys.**40**, 5306 (2007).

Chapter 5

Magneto-electric transport properties of half doped wide bandwidth manganites ($La_{0.5}Sr_{0.5}MnO_3$)

This chapter discusses the conduction mechanism in $La_{0.5}Sr_{0.5}MnO_3$ manganites by analysing the data on the dependence of temperature on electrical resistivity, magnetization and thermoelectric power. The data have fitted to suit various models. The correspondence between the variation of thermoelectric power and magnetoresistance (MR) with temperature has been established.

5.1 Introduction

In the preceding chapters we have discussed the various physical properties of low and medium bandwidth manganites namely GSMO and LCMO, in that, GSMO falls under the family of small bandwidth manganites and LCMO belongs to the class of intermediate bandwidth manganites. Our investigations have found a close correlation between magnetism and thermoelectric power, especially, at low temperatures.

A striking feature of the above investigation is that they display charge ordering wherein the concentration of Mn^{3+}/Mn^{4+} is almost unity. However, none of the compositions investigated and described in earlier chapters were pure ferromagnets. We have seen that the transport data can be fitted with modified versions of various models. For instance, the thermoelectric transport in GSMO and LCMO was fitted with a modified Mandal model where Fischer's spin glass term, $S_2 T^2$ is incorporated. Mott's polaronic model was found suitable for fitting the high temperature data in the case of GSMO/LCMO samples [1-4].

Substitution of divalent cations at trivalent rare earth sites in $REMnO_3$ results in the replacement of Mn^{3+} by Mn^{4+} which gives rise to mixed-valence manganites with a general formula of the form $RE_{1-x}AE_xMnO_3$ [Where RE is the rare earth element, AE is the divalent cation]. $La_{1-x}Sr_xMnO_3$ is a prototypical double exchange ferromagnet in a range of x concentration ($0.1<x<0.6$) and is a wide bandwidth manganite where the enhanced bandwidth is largely due to the strong overlapping of atomic orbitals. It may be noted that the bandwidth is the width of conduction band formed by the hybridization of manganese e_g level and oxygen p level [5-6]. As bandwidth increases, magnitude of hopping amplitude for e_g electrons is also increase, which is favourable for double exchange and hence exhibits

ferromagnetic behaviour. Their Curie temperature T_C and metal to insulator transition temperature are relatively high.

In these class of compounds, valence electrons are more delocalized and are conducive for double exchange phenomenon [7]. From the phase diagram of $La_{1-x}Sr_xMnO_3$ [8-10], it is seen that LSMO has a ferromagnetic metallic ground state at half doping. Though the ratio of Mn^{3+}/Mn^{4+} is ideally suited for charge ordering, in practice, they are not. The interplay of delocalization and conduction under an externally applied magnetic field and their transport properties are interesting from a fundamental perspective. $La_{0.5}Sr_{0.5}MnO_3$ (coded as LSMO5) is an ideal template for validating various models namely, small polaron hopping model, Zener double exchange polynomial law for explaining conduction process. This is a unique system which is ferromagnetic in nature and the possibility of spin polarised tunnelling exist at low temperature.

LSMO5 is ferromagnetic due to double exchange. There can be a possibility of existence of spin polarised tunnelling at low temperature and having appreciable thermoelectric power. Also there exists close correlation between thermoelectric power and magnetoresistance with respect to temperature. Fitting the thermoelectric power and resistivity data in various temperature regions with appropriate models can reveal the exact mechanisms behind the conduction in this half doped manganites. At the metal to insulator boundary of this half doped manganites, there could be a tendency to form coexisting clusters of FM-AFM phases. With this motivation in mind, $La_{0.5}Sr_{0.5}MnO_3$ was prepared and a thorough investigation on its thermoelectric power, resistivity and magnetization was carried out.

5.2Method of synthesis

$La_{0.5}Sr_{0.5}MnO_3$ sample was prepared by citrate gel technique. Stoichiometric amounts of La_2O_3, $SrCO_3$ and MnO_2 were mixed in dilute nitric acid and suitable amounts of ethylene glycol and citric acid were added. Then the solution was heated to 80^{o}C. After a few hours the solution gets boiled, frothed, turned dark, ignited and caught fire to give a spongy powder. The resulting black powder was calcined in air at 900^{o}C for 12 hours and then pressed into pellets of cylindrical discs with diameter 12 mm and thickness 2 mm. The pellets were then sintered at 1050^{o}C for 12 hours.

5.3 Results and Discussions

5.3.1 Structural studies using XRD

The crystal structure of the sample was determined using X-ray diffraction. The X-ray powder diffraction pattern of LSMO5 is shown in figure 5.1.a.

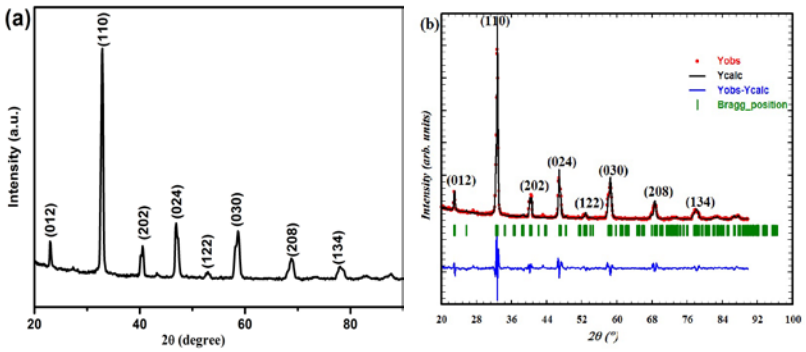

Figure 5.1: (a) XRD pattern for $La_{0.5}Sr_{0.5}MnO_3$. (b) Rietveld refinement performed on $La_{0.5}Sr_{0.5}MnO_3$.

From the diffraction pattern, it is evident that $La_{0.5}Sr_{0.5}MnO_3$ is single phasic with orthorhombically distorted perovskite structure belonging to the space group R3c. The average particle size estimated from XRD data using Scherrer's formula is 25nm. The XRD data have been analysed by refining the experimental data using a standard Rietveld refinement technique.

Refined lattice parameters determined at room temperature are a = 5.455 Å, b = 5.524 Å, c = 7.714 Å which are consistent with earlier reports [11-13]. The Rietveld refined pattern of XRD is also shown in figure 5.1.b.

5.3.2 Electrical and magnetoresistive properties

Resistivity measurements by usual standard four probe techniques in the temperature range of 5K- 300K for different magnetic fields are shown in figure 5.2. A giant MR can be noticed from the figure. The external field when applied aligns the spins favourably thereby reducing the scattering of charge carriers during hopping which results in the decrease of resistivity.

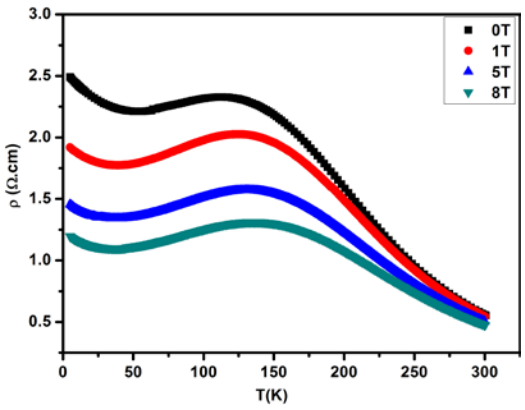

Figure 5.2: Temperature dependence of resistivity measured under 0T, 1T, 5T, and 8T magnetic fields.

The metal to insulator transition temperature T_{im} is taken as the maxima of dρ/dT versus temperature curve which is found to be 120 K at 0T. When the temperature is further lowered from T_{im}, a second transition is observed at T<50 K with a broad resistive minimum in the temperature range of 30 K-40 K. Hence the sample exists in three different states at different temperatures. To explore different scattering mechanisms involved, we analysed resistivity data by dividing the entire temperature range (5 K-300 K) into three different temperature regimes : (i) temperature above T_{im} ($T>T_{im}$), (ii) metallic regime $50K<T<T_{im}$ and (iii) low temperature weak metallic regime T<50K.

5.3.2.1 Conduction mechanism in insulating region ($T>T_{im}$)

Above T_{im}, the semi covalent bond between Mn-O-Mn becomes covalent and the Jahn - Teller distortion is prominent so that the charge carriers are trapped which gives rise to polarons [14-16]. Hence above T_{im}, the resistivity shows a polaronic like behaviour. This can be explained by small polaron hopping model equation,

$$\rho = AT\, e^{E_A/KT}, \qquad (5.1)$$

where T is absolute temperature, E_A is activation energy and A is constant [17-21]. The graph between log (ρ/T) and 1/T shown in figure (5.3) is a straight line. This straight line indicates that the exact conduction mechanism in the temperature regime $T>T_{im}$ for this particular composition is due to polarons.

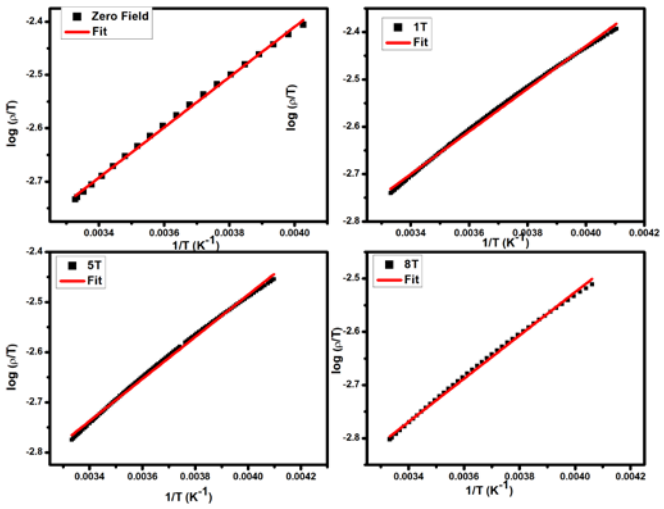

Figure 5.3: Plots of log (ρ/T) vs 1/T for $La_{0.5}Sr_{0.5}MnO_3$ under 0T, 1T, 5T, and 8T magnetic fields.

5.3.2.2 Conduction mechanism at metallic region ($50K<T<T_{im}$)

In the metallic region, thermal frustration of spins rises with increasing temperature and hence the increasing resistivity. The conduction in metallic ferromagnetic region ($50K<T<T_{im}$) is assumed to be due to electron magnon

interaction in double exchange and hence resistivity data are well fitted according to Zener double exchange polynomial law.

$$\rho = \rho_0 + \rho_2 T^2 + \rho_{4.5} T^{4.5} \qquad (5.2)$$

where ρ_0 is temperature independent resistivity term due to domain and grain boundary, $\rho_2 T^2$ due to electron-electron scattering and the last term $\rho_{4.5} T^{4.5}$ is due to electron magnon scattering in the double exchange theory [21]. The fitted parameters are shown in table 5.1. From the fitted values it is found that the value for magnon scattering term $\rho_{4.5} T^{4.5}$ decreases with applied field suggesting the suppression of magnetic fluctuations with the applied magnetic field. Significant decrease in value of ρ_0 with applied field indicates the influence of magnetic field on the magnetic domains where the size of domain boundary reduces with increasing field and there by diminishing ρ_0. Also the shift in the transition temperature T_{im} to high temperature with the application of fields indicates the growth of FM region by suppressing the formation of polarons and spin disorder scattering. Temperature dependent resistivity data in the temperature range $50K<T<T_{im}$ with varying fields fitted to equation (5.2) are shown in figure (5.4).

Table 5.1: Fitted parameters in the temperature variation of resistivity according to the equation (5.2).

Field	ρ_0 *(Ω cm)*	ρ_2 *(Ω cm /K²)*	$\rho_{4.5}$ *(Ω cm /K^4.5)*
Zero	**2.12**	**2.76E-5**	**-8.50E-11**
1T	**1.68**	**3.86E-5**	**-8.40E-11**
5T	**1.27**	**3.19E-5**	**-7.06E-11**
8T	**1.04**	**2.63E-5**	**-5.34E-11**

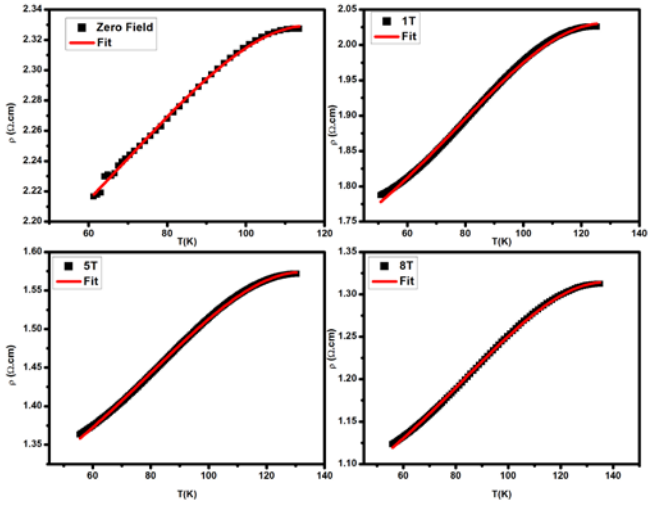

Figure 5.4: Temperature versus resistivity plots of $La_{0.5}Sr_{0.5}MnO_3$ under zero field, 1T, 5T, and 8T field applied in the temperature range 45K<T< T_{im}. The solid line gives the best fit to equation (5.2).

5.3.2.3 Conduction mechanism at weak metallic region (T<50K)

A distinct resistive minimum is observed in the zero field resistivity data in the temperature range of 30-40 K. In zero field, at very low temperature, the neighbouring grains are aligned randomly so that the charge carriers in them have opposite spins. Hence there exists an energy gap between the charge carriers of the neighbouring antiferromagnetically coupled grains. As temperature increases they get enough thermal energy so as to jump the barrier. Thus the resistivity is decreased with increasing temperature. When the temperature corresponding to the minimum resistivity is reached, it superposes the metallic onset resistivity and follows a metallic behaviour. The observed resistive minimum in the zero field resistivity data is not so profound when external fields are applied. This can be due to the inter grain transport phenomenon [16]. When external fields are applied, the adjacent grains are aligned favourably so that the energy gap reduces as a result of which the resistivity minimum reduces with increasing applied field [22].

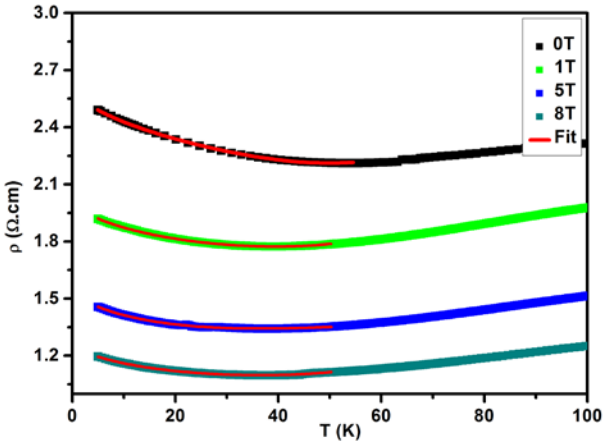

Figure 5.5: Temperature versus resistivity plots of $La_{0.5}Sr_{0.5}MnO_3$ under zero field, 1T, 5T, and 8T field applied in the temperature range T<45K. The solid line gives the best fit to equation (5.3).

Kalyana lakshmi *et. al* have explained the distinct low temperature minimum observed in the electrical resistivity data of $La_{1-x}Na_xMnO_3$ by introducing the effect of weak localization in addition to electron-electron and electron magnon scattering in the resistivity equation (5.2) [23]. Earlier Zhang *et. al* has explained this kind of upturn of resistivity in bilayer manganite $La_{1.2}Sr_{1.8}Mn_2O_7$ by incorporating $T^{1/2}$ term (term corresponding to weak localization) in the conventional resistivity equation of ferromagnetic phase [24]. Later Y.S. Reddy *et. al* also showed that the low temperature upturn of resistivity is directly proportional to weak localization term, $T^{1/2}$ [25]. By introducing a $T^{1/2}$ term in the resistivity equation of ferromagnetic phase, the low temperature minimum observed in the resistivity data is successfully fitted to equation (5.3).

$$\rho = \rho_0 + \rho_{1/2}T^{1/2} + \rho_2 T^2 + \rho_{4.5}T^{4.5} \qquad (5.3)$$

Square root temperature dependence of resistivity indicates the appearance of a weak non metallic behaviour for T< 50K in zero field and from the fitted parameters, this dependence is found to be decreasing with

the application of a magnetic field. It can be due to decrease in magnetic domain boundary with the application of magnetic field.

Table 5.2: Fitted parameters in the temperature variation of resistivity according to the equation (5.3).

Field	ρ_0 *(Ω cm)*	$\rho_{1/2}$ *(Ω cm /K$^{1/2}$)*	ρ_2 *(Ω cm /K^2)*	$\rho_{4.5}$ *(Ω cm /K$^{4.5}$)*
Zero	**2.64**	**-0.07**	**4.17E-6**	**-1.31E-9**
1T	**2.04**	**-0.054**	**4.16E-5**	**-5.95E-10**
5T	**1.58**	**-0.053**	**7.30E-5**	**-6.75E-10**
8T	**1.28**	**-0.04**	**4.02E-5**	**-3.17E-10**

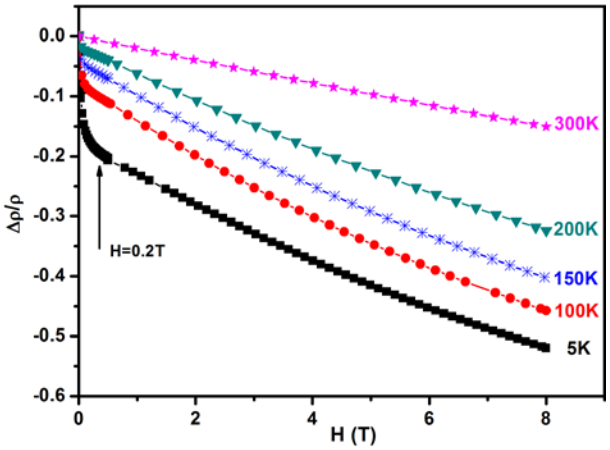

Figure 5.6: Variation of MR with applied magnetic field at different temperatures.

The variation of MR with magnetic field at different temperatures is shown in figure (5.6). From the figure (5.6), it is clear that a kink can be seen near 0.2T in low temperatures, especially, at 5K. Above and below this field, MR varies linearly with magnetic field. This indicates the co-existence of

ferromagnetism with another phase which is weakly conducting [26]. In the region below this kink (H<0.2T), MR has contributions from spin polarized inter grain tunnelling while ferromagnetic contributions are more prevalent in the region above the kink (H>0.2T). The magnetic field corresponding to this kink is termed as Low Field Magneto Resistance (LFMR). Hwang *et al.* has reported that this LFMR in polycrystalline materials is due to the spin polarised transport across the grain boundaries [27]. Absence of such a kink in MR variation with field at high temperature indicates that this spin polarised tunnelling is absent at higher temperatures. As temperature increases, thermal energy increases and thus antiferromagnetically aligned grains acquire sufficient energy to overcome the barrier. Spin tunnelling is not present in the high temperature region where it behaves metallic. Also the Low Field Magneto Resistance in 5K is close to 1/3, which is the universal value of all ferromagnetic manganites.

To separate out the contribution of MR from spin polarized transport, a phenomenological model suggested by Raychaudhari *et.al* was used to analyse experimental MR data [28]. The contribution of inter grain tunnelling in the low temperature can be observed directly from the fitting of magnetic field dependence of $\Delta\rho/\rho$ to the relation

$$MR = -A\int_0^H f(k)dk - JH - KH^3 \qquad (5.4),$$

where $f(k)$ gives the contribution from spin polarised tunnelling which is expressed as

$$f(k) = A\exp(-Bk^2) + Ck^2\exp(-Dk^2) \qquad (5.5)$$

Where A, B, C, D, J and K are adjustable fitting parameters. To fit equation (5.4), we have followed the same method as used by Raychaudhari *et. al* [28]. The experimental MR data and simulated curves using equation (5.4) at

various temperatures are shown in figure (5.7). To fit equation (5.4) to these curves, equation (5.4) is differentiated with respect to H and substituting equation (5.5) in equation (5.4) we get,

$$d(MR)/dH = A\exp(-BH^2) + CH^2\exp(-DH^2) - JH - KH^3 \quad (5.6)$$

The experimental curves were differentiated and fitted to equation (5.6) to find the best fit parameters. Figure (5.8.a) shows the differentiated curve and best fit function at 5K and figure (5.8.b) shows the experimental MR-H curve at 5K along with simulated curves using equation (5.4). It is found that there is an excellent fit for all temperatures up to 300 K where the spin polarized tunnelling contribution is absent. Hence the MR due to spin polarised tunnelling drops rapidly with temperature. Thus the low temperature minimum observed can be due to both spin polarised tunnelling and weak localization effect.

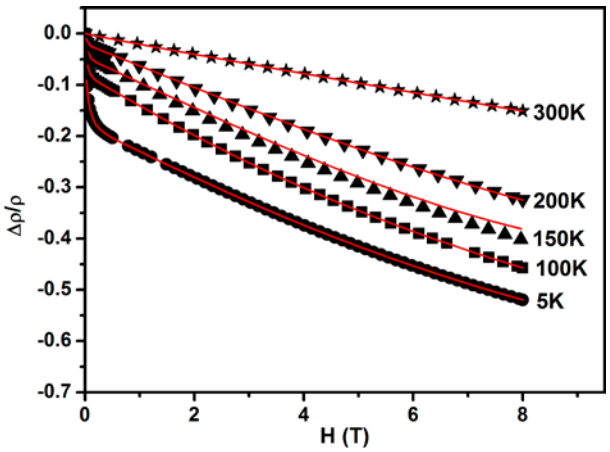

Figure 5.7: The experimental MR-H curves (dots) and the fitted curves (lines) using equation (5.4) at various temperatures.

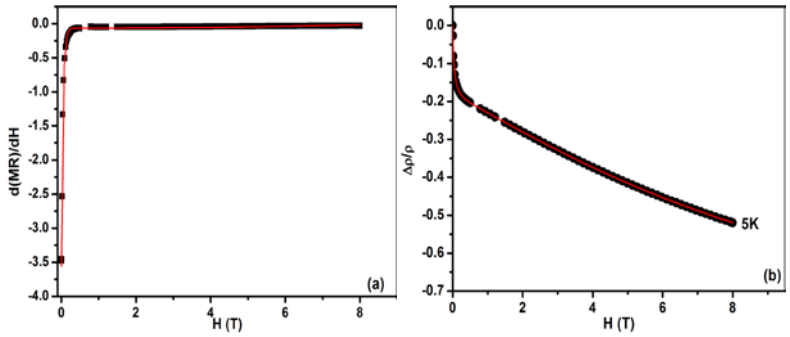

Figure 5.8: (a) The differentiated curve and best fit function at 5K with A=-3.486, B=35.16,C=-0.0125, D=6.12, J= 0.47x $10^{-2}$and K=-0.23x10^{-6} (b) The experimental MR-H curves (dots) and the fitted curves (lines) using equation (5.4) at 5K .

The variation of magnetoresistance with temperature for an applied field of 8T is shown in figure (5.9). A maximum MR percentage of about 64% at around 50K was observed. Two slope changes are seen in MR variation with temperature. This can be explained on the basis of two different mechanisms such as intrinsic and extrinsic [23]. Slope change observed near ferromagnetic non metallic transition can be explained on the basis of an extrinsic inter grain effect. As grain size is very small, large grain boundaries are present. Hence in the presence of field, probability of spin polarisation through inter grain tunnelling is high thereby increasing MR percentage in this region. The other slope change is observed near T_{im} which can be explained on the basis of intrinsic grain effect. In manganites, especially for nano sized ones, there are ferromagnetic metallic regions and antiferromagnetic insulating regions. As temperature increases from T_{im}, volume fraction of the AFM insulating region increases, which enhances spin fluctuations within the volume of grains. Hence near T_{im} when external fields are applied these fluctuations are suppressed so that the electron suffers less scattering by local spins. Thus the sharp drop of MR near T_{im} is due to this intrinsic grain effect.

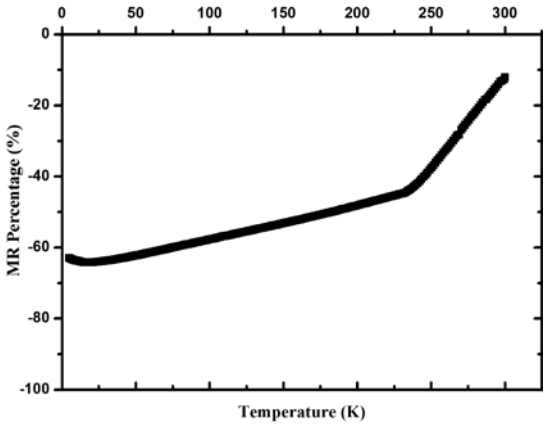

Figure 5.9: Variation of percentage of MR with temperature using a magnetic field of 8T

5.3.3 Magnetization studies

Temperature dependent zero field cooling (ZFC) and field cooling (FC) magnetization measured in different applied magnetic fields of 25, 50 and 200 Oe is shown in figure (5.10). A sharp paramagnetic to ferromagnetic transition is observed at T_C~320K. The transition temperature is taken as the maximum of dM/dT versus temperature curves. This transition is due to the double exchange between neighbouring Mn^{3+} and Mn^{4+} through oxygen, which causes the hopping of electrons from half - filled e_g orbital of Mn^{3+} to empty e_g orbital of Mn^{4+} via $2p_\sigma$ orbital of oxygen. However the transition region is relatively wide and also ZFC magnetisation is found to be decreasing at very low temperatures. Earlier Wang *et.al* explained the wide transition observed in $La_{0.5}Sr_{0.5}MnO_3$ nanoparticle compact by the weaker magnetic exchange coupling near the grain boundary with respect to that of intra grain [29]. As LSMO5 has equal number of Mn^{3+} and Mn^{4+}, the antiferromagnetic (AFM) Mn^{3+}-O-Mn^{3+} interactions tend to compete with ferromagnetic (FM) Mn^{3+}-O-Mn^{4+} interactions resulting in the evolution of magnetic frustration.

ZFC and FC magnetizations as a function of temperature in magnetic fields of 50 Oe, and 25 Oe are shown in figures (5.10.b) and

(5.10.c). It is observed that irreversibility between FC and ZFC is more significant for an applied field of 25 Oe. When the field is higher, FC and ZFC components come closer to each other and hence irreversibility decreases. Also the transition temperatures with applied field are shifted to lower temperatures. This shift in transition and thermo magnetic irreversibility is the most important characteristic of spin clusters which can be due to competing magnetic interactions [30]. Thus the thermo magnetic irreversibility below T_C as well as the magnetization drop can be due to the formation of cluster glass state [31].

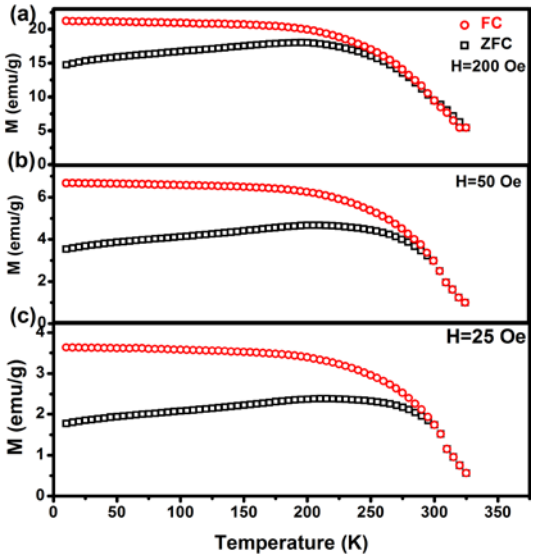

Figure 5.10: Magnetization measurements under ZFC and FC conditions in a magnetic field of (a) 200 Oe, (b) 50 Oe and (c) 25 Oe.

The M-H loops of $La_{0.5}Sr_{0.5}MnO_3$ measured at 5K and 300K are represented in figure (5.11). The magnetization at 5 K shows a hysteresis with unsaturated magnetic moment of 69emu/g at 70 kOe. M H at 300K shows linear increase of magnetization which is attributed to the co-existence of FM clusters in the AFM matrix. The increase in magnetization is due to the dominant behaviour of FM component in the system. The

absence of saturation magnetization is in accordance with the existence of antiferromagnetic order. In the MR studies, it is realized that the existence of two linear variations with respect to LFMR indicates the coexistence of FM-AFM phases. This co-existence of FM-AFM phases were further confirmed from magnetization studies.

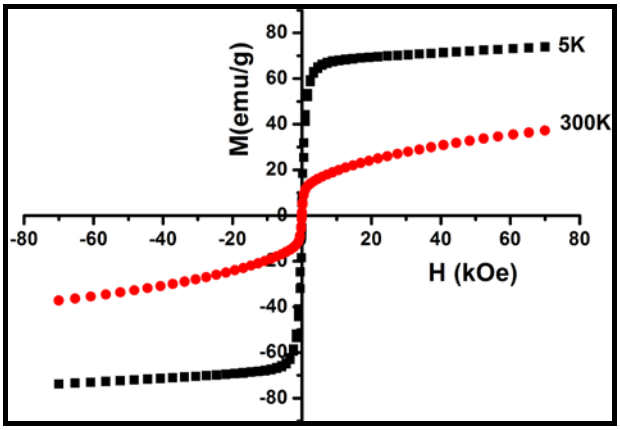

Figure 5.11: Magnetic hysteresis loops of $La_{0.5}Sr_{0.5}MnO_3$ measured at 5 K and 300 K

5.3.4 Thermoelectric power studies

The variation of thermoelectric power with temperature in the temperature range of 5K-300K is shown in figure (5.12). It is found that the value of thermoelectric power changes from positive to negative with increasing temperature. This change of sign in the thermoelectric power, S may be attributed to the orbital degeneracy of the e_g band [32]. Earlier Asamitsu *et al* has explained that this sign change in the thermo power is due to orbital degree of freedom of the e_g carriers [33]. *S* changes its sign from negative to positive with the increase of the spin polarization. From MR, it is found that spin polarised transport is present. The presence of spin polarised transport indicates that the degree of spin polarisation is high [28]. The spin degree of freedom is lost due to the full spin polarization of the e_g electrons and hence that only the orbital degree of freedom survives in the

ferromagnetic ground state. The positive S at low temperature is accredited to the holes which are excited from valence band to the impurity band. At high temperatures, electrons in the valence band are excited into the conduction band. As these electrons have high mobility within the conduction band, S is negative. Thus coexistence of two types of charge carriers is confirmed.

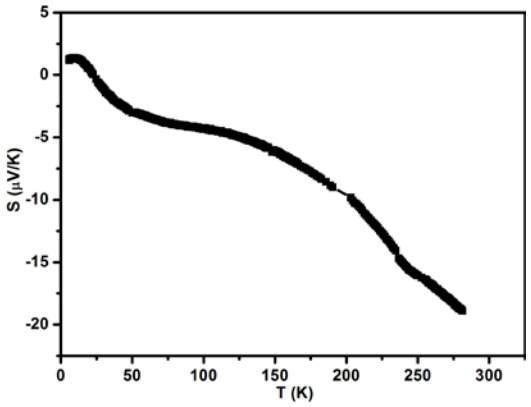

Figure 5.12: Temperature dependence of thermoelectric power from 5 K – 300 K.

In S versus T plot, two peaks are observed, one at the high temperature region (~T_{im}) and the other at the low temperature region (10-30K). Existence of peak at the high temperature region is generally common in all manganites which corresponds to metal to insulator transition. Prior reports showed that phonon drag and magnon drag contributions are present in the low temperature region [34]. Thus the low temperature peak found in the ferromagnetic metallic part may be due to the effect of electron – magnon interaction and electron - phonon interaction. Considering this phonon drag and magnon drag, the more general equation for the thermoelectric power is [23, 34 -35]:

$$S = S_0 + S_{3/2}T^{3/2} + S_3T^3 + S_4T^4 \qquad (5.7)$$

Where S_0 is a constant which accounts the low temperature variation of thermoelectric power, $S_{3/2}T^{3/2}$ is attributed to the magnon drag contribution, S_3T^3 and S_4T^4 are respectively accredited to the phonon drag and spin wave contribution.

From the section 5.3.2.3, the low temperature resistivity data fitting need a $T^{1/2}$ term (corresponds to weak localization effect). Hence we incorporate the contribution of thermoelectric power from a $T^{1/2}$ term. Besides this, K.H Fischer's Kondo term, S_2T^2 corresponding to magnetically frustrated state and a term, S_1T, with opposite sign which lead to a change of sign of TEP at a characteristic temperature are additionally needed for fitting [1]. Hence these contributions are also considered in the conventional equation (5.7) so as to make it suitable to account the entire metallic part of thermoelectric power.

Similar to the electrical resistivity, the equation of thermoelectric power data is modified as:

$$S = S_0 + S_{1/2}T^{1/2} + S_1T + S_{3/2}T^{3/2} + S_2T^2 + S_3T^3 + S_4T^4 \quad (5.8)$$

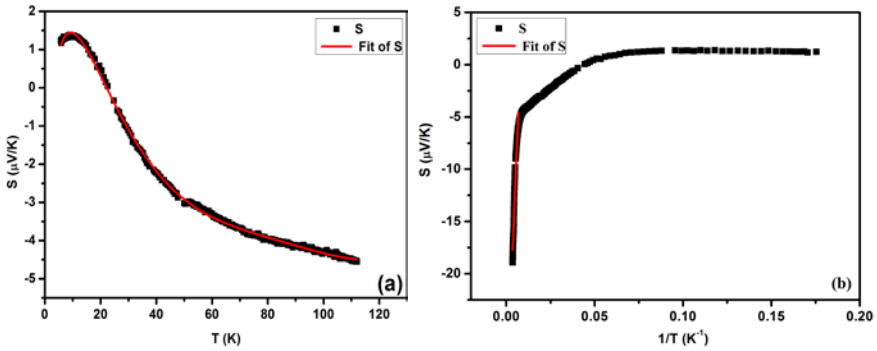

Figure 5.13: Variation of S with 1/T at (a) $T<T_{im}$ (b) $T>T_{im}$. The solid line gives the best fit to equations (5.8) and (5.9).

Thermoelectric power data are well fitted with equation (5.8) and this is shown in fig (5.13.a). The corresponding fitting parameters are included in table 5.3.

Table 5.3: The best fit parameters of the experimental TEP data.

S_0 (μV/K)	$S_{1/2}$ (μV/K$^{3/2}$)	S_1 (μV/K^2)	$S_{3/2}$ (μV/K$^{5/2}$)	S_2 (μV/K^3)	S_3 (μV/K^4)	S_4 (μV/K^5)	E_s meV	E_p meV	α'
-8.12	**7.01**	**-1.26**	**0.127**	**-0.014**	**9.55E-5**	**-2.58E-7**	**4.097**	**39.2**	**-0.37**

In the insulating region, the thermoelectric power data are fitted excellently with Mott's well known equation based on polaron hopping [36],

$$S = \frac{k_B}{e}\left[\frac{E_s}{k_B T} + \alpha'\right] \qquad (5.9)$$

where k_B is the Boltzmann constant, e is the electronic charge, E_s is the activation energy obtained from thermoelectric power data and α' is a constant of proportionality between the heat transfer and the kinetic energy of electron. $\alpha' < 1$ implies the existence of small polarons, while for $\alpha' > 2$ suggests that the conduction involves large polarons [37- 38]. From the slope of S versus 1/T plot, activation energy E_s and from the y intercept, the constant α' is obtained. The value of α' obtained from the equation (5.9) is found to be less than one. This strongly supports the small polaron conduction mechanism in the high temperature region. Figure (5.13.b) shows the best fit curve of S versus 1/T plot and the corresponding fitting parameters are given in table 5.3. By using Mott's equation for resistivity and TEP, activation energy from resistivity plots (E_p) for zero field and

activation energy from TEP plots (E_s) are calculated. The difference between these activation energies termed as polaron hopping energy ($W_H = E_p - E_s$) is found to be 35.1 meV. The huge difference in the values of activation energy is the indication towards the applicability of small polaron hopping (SPH) model in the insulator region. Thus high temperature thermoelectric power and resistivity studies indicate that small polaron hopping as the conducting mechanism.

5.4 Conclusions

The transport properties of strontium doped lanthanum manganite $La_{0.5}Sr_{0.5}MnO_3$ prepared by citrate gel method has been studied in detail. The XRD pattern of the sample showed a single phase homogeneous orthorhombically distorted perovskite structure in the space group R3c. The FC-ZFC magnetization studies revealed that in accordance with a metal to insulator transition there is a sharp ferromagnetic to paramagnetic transition indicating the role of double exchange. Due to the equal ratio of Mn^{3+} and Mn^{4+}, magnetic frustration occurs. Temperature dependent resistivity data measured under varying fields showed that the exact conduction mechanism in the high temperature region is due to polarons and the variation of low temperature electrical resistivity was explained using the combined effect of weak localization and magnon scattering. Resistivity minimum observed below 50 K and metal to insulator transition temperature was found to have strong dependence on the applied magnetic field. This resistivity minimum observed in the ferromagnetic- non-metallic regime shows a $T^{1/2}$ dependence, consistent with weak localization effects, and is explained by inter grain spin- polarized tunnelling through grain boundaries. The contribution of inter grain tunnelling in the low temperature minimum was confirmed by modelling experimental MR data. The shift in the metal to insulator transition peak of resistivity under the application of external field is

probably due to suppression of spin fluctuations. These results were correlated with the results from thermoelectric power measurements. The change of sign in the thermoelectric power is attributed to the orbital degeneracy of the e_g band. Large values of thermoelectric power were not observed in LSMO5 because of the absence of charge ordering.

References

[1] K.H. Fischer, Z. Phys. B Con. Mat.**42**, 245 (1981).

[2] Lija K. Joy, S.Shanmukharao Samatham, Senoy Thomas, V. Ganesan, Salim Al – Harthi, A. Liebig, M. Albrecht, and M. R. Anantharaman J. Appl. Phys. **116**, 213701, (2014).

[3] Lija K. Joy, Durgesh Singh, P M Sudeep,V Ganesan, P M Ajayan, Senoy Thomas and M R Anantharaman, Material Research Express **2**, 055504 (2015).

[4] P. Mandal, Phys. Rev. B **61**, 14675 (2000).

[5] Y. Tokura, Colossal Magneto-resistive oxides, Gordon and Breach Science Publishers, New York (2000).

[6] J. M. D. Coey and M. Viret, Advances in Physics **48**, 167 (1999).

[7] C. Zener, Phys. Rev. **2**, 403 (1951).

[8] A. Urushibara, Y. Moritomo, T. Arima, A. Asamitsu, J. Kido, and Y. Tokura, Phys. Rev. B **51**,14103 (1995).

[9] H. Fujishiro, M. Ikebe, and Y. Konno, Journal of the Physical Society of Japan **67**, 1799 (1998).

[10] Y. Moritomo, T. Akimoto, A. Nakamura, K. Ohoyama, and M. Ohashi, Phys. Rev. B **58**, 5544 (1998).

[11] M. Gupta, P. Yadav, W. Khan, A. Azam, A. H. Naqvi, R.K. Kotnala Adv. Mat. Lett. **3**(3), 220-225 (2012).

[12] G. Campillo, A. Gil, O. Arnache, J. J. Beltrán, J. Osorio and G. Sierra, J. Phys.: Conf. Ser. **466**, 012022 (2013).

[13] G. Venkataiah, V. Prasad , P. Venugopal Reddy, J. Alloys Compd. **429**, 1 (2007).

[14] J.B. Goodenough, Phys. Rev. **100**, 564 (1955).

s[15] Y. Tokura and Y. Tomioka, J. Magn. Magn. Mater. **200**, 1 (1999).

[16] S. Roy, Y. Q. Guo, S. Venkatesh and N. Ali, J. Phys.: Condens. Matter, **13**, 9547 (2001).

[17] S. Mollah, Z.A. Khan, D.K. Shukla, M. Arshad, Ravi Kumar, A. Das , J. Phys. Chem. Solids, **69**, 1023 (2008).

[18] X. J. Chen, C. L Zhang, C. C Almasan, J. S. Gardner and J.L Sarrao, Phys. Rev. B **67**, 094426 (2003).

[19] N.C. Yeh, C.C. Fu, J. Y. T. Wei, R. P. Vasquez, J. Huynh, S. M. Maurer, G. Beach, and D. A. Beam, J. Appl. Phys. **81**, 5499 (1997).

[20] G. Jakob, W. Westerburg, F. Martin, H. Adrian, Phys. Rev. B **58**, 14966 (1988).

[21] D. Varshney and N. Kaurav, J. Low Temp. Phys. **141**, 165 (2005).

[22] E. Rozenberg, M. Auslender, I. Felner, G. Gorodetsky, J. Appl. Phys., **88**, 2578 (2000).

[23] Y. Kalyana Lakshmi, G. Venkataiah, and P. Venugopal Reddy, J. Appl. Phys.**106**, 023707 (2009).

[24] C. L. Zhang, X. J. Chen, C. C. Almasan, J. S. Gardner and J. L. Sarrao, Phys. Rev. B, **65**, 134439 (2002).

[25] Y. S. Reddy, P. Kistaiah, C. Vishnuvardhan Reddy, Advances in Materials Physics and Chemistry, **2**, 49 (2012).

[26] A. I. Tovstolytkin, V. M Tsmots', L. I Pan'kiv, P. G Litovchenko and I.S Pan'kiv, Low Temp.Phys. **36**, 220 (2010).

[27] H. Y. Hwang, S.-W. Cheong, N. P. Ong, and B. Batlogg, Phys. Rev. Lett. **77**, 2041 (1996).

[28] P. Raychaudhuri, T. K. Nath, A. K. Nigam, and R. Pinto, J. Appl. Phys., **84**, 2048 (1998).

[29] Zhi-Hong Wang, Tian-Hao Ji, Yi-Qian Wang, Xin Chen, Run-Wei Li, Jian-Wang Cai, Ji-Rong Sun, and Bao-Gen Shen, J. Appl. Phys., **87**, 5582 (2000).

[30] M. Svedberg, S. Majumdar, H. Huhtinen, P. Paturi and S. Granroth, J. Phys. Condens. Matter **23**, 386005 (2011).

[31] J. A. Mydosh, Spin Glass: An Experimental Introduction, Taylor & Francis, London, (1993).

[32] G. Venkataiah, Y.K. Lakshmi and P.V. Reddy, PMC Physics B, 1:7 (2008).

[33] A. Asamitsu, Y. Moritomo and Y. Tokura, Phys. Rev. B **53**, R2952 (1996).

[34] S. Bhattacharya, S. Pal, A. Banerjee, H. D. Yang and B. K. Chaudhuri, J. Chem. Phys. **119**, 3972 (2003).

[35] B. H. Kim, J. S. Kim, T.H. Park, D.S. Lee, and Y. W. Park, J. Appl. Phys. **103**, 113717 (2008).

[36] N. F. Mott and E. A. Davis, Electronics processes in non-crystalline materials, (Clarendon, Oxford, 1971).

[37] A. Banerjee, S. Pal, S. Bhattacharya, H. D. Yang, and B. K. Chaudhuri, Phys. Rev. B **64**, 104428 (2001).

[38] S. Sagar, V. Ganesan, P. A. Joy, S. Thomas, A. Liebig, M. Albrecht and M. R. Anantharaman, Europhys. Lett. **91**, 17008 (2010).

Chapter 6

A study on the magnetic properties of Gd-Sr based low bandwidth manganites in their bulk and thin film forms

This chapter deals with the magnetic properties of both bulk and thin film forms of charge ordered Gd-Sr manganites belonging to the series $Gd_{1-x}Sr_xMnO_3$ (x= 0.3, 0.5, 0.6). In the case of bulk, it is found that the Gd moments order anti parallel to the manganese spins giving rise to a ferrimagnetic behaviour. A spin glass transition due to the competing ferromagnetic (FM) and antiferromagnetic (AFM) phases of manganese is observed at around 42K. Bulk form of $Gd_{0.7}Sr_{0.3}MnO_3$ exhibits magnetization reversal for applied fields of 25 Oe and 50 Oe at very low temperatures. In the two dimensional thin film forms of $Gd_{1-x}Sr_xMnO_3$, coercivity is different when compared to their bulk counterparts, moreover, the spin reversal and magnetic behaviour exhibited by thin films are at variance with respect to their bulk. An overview of structural and compositional analysis of films will be presented. Surface morphology of the films was examined from SEM and AFM images.

The work discussed in this chapter has been reported in: ***Journal of Magnetism and Magnetic Materials 398, 174–182 (2016).***

6.1 Introduction

The magnetic properties of mixed valent perovskite manganites strongly depend on the degree of substitution of trivalent elements by divalent cations [1]. The other factors that influence the nature of different magnetic interactions in these compounds are ionic radii of rare earth and dopant cations, small changes in Mn-O-Mn bond length and bond angles induced by tolerance factor [2-3]. There are very few literature reports dealing with heavy rare earth elements (Eu, Gd, Tb, Dy) based manganites, since their magnetization, conductivity and magnetic ordering temperatures are lower when compared to manganites based on lighter rare earths [4-6]. The replacement of lighter rare earth elements in mixed valent manganites by heavier rare earth elements induce lattice distortion associated with modification of tolerance factor which in turn influence the double exchange mechanism and hence influence magnetic interactions [2]. Due to smaller ionic radii of heavier rare earth R atom, Mn-O-Mn bond distribution is maximum and hence a weak double exchange results [7]. Since heavy rare earth elements exhibit largest magnetic moments of all the series, their intrinsic magnetism affects the magnetic response of the Mn sub lattice and thus the overall manganite system. Thus a diverse magnetic response of the overall manganite system is expected by incorporating heavier rare earth ions instead of lighter ones. It is reported that compounds with larger ionic radii such as La, Pr and Nd are ferromagnetic (FM), whereas compounds with smaller ionic radii such as Sm, Eu and Gd exhibit properties of spin glass [8]. Large difference in the ionic radii of R and A ions results in the Mn-O-Mn bond angle variation which in turn leads to spin glass state [9].

There have been reports on Gd and Dy based perovskites showing specific magnetic features including a reversal of magnetization at low temperatures [10]. The magnetization curves of perovskite manganites based

on smaller rare earth ions such as Dy, Tb, Gd show anomalies below 10K [10]. In $GdMnO_3$, besides Mn^{3+} ordering observed at 42K, due to the magnetization of Gd ions, spin ordering due to Gd spins were observed at around 7K [10-11]. Earlier Troyanchuk *et. al* reported that Gd ions magnetic moments were aligned opposite to the magnetic moments of Mn ions [12]. Spin reversal and ferrimagnetism have been observed in both bulk and thin film forms of $Gd_{0.67}Ca_{0.33}MnO_3$ [7, 13]. G. J. Snyder *et al.* explained the existence of a ferrimagnetic phase in $Gd_{0.67}Ca_{0.33}MnO_3$ by the antiferromagnetic interaction between Mn sub lattice with Gd sub lattice [4]. This ferrimagnetic interaction results into magnetic reversal and this depends on the applied field. Yanwei Ma *et al.* has studied the effect of application of magnetic field on the spin reversal of calcium doped $GdMnO_3$ [13]. The intrinsic magnetic nature of Gd ion plays an important role in the overall magnetic behaviour of the system. Due to the ionic radii mismatch of Gd and Sr, it is interesting to study the effect of Strontium doping on the magnetism in $GdMnO_3$ system. Since the mean size radius of Gd is smaller when compared to Sr, $Gd_{1-x}Sr_xMnO_3$ belonging to low bandwidth manganites and there exists a stable charge ordered phase over a wide range of doping (x=0.3 - 0.7) [14]. Earlier Garcia Landa *et. al* has reported the co-existence of charge ordered state and spin glass state in bulk form of $Gd_{0.5}Sr_{0.5}MnO_3$ [15]. The cluster glass like behaviour due to co-existence of ferromagnetic (FM) – antiferromagnetic (AFM) phases and ferrimagnetic interaction introduced by Gd substitution suggests an AFM exchange coupling between Gd^{3+} and Mn^{3+}/Mn^{4+} sub lattice.

Magnetic reversal was also reported in the thin film forms of $Gd_{0.67}Ca_{0.33}MnO_3$ [4, 13]. To fabricate a rich variety of electronic and magnetic devices, thin film form of these manganites with unique physical properties is necessary. Magnetization reversal is found to be an important

technology in magnetism used in magnetic data storage processes. A systematic study of both the spin reversal and spin glass existence in the charge ordered region of both bulk and thin film form of $Gd_{1-x}Sr_xMnO_3$ assume significance and less investigated. So it is in this context that a thorough investigation on thin film forms of $Gd_{1-x}Sr_x MnO_3$ is relevant.

It is presumed that in two dimensional thin film form of $Gd_{1-x}Sr_xMnO_3$, due to grain size effect, coercivity could be different when compared to bulk. Hence the magnetic behaviour exhibited by thin films will also be different. Also it is necessary to study the dependence of both coercivity and external applied field of thin films on the glassy behaviour, which was already reported in the bulk form of $Gd_{1-x}Sr_xMnO_3$ (x=0.3, 0.5 and 0.6) due to competing FM and AFM phases of manganese. To understand the nature of magnetic behaviour, polycrystalline thin film form of $Gd_{1-x}Sr_xMnO_3$ were prepared by pulsed laser deposition of polycrystalline bulk materials as targets which were synthesized by solid state reaction methods. As an initial investigation, these compositions were deposited on a silicon substrate by pulsed laser ablation. FC-ZFC magnetization measurements were carried out which could lead to the understanding of the interaction of Gd - Mn moments in bulk as well as thin films.

6.2 Experimental

6.2.1 Preparation of thin films

Bulk samples of Gd-Sr manganites belonging to the series $Gd_{1-x}Sr_xMnO_3$ (x = 0.3, 0.5, 0.6) were prepared by wet solid state reaction and compacted form of these compositions were employed as targets. For the synthesis of bulk samples, stoichiometric amounts of precursor materials namely, Gd_2O_3, $SrCO_3$ and MnO_2 were mixed in concentrated nitric acid. The solution was heated and excess nitric acid was boiled off. They were then calcined in air at 900^0C for 12 hours. After pre sintering, the black

powder were ground and pressed into pellets and sintered at 1200^0C in air for 72 hours. This sintered pellets were used as targets for depositing $Gd_{1-x}Sr_xMnO_3$ (x= 0.3, 0.5, 0.6) thin films on silicon substrates using pulsed laser deposition. A KrF excimer laser with 248 nm wavelength was employed for ablation and the estimated fluence was kept at about 2.91J/cm^2. To avoid the formation of native oxide layers on the surface of substrate, the substrates were pre-treated with HF solution before deposition. The substrate temperature was kept at 800^0C during film growth and the deposition was carried out under an oxygen pressure of about 2 mTorr.

6.2.2 Characterization

The crystal structure of both the bulk and thin films were analysed using X-ray diffractometer (Bruker D8 Discover) with an incident Cu K_α radiation source. Microstructural analysis and surface morphology of the films were carried out using Zeiss Ultra 55 Field Emission-Scanning Electron Microscopy (FE-SEM) and Veeco Dimension 3000 atomic force microscope (AFM). Composition of the film was confirmed using Rutherford Back Scattering spectroscopy (RBS) using He++ ions having energy of 1.7 MeV. Thickness of the film was determined by cross sectional SEM. To understand the nature of magnetic behaviour of thin films, Field Cooled (FC) – Zero Field Cooled (ZFC) and magnetic hysteresis (MH) measurements of magnetization were carried out using a Quantum Design superconducting quantum interference device.

6.3 Results and Discussions

6.3.1 Structural characterization using XRD

Figure 6.1 shows the X - ray diffraction pattern of thin films of GSMO. No impurity phase was found in any of the thin films. GSMO film grown on Si substrate exhibited the same structure as that of its bulk counterparts which is orthorhombic and with a space group of Pbnm. This is in agreement

with previous reports [14-15]. The XRD data have been analysed by refining the experimental data using a standard Rietveld refinement techniques using Full PROF program. The Rietveld refined XRD pattern of $Gd_{0.5}Sr_{0.5}MnO_3$ is shown in figure 6.2. Figure 6.3(a) and (b) shows Rietveld refinement for $Gd_{0.7}Sr_{0.3}MnO_3$ and $Gd_{0.4}Sr_{0.6}MnO_3$ thin films.

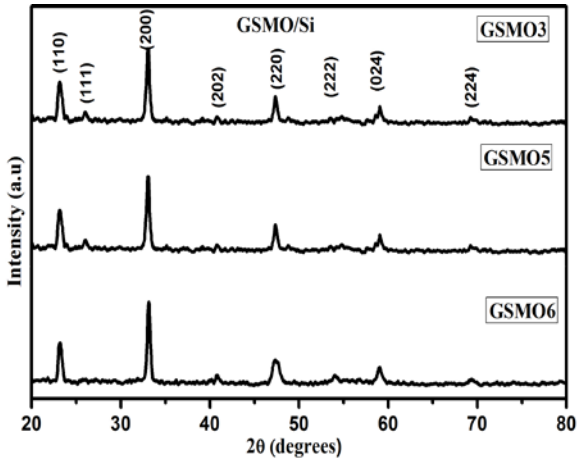

Figure 6.1: XRD pattern of $Gd_{1-x}Sr_xMnO_3$(x = 03, 0.5, and 0.6) thin films.

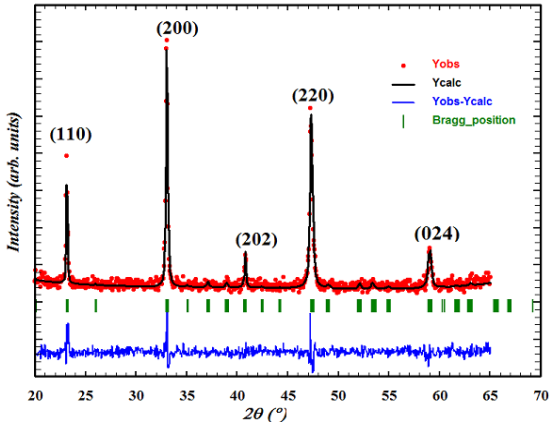

Figure 6.2: Rietveld refined XRD pattern of $Gd_{0.5}Sr_{0.5}MnO_3$ thin film.

The refined lattice parameters of all films are shown in table 6.1. A systematic decrease in lattice parameters is observed with increasing strontium substitution. An increase in lattice parameter with decreasing Strontium substitution is expected as in the case of bulk due to the larger

ionic radii of Sr^{2+} ions (0.144nm) compared to that of Gd^{3+} ions (0.107 nm). The lattice parameters and hence the cell volume of thin film samples are found to be slightly smaller than the bulk samples. This indicates that the unit cell of the film samples are compressed as compared to their bulk counterparts. XRD of bulk GSMO is already shown in figure 4.1.a and the refined lattice parameters are included in table 4.1. For convenience, the refined lattice parameters and crystallite size of bulk GSMO is reproduced in table 6.1. The average crystallite size estimated from XRD data using Scherrer's formula and also cell volume of both bulk and thin films of $Gd_{1-x}Sr_xMnO_3$ (x= 0.3,0.5,0.6) are estimated and shown in table 6.1. It is found that the average crystallite size of thin films is less than that of bulk. Earlier it was reported that the unit cell parameter decreases as the average crystallite size decreases [16].The grain size of the film is dependent on deposition parameters. The best stoichiometry as well as the single phase nature is retained in the films too.

Table 6.1. Structural parameters of GSMO bulk and thin films.

Sample codes	Bulk / Thin film	a Å	b Å	c Å	Crystallite size nm	Cell Volume $(Å)^3$
GSMO3	**Bulk**	**5.41±0.01**	**5.42±0.02**	**7.69±0.01**	**43**	**225.27**
GSMO5	**Bulk**	**5.40±0.02**	**5.41±0.02**	**7.68±0.01**	**41**	**224.27**
GSMO6	**Bulk**	**5.359±0.001**	**5.407±0.002**	**7.68±0.003**	**34**	**222.54**
GSMO3	**Thin film**	**5.402±0.001**	**5.42±0.01**	**7.682±0.002**	**37**	**224.92**
GSMO5	**Thin film**	**5.39±0.01**	**5.41±0.01**	**7.67±0.01**	**32**	**223.65**
GSMO6	**Thin film**	**5.357±0.003**	**5.407±0.002**	**7.666±0.004**	**25**	**222.05**

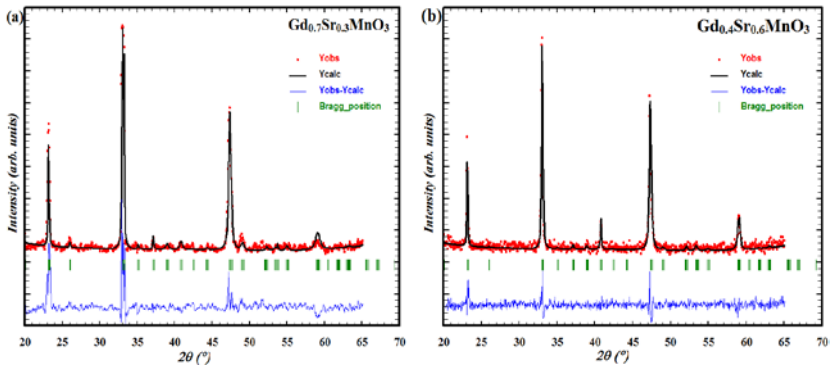

Figure 6.3: Rietveld refined XRD pattern of (a) $Gd_{0.7}Sr_{0.3}MnO_3$ (b) $Gd_{0.4}Sr_{0.6}MnO_3$ thin films.

6.3.2 Surface analysis by SEM

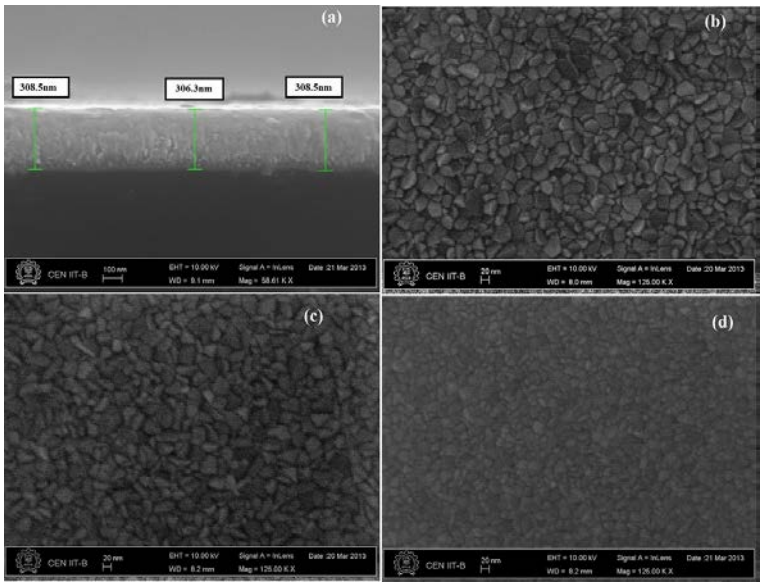

Figure 6.4: (a) Cross sectional SEM image of $Gd_{0.5}Sr_{0.5}MnO_3$ thin film, FE-SEM images of thin film forms of (b) $Gd_{0.7}Sr_{0.3}MnO_3$ (c) $Gd_{0.5}Sr_{0.5}MnO_3$ (d) $Gd_{0.4}Sr_{0.6}MnO_3$.

The average value of thickness calculated from cross sectional SEM of $Gd_{0.5}Sr_{0.5}MnO_3$ thin films is shown in figure 6.3.a and is found to be ~ 300 nm for all the films. Surface morphology of the films by SEM shows that the film surfaces are dense, compact and is uniform in nature. Films exhibit a well-defined structure with a visible grain boundary indicating the crystalline

nature. It is seen that the micro structure is quite homogeneous with an average grain size of nearly 37nm. Crystallite size estimated from XRD and grain size evaluated from SEM is found to be matching. Also the grain growth and crystallisation is observed with decreasing Strontium substitution. SEM images of GSMO3, GSMO5 and GSMO6 are respectively shown in figures 6.4.b, 6.4.c and 6.4.d. Grain size distribution of $Gd_{0.5}Sr_{0.5}MnO_3$ thin film is shown in figure 6.5.

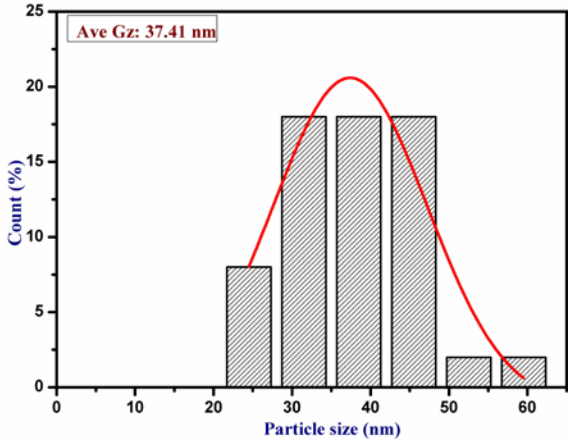

Figure 6.5: Representative grain size distribution of GSMO5 thin film.

6.3.3 Surface analysis by AFM

Topography and roughness of the films were analysed using an Atomic Force Microscope. AFM images of polycrystalline microstructures of $Gd_{1-x}Sr_xMnO_3$ (x = 0.3, 0.5, 0.6) films deposited on Si substrate is shown in figure 6.6.

From AFM images it is evident that the surface has a granular structure similar to that observed in the SEM. The morphology of the films shows a very dense structure having a very low roughness. Low value of roughness indicates that the structural features are homogeneous. This structure is observed to be similar to Zone II/ Zone T structures of "microstructure zones model" suggested by Thornton [17-18]. Hence both

AFM and SEM give a dense, closely packed morphology with a smooth surface. Root mean square roughnesses (RMS) of GSMO thin films on an area of 5µm x 5µm are also calculated. With decreasing strontium percentage the surface roughness and average grain size increases. The progressive morphological evolution of grain growth upon decreasing percentage of Strontium is clearly visible from the nature of surface by both SEM and AFM analysis.

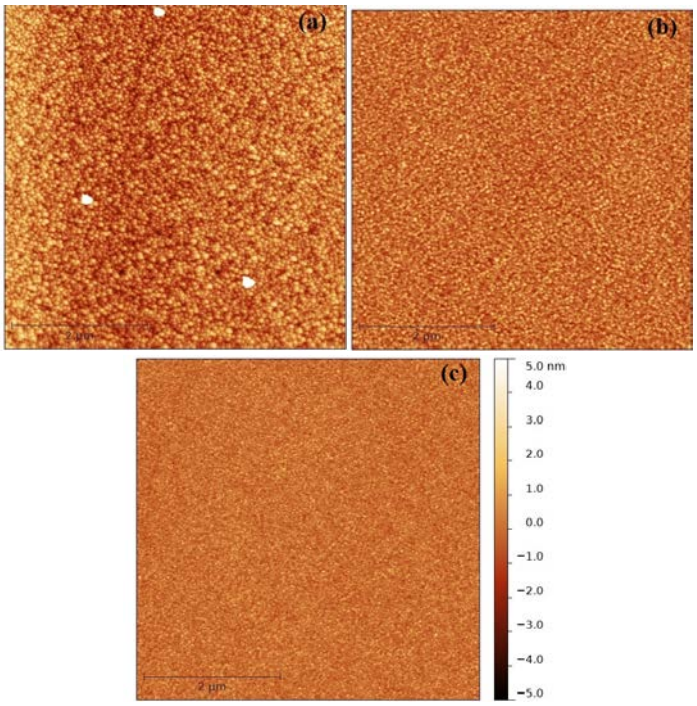

Figure 6.6: AFM images of thin film forms of (a) $Gd_{0.7}Sr_{0.3}MnO_3$ (b) $Gd_{0.5}Sr_{0.5}MnO_3$ (c) $Gd_{0.4}Sr_{0.6}MnO_3$. All images are in 5× 5 µm^2.

6.3.4 Rutherford Back Scattering Analysis

Figure 6.7 shows RBS analysis of $Gd_{1-x}Sr_xMnO_3$ (x = 0.3, 0.5, 0.6) thin films. The chemical composition of thin films was found out by RBS elemental analysis. The RBS spectra were fitted with the SIMNRA software and the results are summarized in table 6.2. As far as the composition of the films are concerned there is one to one correspondence with their bulk

targets. From the RBS data it is found that the samples synthesised were stoichiometric with respect to the oxygen content.

Table 6.2. Stoichiometry of GSMO thin films.

Film Name	Stoichiometry
GSMO3	$Gd_{0.71}Sr_{0.31}MnO_3$
GSMO5	$Gd_{0.51}Sr_{0.52}MnO_3$
GSMO6	$Gd_{0.41}Sr_{0.6}MnO_3$

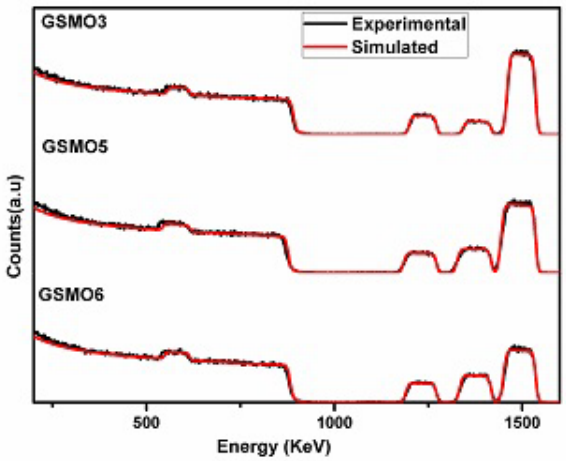

Figure 6.7: RBS spectrum of GSMO thin films.

6.3.5 Magnetization Measurements

6.3.5.1 MH measurements

Magnetization as a function of applied field at 10K of $Gd_{1-x}Sr_xMnO_3$ (x = 0.3, 0.5, 0.6) in bulk form is shown in figure 6.8. The magnetic hysteresis loops for thin films of $Gd_{1-x}Sr_xMnO_3$ (x = 0.3, 0.5, 0.6) measured up to 80 kOe at 10K and 300K are shown in figure 6.9. Coercivity of both bulk and thin film form of $Gd_{1-x}Sr_xMnO_3$ (x = 0.3, 0.5, 0.6) are noted separately in their corresponding MH loops. It is to be noted that coercivity in thin films is very much lesser when compared to their bulk target. This can be due to their lower crystallinity and smaller grain size when compared to their bulk target. It is found that at 10K the loop is not saturated even in an

applied field of 70 kOe. Unsaturated increase of magnetization is indicative of a ferrimagnetic like state in both thin films and bulk.

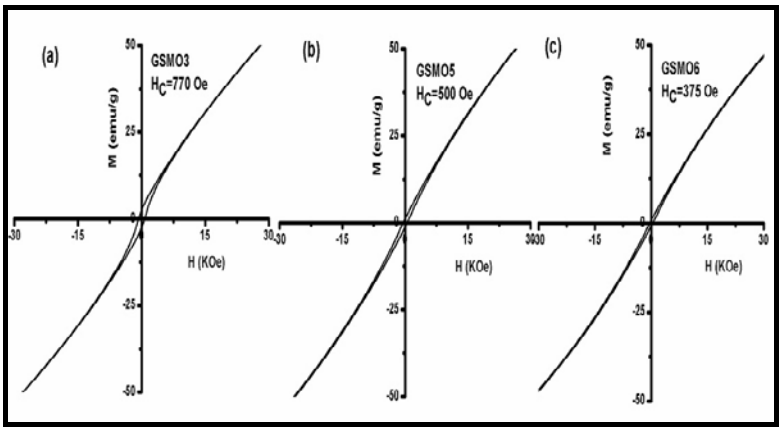

Figure 6.8: Magnetic hysteresis loops of $Gd_{1-x}Sr_xMnO_3$ bulk at 10K (a) x=0.3, (b) x=0.5 and (c) x=0.6.

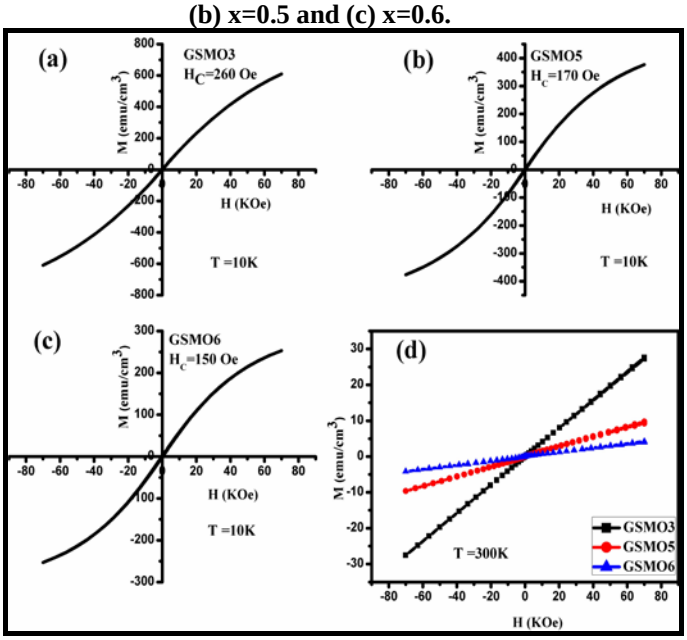

Figure 6.9: Magnetic hysteresis loops of $Gd_{1-x}Sr_xMnO_3$ thin film at 10K (a) x=0.3. (b) x=0.5 (c) x=0.6 (d) Magnetic hysteresis loops of $Gd_{1-x}Sr_xMnO_3$ (x=0.3, 0.5, 0.6) thin film at 300K.

There are several reports highlighting a magnetic phase change exhibited by manganites [7, 10, 19-22]. It has been reported that a meta magnetic FM phase can be formed by the partial transformation of CO/AFM phases under high field. As $Gd_{1-x}Sr_xMnO_3$ belonging to small bandwidth manganites, range of compositions showing charge ordering is wide rather than usual single composition at x= 0.5 as in other manganites. Hence samples with x= 0.3, 0.5, 0.6 are charge ordered. In charge ordering, both FM and AFM phases co- exist and this may results in competitive magnetic interactions.

6.3.5.2 FC - ZFC magnetic measurements

FC - ZFC measurements carried out on bulk form of $Gd_{1-x}Sr_xMnO_3$ (x = 0.3, 0.5, 0.6) under a magnetic field of 200 Oe is shown in figure 6.10. The substitution of trivalent Gadolinium by divalent Strontium converts Mn^{3+} into Mn^{4+}. Going from x = 0.3 to x = 0.6, it is found that effective magnetic moment decreases. This is because for the composition corresponding to x=0.3, the double exchange effect is maximum as seen in the case of Lanthanum compounds.

Temperature dependent magnetization studies under applied fields of 25 Oe and 50 Oe of bulk $Gd_{0.7}Sr_{0.3}MnO_3$ (GSMO3) is shown in figure 6.11. When a magnetic field of 25 Oe, which is very much less than their coercive field (H_C = 770 Oe), is applied on GSMO3, ZFC magnetization first decreases with increasing temperature and then rapidly increases to a maximum, T_{cusp} and finally reaches the reversible state at $T_{irr.}$ While FC magnetization increases with decreasing temperature, it reaches a maximum and then sharply decreases to zero and goes to negative values on further cooling. The temperature at which magnetization decreases to zero is called compensation temperature and the phenomenon of attaining negative values is called magnetic reversal [4]. Here FC curve crosses the temperature axis at

the compensation temperature T_{comp}=11K and goes to a negative value for a field (25 Oe) lower than its coercive field. Earlier Snyder *et al.* also found a similar type of magnetic reversal in Calcium substituted $GdMnO_3$ [4]. They explained this anomaly by attributing it to the interaction of Gd sub lattice with Mn sub lattice.

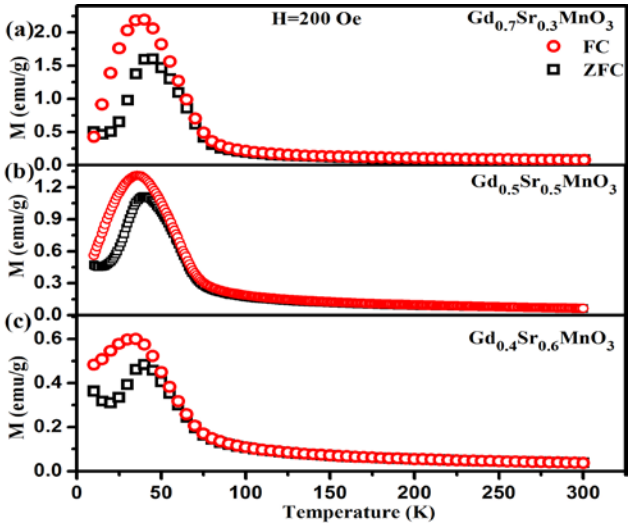

Figure 6.10: ZFC and FC magnetization measurements of bulk $Gd_{1-x}Sr_x MnO_3$ (x= 0.3, 0.5, 0.6) under a magnetic field of 200 Oe.

The ordering of manganese (Mn^{3+} and Mn^{4+}) spins due to strong competition between FM phase and AFM phase results in the formation of a frustrated state, termed as spin glass, is observed at around 42K. It is noticed that FC and ZFC splitting gap is substantial under low applied fields (25 Oe and 50 Oe) unlike the splitting observed under an applied field of 200 Oe. Thus it can be concluded that irreversibility decreases at higher applied fields. This thermomagnetic irreversibility is also an indication of the existence of a glass state [22]. Garcia Landa *et.al* has reported the presence of a spin glass in $Gd_{0.5}Sr_{0.5}MnO_3$ at 42K [15]. There are also reports on the co- existence of CO and spin glass state at low temperatures in manganites

[23-25]. At glass transition temperatures the dominating magnetization is due to the ordering of manganese spins. Below this temperature, Gd spins became more dominant and hence FC magnetization decreases and magnetic reversal is observed on further cooling under the applied field.

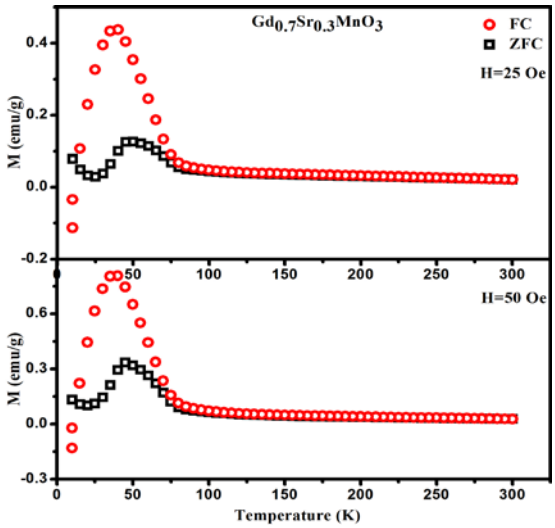

Figure 6.11: ZFC and FC magnetization measurements of bulk $Gd_{0.7}Sr_{0.3}MnO_3$ under magnetic fields of (a) 25 Oe and (b) 50 Oe.

Thus this system behaves as a ferrimagnetic like system of two interacting magnetic sub lattices of Manganese and Gadolinium. The substitution of trivalent Gd by divalent Sr converts Mn^{3+} into Mn^{4+} and also generates magnetic clusters. On cooling under the presence of a small field, a field lower than the coercive field, the Mn sub lattice orders ferromagnetically, while the Gd sub lattice polarise in an opposite direction to the external field. Also at T_{cusp}, due to competing FM and AFM phases of manganese gives rise to an ordering of the lattice and aids in the culmination of a frustrated glass state. This accounts for the increase in magnetization and peaks at T_{cusp}.

Below spin glass transition, magnetic contributions of Gd^{3+} 4f spins are prominent. Upon further cooling, Gd^{3+} spins are aligned anti parallel to canted Mn^{3+}/Mn^{4+} spins. This antiferromagnetic interaction of Gd sub lattice with Mn sub lattice reduces the net magnetization. When the temperature is lowered to compensation temperature, magnetic moments of Gd and Mn cancel exactly. Below this temperature, negative magnetization is observed. While in ZFC, the magnetization is positive in the entire temperature with a minimum dip at 24K. Curie - Weiss contribution at low temperatures in ZFC can be due to the effect of the external field on Gd sub lattice. However for a higher applied field of 200 Oe, even lower than the coercivity of GSMO3, FC magnetization no longer becomes negative. The paramagnetic contribution of Gd is more and more supporting due to the increasing field strength and it takes positive values. Earlier Yanwei Ma *et al*. has studied the effect of application of magnetic field on the spin reversal behaviour of calcium doped $GdMnO_3$ [13]. They reported that if the applied field is greater than the coercive field, Gd ions flip to align parallel with the external field with an increase in both FC and ZFC magnetisation. No dip in magnetization is observed at an applied field of 200 Oe, a field lower than its H_C.

Magnetization measurements of bulk $Gd_{1-x}Sr_xMnO_3$ (x=0.5, 0.6) under ZFC and FC conditions in a magnetic field of 25 Oe are shown in figure 6.12. With increasing strontium concentration, the transition at low temperature corresponding to Gd moments is reduced because Sr doping dilutes the magnetic Gd sub lattice. This kind of dilution of rare earth ion by Sr doping was earlier reported by S Robler *et al.* in Sr doped $DyMnO_3$ [26]. Hence for compositions x = 0.5 and 0.6, Curie Weiss contribution of Gd moments at lower temperatures is lesser when compared to x= 0.3.

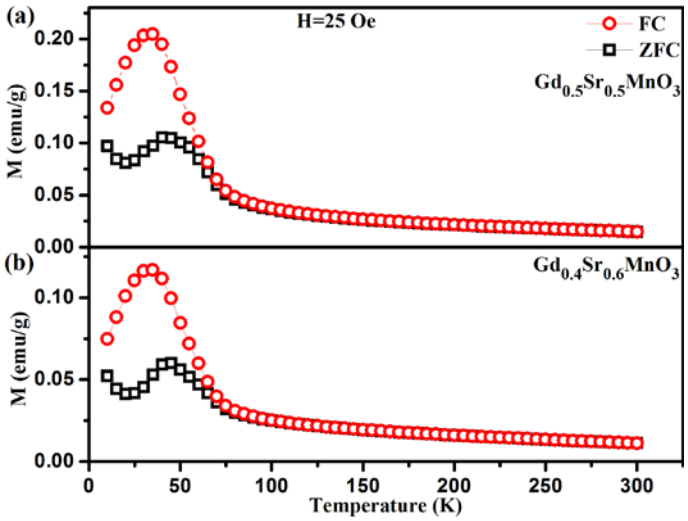

Figure 6.12: ZFC and FC magnetization measurements of bulk (a) $Gd_{0.5}Sr_{0.5}MnO_3$ (x= 0.3, 0.5, 0.6) and (b) $Gd_{0.4}Sr_{0.6}MnO_3$ under a magnetic field of 25 Oe.

As the maximum external field applied is 200 Oe, which is very much less than the coercive field of bulk, increase in magnetisation by the Curie Weiss contribution of Gd ions is not seen in the case of bulk samples under study. While for thin films it is found that coercivity is very much lesser when compared to their bulk. In the case of $Gd_{0.7}Sr_{0.3}MnO_3$ thin film, the paramagnetic contribution of Gd ions are more dominant and they orient along the field leading to an increase in both FC and ZFC magnetizations with a dip in the magnetization at 20K which is shown in figure 6.13.a.

When a small field of 25 Oe is applied, similar to bulk due to ferrimagnetic interaction of Gd and Mn sub lattices, both FC and ZFC magnetization decreases after exhibiting their glassy transition at 40K. FC magnetization goes on decreasing with temperature while ZFC magnetization increases after a minimum at T = 20K. This is shown in figure 6.13.b.

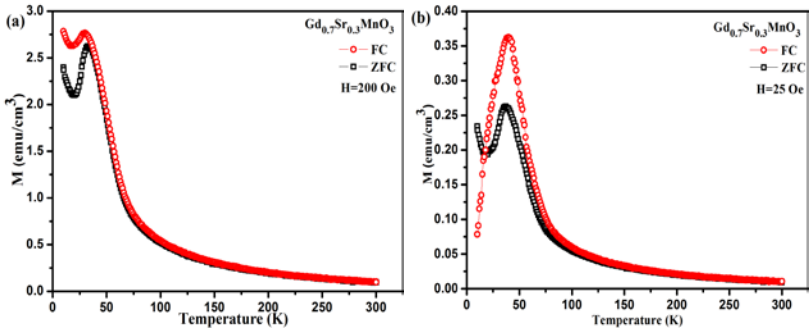

Figure 6.13: ZFC and FC magnetization measurements of $Gd_{0.7}Sr_{0.3}MnO_3$ thin film under a magnetic field of (a) 200 Oe and (b) 25 Oe.

The coercivity of thin films of $Gd_{1-x}Sr_xMnO_3$ decreases with increasing Sr, therefore GSMO3 exhibits higher coercivity. Hence the ferrimagnetic behaviour shown by x = 0.3 under an applied field of 200 Oe is absent for x= 0.5 and 0.6 under the same applied field (200 Oe $<<H_C$). Temperature dependent magnetization studies in 200 Oe for field cooling and zero field cooling of $Gd_{1-x}Sr_xMnO_3$ (x=0.5, 0.6) thin films is shown in figure 6.14. Unlike bulk, the magnetization variation of $Gd_{1-x}Sr_xMnO_3$ (x=0.5, 0.6) thin films is paramagnetic in nature. This is due to the application of a field higher than their coercive field. When the applied field is high, the internal field produced at the Gd sites by Mn sub lattice is low and hence an applied field of 200 Oe, which is higher than coercive field, is strong enough to align Gd ions parallel to this field and leading to the superposition of Gd and Mn sub lattices. A small slope change in ZFC under 200 Oe was observed at around the glass transition temperature of 40K. Under an applied field of 500 Oe $>>H_C$, this transition vanishes. For a higher field of 500 Oe the frustrated glassy state melts resulting in a paramagnetic behaviour. This is shown in figure 6.14.b. FC-ZFC curves are almost identical at higher fields which are indicative of the melting of glass state [25].

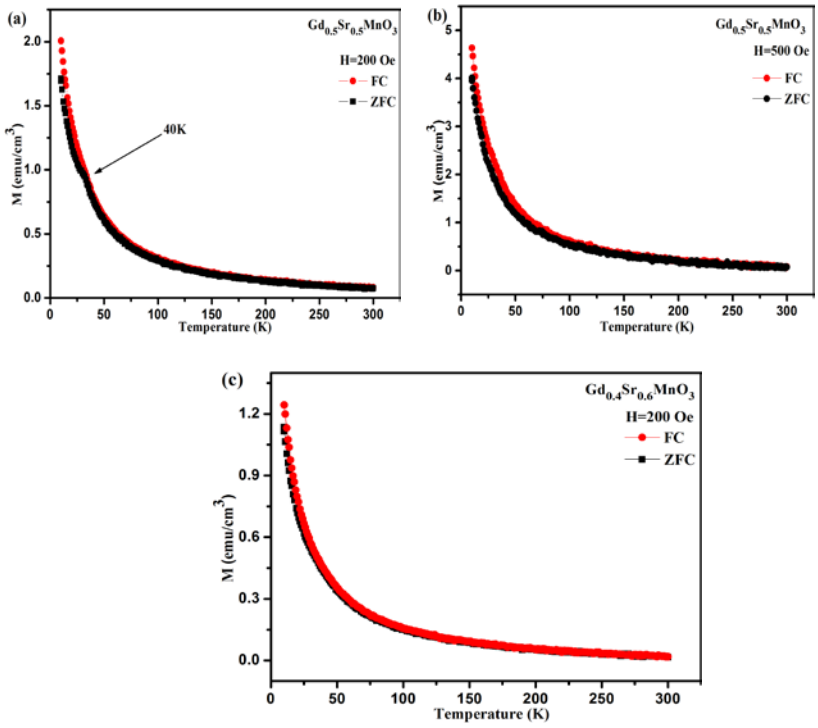

Figure 6.14: ZFC and FC Magnetization measurements of $Gd_{0.5}Sr_{0.5}MnO_3$ thin film under a magnetic field of (a) 200Oe and (b) 500Oe, (c) $Gd_{0.4}Sr_{0.6}MnO_3$ thin film under a magnetic field of 200 Oe.

6.4 Conclusions

Bulk and thin film samples belonging to the series $Gd_{1-x}Sr_xMnO_3$ (x = 0.3, 0.5, 0.6) were prepared and characterized. The lower coercivity of thin films when compared to bulk is attributed to their smaller crystallinity and grain size. With strontium substitution coercivity is found to be decreasing and hence $Gd_{0.7}Sr_{0.3}MnO_3$ exhibits higher coercivity. Magnetic reversal was observed in bulk form of $Gd_{0.7}Sr_{0.3}MnO_3$ at very low temperatures in small external fields. This is due to the antiferromagnetic interaction of Gd - Mn sub lattice in $Gd_{0.7}Sr_{0.3}MnO_3$. For $Gd_{0.5}Sr_{0.5}MnO_3$ and $Gd_{0.4}Sr_{0.6}MnO_3$, the transition at low temperature corresponding to Gd moments is reduced and hence magnetic reversal is absent. Spin glass transition was observed in Gd_{1-}

$_xSr_xMnO_3$ (x = 0.3, 0.5, 0.6) at around 42K. The magnetic transitions exhibited by $Gd_{0.7}Sr_{0.3}MnO_3$ thin films under a field of 200 Oe (ZFC - FC) were quite similar to their bulk counterparts. Due to lower coercivity of thin films corresponding to higher doping (x= 0.5 and 0.6), the applied field is enough to suppress both the glassy and ferrimagnetic nature.

References

[1] J. M. D. Coey, M. Viret and S. von Molnaír Adv. Phys.**48**, 167 (1999).

[2] Young Sun, M. B. Salamon, Wei Tong and Yuheng Zhang, Phys. Rev. B **66**, 094414 (2002).

[3] J. B. Goodenough, J. Alloys Compd. **1**, 262–263 (1997).

[4] G. Jeffrey Snyder, C. H. Booth,F. Bridges, Ron Hiskes, Steve DiCarolis, M. R. Beasley and T. H. Geballe, Phys.Rev. B **55**, 6453 (1997).

[5] T. Kimura, T. Goto, H. Shintani, K. Ishizaka, T. Arima and Y. Tokura, Nature **426**, 55 (2003).

[6] W. Eerenstein, N. D. Mathur, and J. F. Scott, Nature **442**, 759 (2006).

[7] Octavio Pena, Mona Bahout, Karim Ghanimi, Pedro Duran, Dionisio Gutierrez and Carlos Moure, J. Mater. Chem. **12**, 2480 (2002).

[8] I.O. Troyanchuk, S.V. Trukhanov, and H. Szymczak, Crystallography Reports, **47**, 652 (2002).

[9] S.V. Trukhanov, I.O. Troyanchuk, M. Hervieu, H. Szymczak, K. Bärner Phys. Rev. B **66**, 184424 (2002).

[10] Raja Das, Adhish Jaiswal and Pankaj Poddar, J. Phys. D: Appl. Phys. **46**, 045301 (2013).

[11] P. Negi, G. Dixit, H.M. Agrawal, R.C. Srivastava, J Supercond Nov Magnn. **26**, 1611 (2013).

[12] I.O. Troyanchuk, S.V. Trukhanov, D.D. Khalyavin and H. Szymczak, J. Magn. Magn. Mater. **208**, 217 (2000).

[13] Yanwei Ma, M. Guilloux-Viry, P. Barahona, O. Peña and C. Moure, Appl. Phys. Lett. **86**, 062506 (2005).

[14] S. Sagar, V. Ganesan, P. A. Joy, Senoy Thomas, A. Liebig, M. Albrecht and M. R. Anantharaman, Euro Phys. Lett.**91**, 17008 (2010).

[15] B. Garcia-Landa, J. M. De Teresa, and M. R. Ibarra, J. Appl. Phys. **83**, 7664 (1998).

[16] S.V. Trukhanov, A.V. Trukhanov, S.G. Stepin, H. Szymczak and C.E. Botez, Phys. Solid State. **50**, 886 (2008).

[17] J. A. Thornton, J. Vac. Sci. Technol. A. **4**, 3059-3065 (1986).

[18] M. Koubaa, A. M. Haghiri-Gosnet, R. Desfeux, P. Lecoeur, W. Prellier, B. Mercey, J. Appl. Phys. **93**, 5227-5235 (2003).

[19] X. L. Wang, D. Li, T. Y. Cui, P. Kharel, W. Liu and Z. D. Zhang, J. Appl. Phys. **107**, 09B510 (2010).

[20] L. S. Uspenskaya, I. V. Kurbatova, G. Nurgaliev and S. Miteva, Bull. Russ. Acad. Sci.: Phys. **73**, 1110 (2009).

[21] V. S. Kolat, T. Izgi, A. O. Kaya, N. Bayri, H. Gencer and S. Atalay, J. Magn. Magn. Mater. **322**, 427 (2010).

[22] M. Svedberg, S. Majumdar, H. Huhtinen, P. Paturi and S. Granroth, J. Phys.Condens. Matter **23**, 386005 (2011).

[23] A.A.Wagh, P S Anil Kumar, H L.Bhat and Suja Elizabeth, J. Phys.: Condens. Matter **22**, 026005 (2010).

[24] A.A.Wagh, P.S. Anil Kumar, H L. Bhat and Suja Elizabeth, J Supercond Nov Magn 24 (2011) 665 (2010).

[25] T. Tang, R.S. Huang and S.Y. Zhang, Solid State Commun. **147**, 190 (2008).

[26] S. Robler, S. Harikrishnan, U. K. Robler, Suja Elizabeth, H. L. Bhat, F. Steglich and S. Wirth, JPCS. **200**, 012168 (2010).

Chapter 7

Conclusion and Future Scope

The inferences drawn out of this investigation is provided in this chapter. The scope for further studies is also highlighted in this chapter. Several positives outcomes of this investigation along with some of their limitations are also dealt within this chapter. Moreover, preliminary experiments carried out on $Ca_{0.9}Yb_{0.1}MnO_3$ indicate that they exhibit appreciable Seebeck coefficient at room temperature and the initial results of this work are also briefly discussed in this chapter.

Conclusion and…

Chapter 7

The necessity of finding eco-friendly alternatives to conventional sources of energy is being felt now than never before, especially with dwindling natural resources. The emphasis on preserving the ecology for future generations and the civil society's activism has been a driving force in finding alternatives. Worldwide, a huge amount of heat is generated and is wasted, be it in industrial plants, exhaust of automobiles or even in our own work place, there is an opportunity to tap waste heat.

Thermoelectricity and thermoelectric materials are bound to play a lead role in converting waste heat into useful energy. Thermoelectric materials are in the forefront of research and development for the last two decades or so. They can be employed either for generation of electricity or production of cooling. Scientists have been scouting for newer materials for conversion of heat into energy and in this search they have tumbled upon a few materials. They are semiconductors such as Bi_2Te_3, Sb_2Te_3, PbTe and GeTe, skutterudites or clathrates and quantum dot superlattices such as PbTe/PbTeSe. However, they have their own merits and demerits.

Manganites belong to a class of materials which have been thoroughly investigated during the last five to six decades. In the 50's and 60's, they were in the lime light because of their potential applications in the regime of catalysis. During the high T_C era of superconductors, they were again under scrutiny because of the fact that they are correlated systems. Manganites became the cynosure of all eyes once again with the discovery of GMR/CMR.

Perovskite manganites are excellent electron correlated systems possessing different phase states and transitions with a close correlation between structure, electron transport and magnetic properties. So perovskite structured manganites having the general formula $RE_{1-x}AE_xMnO_3$ are

capable of displaying a large value of Seebeck coefficient. This, once again brings the spot light back on these class of materials as potential thermoelectric materials. Through this thesis, we examined the suitability of manganites as a potential material for thermoelectric applications. The conclusion drawn out of this small piece of investigations is listed in this chapter. In any study, there is bound to be a gap between the intended and achieved. In this investigation too, there are grey areas and lacunae. This is also brought out. As the saying goes "Wisdom dawns only late", here too, we realized that there existed a huge scope for some more investigation for attaining completeness, which could not be carried out; however, this is projected as futuristic. The scope for further investigation is also brought out after carrying out an initial study and the preliminary results obtained on $Ca_{0.9}Yb_{0.1}MnO_3$ are also included in the section under conclusion.

Manganites exhibit a variety of properties vis a vis charge, orbital and magnetic ordering, colossal magneto resistance and Jahn-Teller effect. They are expected to display substantial thermoelectric power at temperatures where there is co-existence of magnetic order and charge order. Manganites can be classified into small, intermediate and large bandwidth based on the overlapping of Manganese e_g and Oxygen p orbitals.

Intermediate bandwidth manganites based on Calcium, especially the charge ordered composition, $La_{0.5}Ca_{0.5}MnO_3$, was synthesized by high energy ball milling. The sample possessed a distorted orthorhombic perovskite structure with a Pbmn space group. Both the surface composition and the optimal Mn^{4+}- Mn^{3+} concentration in charge ordered LCMO5 was examined by XPS analysis. A strong competition between the FM and AFM order due to charge ordering resulted in a spin-glass state in the temperature regime T<120K. Thermoelectric power (TEP) data was systematically analyzed by dividing the entire temperature range (5K- 300K) into three

different regimes to explore different scattering mechanisms involved. Mandal's model was applied to explain TEP data in the region below the Curie temperature (T_C). It has been found that the variation of thermoelectric power with temperature is pronounced when the system enters the charge ordered region at T <200K. For temperatures lower than120K, due to the co-existence of charge ordered state with a spin-glass state, the variation of thermoelectric power is maximum and exhibited a peak value of -80mV/K at 58K. The observed colossal thermoelectric power was explained by incorporating Kondo properties of the spin-glass along with magnon scattering as proposed by Mandal. TEP data in the charge ordered region ($120<T<T_C$) is explained by including a phonon drag term in Mandal's model, instead of a spin-glass contribution.Thermoelectric power in the region above the Curie temperature is due to the presence of small polarons in the high temperature regime.

To study the effect of grain size on the contribution to thermoelectric properties from different scattering mechanisms, single phasic charge ordered small bandwidth manganites, $Gd_{1-x}Sr_xMnO_3$ (x =0.3, 0.5 and 0.6) were prepared using solid state reactions. They were then subjected to high energy ball milling to reduce the size of the grains. Both the surface composition and the optimal Mn^{4+}- Mn^{3+} concentration in charge ordered milled and unmilled GSMO samples were estimated by XPS analysis. The colossal thermoelectric power obtained at the low temperature for both unmilled and milled samples was explained based on charge ordered spin glass state. The samples having smaller grain size exhibited increased thermoelectric power over the samples having larger grain size for GSMO samples. Compared to unmilled samples, thermoelectric power of charge ordered milled GSMO samples displayed higher values. This is due to the

increased phonon scattering. One could also witness pronounced changes in the thermoelectric transition temperatures with decrease in grain sizes.

From magnetic measurements of bulk $Gd_{1-x}Sr_xMnO_3$ (x =0.3, 0.5 and 0.6), it was found that the Gd moments order anti parallel to the manganese spins giving rise to a ferrimagnetic behaviour. A spin glass transition due to the competing ferromagnetic (FM) and antiferromagnetic (AFM) interactions is observed at around 42K. Bulk form of $Gd_{0.7}Sr_{0.3}MnO_3$ exhibited magnetization reversal for applied fields of 25 Oe and 50 Oe at very low temperatures.

To study the dimensional dependence on the magnetic properties, thin film forms of these manganites with unique physical properties are necessary. To understand the nature and origin of both spin glasses and spin reversal, polycrystalline thin film form of $Gd_{1-x}Sr_xMnO_3$ (x =0.3, 0.5 and 0.6) were prepared by pulsed laser deposition of polycrystalline bulk materials as targets which were synthesized by solid state reaction methods. In $Gd_{1-x}Sr_xMnO_3$ thin films, coercivity was found to be lower when compared to their bulk counterparts. Thin films of $Gd_{0.7}Sr_{0.3}MnO_3$ exhibited both glassy and ferrimagnetic behaviour for an applied magnetic field of 200 Oe similar to bulk. While for x= 0.5 and 0.6, coercivity was lower and therefore an applied magnetic field of 200 Oe was large enough to suppress both the glassy and ferrimagnetic phases in thin films. Reduced coercivity of thin films when compared to bulk has been attributed to the grain size effect.

Though colossal thermoelectric power was obtained in LCMO and milled and unmilled samples of GSMO, they were all at lower temperatures. There existed strong interdependence between magnetic orders and charge ordering. $La_{0.5}Sr_{0.5}MnO_3$ is a large bandwidth manganite and there exist no charge ordering. Thermoelectric measurements were carried out on single phasic $La_{0.5}Sr_{0.5}MnO_3$. The FC-ZFC magnetization studies revealed that

along with a metal to insulator transition there is a sharp ferromagnetic to paramagnetic transition indicating the role of double exchange. Due to the equal ratio of Mn^{3+} and Mn^{4+}, magnetic frustration occurs. Temperature dependent resistivity data measured under varying fields showed that the exact conduction mechanism in the high temperature region is due to polarons and the variation of low temperature electrical resistivity was explained using the combined effect of weak localization, electron-electron and magnon scattering. Resistivity minimum observed below 50 K and metal to insulator transition temperature was found to have strong dependence on the applied magnetic field. This resistivity minimum observed in the ferromagnetic- non-metallic regime shows a $T^{1/2}$ dependence, consistent with weak localization effects, and is explained by inter grain spin- polarized tunnelling through grain boundaries. These results were correlated with the results from thermoelectric power measurements. Large values of thermoelectric power were not observed in LSMO5 because of the absence of charge ordering.

All throughout this work we have observed that colossal thermoelectric power is exhibited by both small and intermediate bandwidth manganites only at low temperatures. LCMO showed a colossal thermoelectric power of -80mV/K at 58K and bulk GSMO samples exhibited thermoelectric power of ~ -35mV/K. The most important performance indicator of a thermoelectric material is ZT, which was not evaluated in any of the above samples. The evaluation of ZT requires that the thermal conductivity, electrical conductivity as well as thermoelectric power is estimated at these temperatures. In none of the samples investigated under the present study described in various chapters, ZT was not evaluated. With a view to finding a material which exhibits appreciable thermoelectric power at room temperature we embarked on an investigation on heavy rare earth,

Ytterbium, based $CaMnO_3$ ($Ca_{0.9}Yb_{0.1}MnO_3$). The initial results are described in the ensuing paragraphs.

Single phasic $Ca_{0.9}Yb_{0.1}MnO_3$ is prepared. XRD is shown in the inset of figure 7.1.a. The thermoelectric power, thermal conductivity and electrical conductivity of this sample in the temperature range of 295K to 380 K are depicted in figure (7.1).

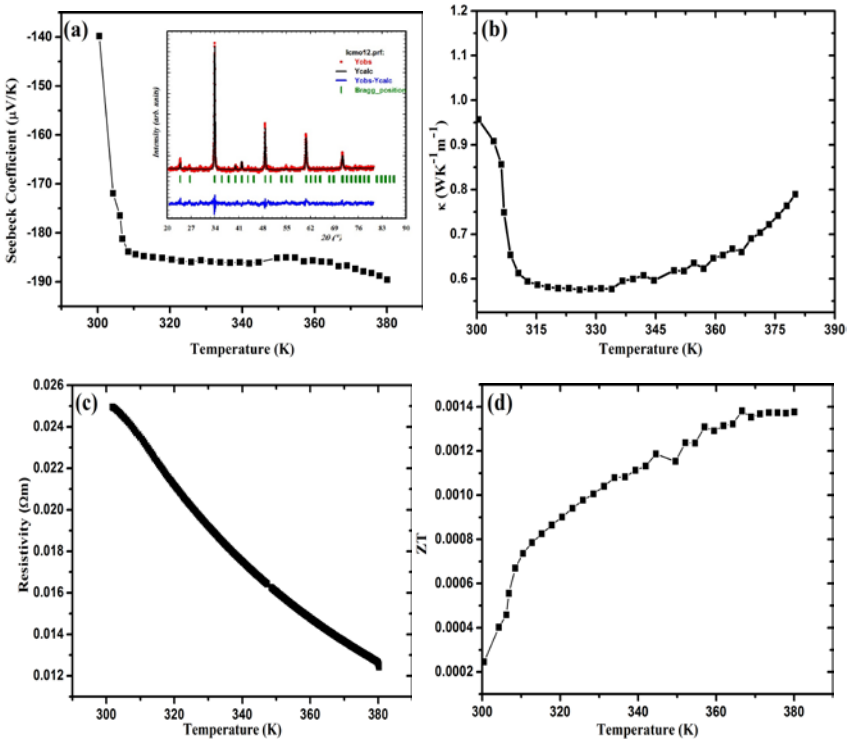

Figure 7.1: Variation of (a) thermoelectric power (b) thermal conductivity (c) resistivity and (d) thermoelectric efficiency with respect to temperature.

An appreciable thermoelectric power of about -170 μV/K at room temperature was observed which is almost double when compared to earlier reported values of -85 μV/K. A lowest thermal conductivity of about $0.9566 Wm^{-1}K^{-1}$ was exhibited by the sample at room temperature. Temperature dependent resistivity data showed that the exact conduction

mechanism in the high temperature region is due to polarons. This points out that the thermoelectric power is mainly decided by the presence of small polarons in the high temperature region. In this region, distortion became more prominent which induces enhanced phonon scattering which results in lower phonon thermal conductivity. Combining the three factors *S*, ρ, and κ the dimensionless figure merit ZT, is evaluated. ZT values are very much lower, which is mainly because of lower electrical conductivity. This low electrical conductivity is due to the contribution from oxygen vacancies. Further experiments are to be conducted to estimate the amount of oxygen vacancies. Even though ZT is found to be low, high thermoelectric power and low thermal conductivity observed at room temperature is quite promising and opens an altogether new window of opportunities for further investigations in these classes of materials. However, it must be mentioned here that appropriate preparation techniques are to be adopted to enhance the electrical conductivity without compromising on thermoelectric power and thermal conductivity.

There are many positives in the present study. A remarkable feature of this study is the observation of colossal thermoelectric power at low temperatures where there is coexistence of magnetic order along with charge ordering. Initial experiments to study the size effect indicated that nanostructuring did have a positive influence in enhancing the temperature of transition to higher temperatures with enhanced thermoelectric power values. However, they are not that substantial enough to elevate these class of materials towards the room temperature regime. A striking feature of this probe is that both low and medium bandwidth manganites exhibited colossal thermoelectric power, while a large bandwidth manganite exhibited promising values of thermoelectric power and electrical conductivity at near room temperature.

On the negative side, neither thermoelectric power nor ZT could be evaluated for thin film samples. This is probably because these films were coated on a silicon substrates which itself is conducting. Perhaps, thin film could be coated on quartz substrates and the ZT could be estimated. This is earmarked for future investigations. Though an attempt was made to nanostructure some of the compounds, due to lack of time, only a set composition were investigated for two different grain sizes. Scope prevails for carrying out a systematic study on compounds belonging to the series $Gd_{1-x}Sr_xMnO_3$ (x=0.3, 0.5, 0.6). A size dependent study for varying grain sizes, in each of the composition would be very interesting. In this context it must be mentioned that, one needs to calculate the mean free paths corresponding to electron, phonon and accordingly vary the grain sizes so that their conflicting requirements with respect to quantum confinements are taken care of.

Another obvious lacuna in this study is that a definitive statement as regard various mechanisms in different regimes could not be made for sure. More investigations are the only resort at this point of time. Various scattering mechanisms play a role in the conduction. For instance, there are electron scattering, phonon scattering and magnon scattering. The extent to which they are dealt in this thesis is superficial and hence an in-depth study is a necessity. This only will bring out the Physics and enable tailoring the properties. This is reserved for the successors. In perovskite manganites, the electrical transport is strongly spin dependent. Magnetic field dependent thermoelectric power measurements will bring out interesting observations in the field of spin-dependent charge ordered manganites. However, it could not be carried out in the samples and is left for future studies.

On a philosophical note, the re-emergence of manganites as a potential thermoelectric material can be equated with a re-entry. There are

re-entrances and re-emergences of many phenomenon. Most of them are cyclical. The most striking is the 11-year cycle which is responsible for sunspots which influence the earth very much. Many write them off as conjectures. Who knows!! Whether this conjecture of the re-emergence of manganites in the regime of thermoelectrics is going to be a money spinning one. But one thing is sure, in the near future, thermoelectric devices based on manganites can be expected and will be in the market, may be, with a little help from Nanotechnology! Even a multifunctional nanostructured manganite, all in one- a catalyst, GMR and a heat scavenger, could be in the market in coming days!